Advances in Radiofrequency Coil Developments for 7 Tesla Human MRI

by

Tales Roberto de Souza Santini

Bachelor of Science in Electrical Engineering, University of São Paulo, 2010

Master of Science in Electrical Engineering, University of São Paulo, 2014

Submitted to the Graduate Faculty of

Swanson School of Engineering in partial fulfillment

of the requirements for the degree of

Doctor of Philosophy

University of Pittsburgh

2019

UNIVERSITY OF PITTSBURGH

SWANSON SCHOOL OF ENGINEERING

This dissertation was presented

by

Tales Roberto de Souza Santini

It was defended on

July 26, 2019

and approved by

George D. Stetten, M.D., Ph.D., Professor
Department of Bioengineering

Howard J. Aizenstein, M.D., Ph.D., Professor
Departments of Psychiatry, Bioengineering, and Clinical and Translational Science

Joseph Mettenburg, M.D., Ph.D. Assistant Professor
Department of Radiology

Dissertation Director: Tamer S. Ibrahim, Ph.D., Professor
Departments of Bioengineering, Psychiatry, and Radiology

Advances in Radiofrequency Coil Developments for 7 Tesla Human MRI

Tales Roberto de Souza Santini, Ph.D.

University of Pittsburgh, 2019

Magnetic Resonance Imaging (MRI) is extensively used in clinics as a non-invasive medical diagnostic tool. MRI has excellent soft tissue contrast characteristics, utilizes non-ionizing radiation, and is considered safer than other imaging techniques, such as PET, CT, and X-Ray. Currently, clinics acquire MRI images using magnetic field intensities of 1.5 Tesla (T) and 3T. However, higher field strengths provide better resolution and improved tissue contrast. Two years following the FDA clearance of the first 7T scanner (Siemens, Terra), 7T related technologies are changing the standards of imaging and are expected to become the new clinical standard in the future. 7T MRI enables improved characterization of abnormalities in the human body and early identification of disease, especially in neuroimaging.

Despite the promises of 7T MRI, several challenges still need to be addressed before it can be widely utilized in the clinic. The higher the magnetic field strength implicates a shorter wavelength of the electromagnetic waves inside the tissues. At 7T, the RF wavelength is approximately 12 cm inside the tissues, which is smaller than many parts of the body. This short wavelength causes strong RF interference, which produces inhomogeneous RF field distributions inside the regions of interest. These inhomogeneities cause voids or regions of low contrast in the images, thus limiting the diagnostic capabilities of 7T MRI. Additionally, the inhomogeneous electric field distribution at 7T might lead to higher local and global power deposition, which is a safety concern.

In this dissertation work, optimized RF coil designs and methodologies are presented for head and extremity imaging at 7T. The simulated and experimentally-verified results show improved homogeneity of the RF magnetic field as well as reduction of power deposition in tissue during MRI scans.

Table of Contents

List of Tables

List of Figures

Preface

Firstly, I would like to thank my advisor Dr. Tamer S. Ibrahim for his guidance, energy, patience, and (huge) enthusiasm. It was a pleasure to work with him in the projects presented in this Dissertation. I also would like to thank the committee members for all the help throughout these years.

I would like to thank the members of the RF lab for all the good moments and the support in the difficulties. By seniority, thank you Narayanan, Kim, Yujuan, Sossena, Nadim, Neilesh, Tiago, Salem, and Danielle. I also would like to thank all the undergraduate students that worked with me and helped in several projects. By seniority, thank you Jacob, Anthony, Steve, Zach, Yutong, Lisa, Danesh, and Matt.

I would like to thank my mentors who so much helped at the beginning of this journey. Thank you Dr. Maciel, Dr. Marcelo Prado, Dr. Marcelo Vieira. I also would like to thank my dear friends Issao, Strutz, and my English teacher Margarida, I would not have started my Ph.D. without your support and help.

I would like to acknowledge the CAPES foundation for supporting my Ph.D. and the National Institutes of Health for supporting the projects developed in this Dissertation. I also would like to thank the University of Pittsburgh, the Department of Bioengineering, and the Pitt Strive (with special thanks to Sussan).

Finally, I would like to thank my parents, my sister, and my fiancée for the support throughout graduate school. I could not have done it without them.

1.0 Introduction

Magnetic Resonance Imaging (MRI) is a diagnostic tool largely used in medicine for acquiring images that aid in the detection and classification of diseases and various ailments in the human body. Its major advantages rely on its possibility to noninvasively image the body with excellent contrast for soft tissue structures and its metabolic process [1]. Most clinical applications use a static magnetic field (B_0) of 1.5 or 3 Tesla (T), however, 7T MRI was recently cleared by the regulatory agency FDA to be used clinically. The increase in B_0 provides higher signal-to-noise ratio (SNR), improved tissue contrast, and higher spatial resolution [2], potentially improving the detection, monitoring, and understanding of several diseases, such as Alzheimer's [3], Parkinson/Schizophrenia [4] and hemorrhage/strokes/microinfarcts [5]. However, moving towards 7T is not a mere scaling up of the system [6]. The wavelength (λ) of radiofrequency (RF) fields produced by these systems become smaller than some parts of the body ($\lambda \approx 12cm$, inside the tissue). The major consequences of the smaller wavelength are: 1) higher specific absorption ratio (SAR) [7, 8], specially peak SAR [9, 10] and average SAR [11, 12], presents risks for the subject due to potential tissue heating [13]; 2) reduced wavelength causes inhomogeneities in the radio frequency (RF) circular polarized magnetic field (B_1^+) [9, 10, 14, 15], causing voids in the images, especially when using high flip angle MRI clinical sequences [15, 16].

To accomplish high quality and safe imaging at 7T MRI, the RF coil [6] design and operation has to be entirely rethought. For this purpose, arrays of transmit and receive RF coils have been designed [17]. The RF field distribution created by each coil is inhomogeneous due to the UHF operational frequency, however, the sum of each component can deliver a relatively homogenous RF field pattern [18]. The Tic-Tac-Toe (TTT) is a multichannel, highly coupled and

load insensitive coil design [19]. The currently utilized TTT 7T head coil is a 16-channel transmit array that provides a whole head homogenous imaging at 7T [20]. This dissertation will present the details of the TTT design and operation with applications for head and foot imaging at 7T.

1.1 Motivation

The 7 Tesla (7T) MRI technology is reaching its maturity after almost 17 years as the first machine of this type was manufactured and with the recent FDA cleaning for the Terra Magneton 7T human MRI (Siemens, Germany). The advantages of its increased static magnetic field (B_0) are well known: 1) higher signal-to-noise ratio (SNR) can be used to acquire higher resolution clinical sequences in a shorter scanning time [9, 10, 21] – being capable of detecting smaller structures not seen at lower B0 [10, 22] (e.g. White Matter Hyperintensities (WMH) detection and its progression over time [5]); 2) higher contrast among soft tissues provides better detection of structural abnormalities [10]; 3) higher susceptibility effects improve susceptibility weighted imaging (SWI) and Blood-oxygen-level-dependent (BOLD) contrasts [9, 15] (essential in functional MRI (fMRI) applications).

The lack of an integrated transmit body coil for 7T scanners (currently available at lower fields (i.e. 1.5T and 3T)) forces the development of local transmit RF coils for proton excitation. For this purpose, traditional approaches of RF coil development have been applied (e.g. birdcage [16]) as well as multichannel approaches, such as TEM [23], microstrip [24], and loop coils [18, 24], but the inhomogeneous B_1^+ pattern provided by these coils degrades the image quality and its diagnosis capabilities. Our group developed the Tic-Tac-Toe (TTT) design for 7T imaging [20, 25-33]. After approximately 5 years of the implementation of the 16 channels head TTT coil, more

than 750 subjects were scanned in patient studies. The results consistently show an unprecedented homogeneity provided by this innovative RF coil [20]. Moreover, the simulations and preliminary experimental data also indicated that the TTT design presents a considerable reduced SAR when compared with the traditional TEM RF coil (scaled for the same average B_1^+) [34], demonstrating the safety of the design. The TTT design has also been applied successfully to the body [33], foot/ankle [35, 36], and breast imaging [25, 26].

1.1.1 Challenges in 7T MRI Systems: Ankle/Foot

Most clinical scanners have a field intensity of 1.5T or 3T. These scanners also present a body coil for spin excitation integrated to the system. This body coil can provide homogenous excitation to any part of the body, including the ankle/foot. For 7T scanners, the lack of an integrated commercial body coil and the absence of a commercial dedicated foot/ankle coil prevent the research sites from properly acquiring images from these parts of the body. Most research centers utilize a head or knee coil for imaging the ankle/foot, which is far from optimal: 1) for the case of the head coil, it may not be suitable for all foot sizes, since head coils are designed with tight fit for the head, presenting limited space and potentially high SAR; 2) for the case of using a knee coil, the foot has to stay in a high angle position due to the cylindrical shape of the coil (the recommended angle of flexion is less than 10 degrees [37]), making this option impractical for clinical applications, when an injured foot/ankle may not be able to extend.

1.1.2 Challenges in 7T MRI Systems: Neuro

Head and neuro imaging at 7T MRI suffer from RF inhomogeneity because the head size is up to twice the size of an RF wavelength in the anterior-posterior direction. In commercial solutions, the inhomogeneities are severe in the lower regions of the brain, such as the cerebellum and temporal lobes. This affects mostly high flip angle clinical sequences, such as turbo-spin echo (TSE), fluid-attenuated inversion recovery (FLAIR), and angiography with the time-of-flight sequences. Using these clinical MRI sequences at 7T, the images acquired in the cerebellum and temporal lobes often present voids, or regions of low contrast, when scanning with commercially available head coils. Moreover, with the decreased skin depth and the increased RF inhomogeneities, there is a higher local/global RF power deposition in the brain tissues. Therefore, it is necessary to have reliable simulations and innovative coil design to overcome these issues.

1.2 Objectives of this Dissertation

The work presented in this dissertation contributes to the long-term goal of developing robust and reliable RF coils based on the TTT design for 7T applications. These RF coils should generate homogeneous and subject insensitive B_1^+ field distribution while keeping the robustness currently seen in clinical MRIs (1.5T and 3T). The main goal of this work is to further develop software and hardware tools to design, improve, and characterize the performances of the RF coils, capable to be used as both single transmit channel (the hardware cleared by the FDA for clinical platform at 7T) or multichannel transmit mode (pTx).

Objective 1: Develop an RF coil for ankle and foot imaging at 7T MRI. The coil is composed of 4-channel TTT transmit and 4-channel receive RF coil. The TTT design is utilized to provide a homogeneous magnetic field distribution inside the region of interest, with sufficient efficiency and adequate levels of SAR. The coil was tested with several clinical and research musculoskeletal sequences including T2DESS, PD TSE, SWI, and B_1^+ Mapping.

Objective 2: Develop a generic model for optimizing RF coil design/shimming and comparison between the TTT and the traditional TEM RF coil. An in-house developed and validated Finite-Difference Time-Domain (FDTD) software was used to simulate the RF coil designs and each result was quantitatively evaluated by applying Matlab-based optimizations tools for RF shimming. A new methodology was developed for RF shimming that is intended for achieving a blend of quantitative characteristics that constrain the RF fields produced by RF coils. This technique was applied in the current 16-channel TTT head coil. Patient studies were performed using the current RF coil in conjunction with RF shimming technique achieved using the proposed methodology.

Objective 3: Develop a 64-channel TTT transmit head RF coil. Several models of this RF coil were simulated and evaluated using the methodology developed in Objective 2 and the design that provides the best homogeneity, sufficient efficiency, and low levels of SAR was constructed using 3D printing. The performance (B_1^+ field, SAR, scattering parameters, efficiency) were evaluated as a part of this objective.

1.3 Outline of this Dissertation

This Dissertation is structured as follows, including the publications pertaining to each chapter.

Chapter 2: a review of the principals of MRI is presented, including the physical phenomena that originated the technology, the components of the MRI scanner, a brief review of transmit and receive RF coils, and the finite-difference time-domain method, that was used for electromagnetic simulations presented in this dissertation

Chapter 3: the development of an RF coil for foot and ankle is presented. The RF system is composed of 1 Tic-Tac-Toe side, totaling 4 channels, for the transmission, and a 4-channel loop array for signal reception. Numerical simulations are compared with experimentally acquired data in the cylindrical phantom. The RF coil was then used for in-vivo image acquisitions in a volunteer.

Chapter 4: this chapter presents the theoretical analysis of a 20-channel transmit RF array based on the Tic-Tac-Toe design. The eigenmodes of the RF array is calculated using FDTD simulations. The results are compared with experimentally acquired data. It also presents the specific absorption rate (SAR) from each eigenmode. Finally, it presents one example of the combination of the eigenmodes, demonstrating its potential to create a homogenous magnetic field distribution inside the head at 7T MRI.

Chapter 5: in this chapter, the Tic-Tac-Toe RF coil design is optimized for patient studies. Considerations of subject insensitiveness, specific absorption rate, and magnetic field homogeneity are presented in addition to several numerical optimizations. Two cases were

implemented and experimentally verified. The most homogenous case has been used in several patient studies, totaling more than 750 subjects scanned thus far using the presented methodology.

Chapter 6: this chapter presents the new generation of the Tic-Tac-Toe design for head imaging at 7T MRI. The original 9-inch panels were reduced to 4.25 inches, totaling 16 panels around the head and 64 channels in total. FDTD simulations and numerical optimizations were performed. Preliminary data was acquired in a spherical phantom. The following publications are related to this work.

Chapter7: final considerations are presented in this chapter, as well as the future work that can be developed from this Dissertation.

Appendix A: this appendix presents a comparison between the Tic-Tac-Toe head coil design and the traditional Transverse Electromagnetic (TEM) Resonator coil. Several head models were simulated using the FDTD method. The two coil designs were compared using several metrics, such as efficiency, power deposition in the tissues, and subject insensitivity. The following publications are related to this work.

Appendix B: this appendix demonstrates the quality of the MRI images acquired in-vivo at 7T with the 16-channel TTT design, presented in detail in Chapters 4, 5 and 6.

1.4 Publications

1.4.1 Refereed Journal Articles

1. **Tales Santini***, Narayanan Krishnamurthy*, Junghwan Kim, Sossena Wood, Howard Aizenstein, and Tamer S. Ibrahim. *"Computational and Experimental Evaluations of transmission line Based RF Coils at 7T"*. PlosOne, 2019. *equal contribution.
2. Melania Borges, Marcelo Prado, **Tales Santini**, Adriano Barbosa, Antonio Moreira, Issao Ishibe, Marcelo Katz, Fatima Cintra. "Development and clinical validation of a non-invasive, beat-to-beat blood pressure monitoring device, compared to invasive blood pressure monitoring during coronary angiography." Einstein Journal (2019).
3. **Tales Santini**, Yujuan Zhao, Sossena Wood, Narayanan Krishnamurthy, Junghwan Kim, Nadim Farhat, Tiago Martins, Tiejun Zhao, Howard Aizenstein, and Tamer S. Ibrahim. *"In-vivo and numerical analysis of the eigenmodes produced by a multi-level head transmit array for 7 Tesla MRI*" PlosOne, 2018.
4. **Tales Santini**, Junghwan Kim, Sossena Wood, Narayanan Krishnamurthy, Nadim Farhat, Carlos Maciel, Shailesh Raval, Tamer Ibrahim. *"A new RF Transmit Coil for Foot and Ankle Imaging at 7T MRI."* Magnetic Resonance Imaging, 2018.
5. Stephen Smagula, Helmet Karim, Anusha Rangarajan, Fernando Santos, Sossena Wood, **Tales Santini**, John Jakicic, Charles ReynoldsIII, Judy Cameron, Abbe Vallejo, Meryl Butters, Caterina Rosano, Tamer Ibrahim, Kirk Erickson, Howard Aizenstein. *"Association of hippocampal substructure resting-state functional connectivity with memory performance in older adults,"* American Journal of Geriatric Psychiatry, 2018.
6. Kim, Junghwan, **Tales Santini**, Kyongtae Ty Bae, Narayan Krishnamurthy, Yujuan Zhao, Tiejun Zhao, and Tamer S. Ibrahim. *"Development of a 7 T RF coil system for breast imaging."* NMR in Biomedicine 2017.
7. Sossena Wood, Narayanan Krishnamurthy, **Tales Santini**, Shailesh Raval, Nadim Farhat, John Andy Holmes, Tamer S. Ibrahim. *"Design and fabrication of a realistic anthropomorphic heterogeneous head phantom for MR purposes"*. PLoS ONE 2017.

8. Shailesh Raval, Cynthia A. Britton, Tiejun Zhao, Narayanan Krishnamurthy, **Tales Santini**, Vijay Gorantla, Tamer Ibrahim. *"Ultra-high field upper extremity peripheral nerve and non-contrast enhanced vascular imaging."* PloS ONE, 2017.
9. **Tales Santini**, Tamer Ibrahim, Carlos Maciel. "*Load-insensitive active quasi-circulator for continuous-wave Doppler ultrasound applications*." Electronics Letters, 2016.
10. Junghwan Kim, Narayan Krishnamurthy, **Tales Santini**, Yujuan Zhao, Tiejun Zhao, Kyongtae Ty Bae, and Tamer S. Ibrahim. *"Experimental and numerical analysis of B1+ field and SAR with a new transmit array design for 7T breast MRI."* Journal of Magnetic Resonance, 2016.
11. Shailesh B. Raval, Tiejun Zhao, Narayanan Krishnamurthy, **Tales Santini**, Cynthia Britton, Vijay S. Gorantla, Tamer S. Ibrahim. *"Ultra-high-field RF coil development for evaluating upper extremity imaging applications."* NMR Biomed, 2016
12. Miguel Filho, Alexandre R. Marra, Thyago Magnus, Rodrigo Rodrigues, Marcelo Prado, **Tales Santini**, Elivane Victor, Eder Ishibe, Oscar Santos, Michael Edmond. *"Comparison of human and electronic observation for the measurement of compliance with hand hygiene."* American Journal of Infection Control, 2014.

1.4.2 Book Chapter

1. Nadim S. Farhat, Robert Theiss, **Tales Santini**, Tamer S. Ibrahim, Howard J. Aizenstein. "Recent advances in Neuroimaging of Small Vessel Disease in Late-life Depression". Advances in Experimental Medicine and Biology (AEMB), book series of Springer.

1.4.3 Conference Proceedings

1. Stephen Smagula, **Tales Santini**, Sarah Stahl, Tamer Ibrahim, Charles Reynolds, Richard Schulz, Layla Banihashemi, Liang Zhan. "White Matter Integrity Underlying

Subsyndromal Depression Symptoms in Dementia Caregivers". Gerontological Society of America annual meeting, Austin, TX, 2019

2. Matthew Saich, **Tales Santini**, Neilesh Vinjamuri, Tiago Martins, Zachary Fritts, Minseok Koo, Salem Alkhateeb, Nadim Farhat, Tamer S. Ibrahim. "Construction and Testing of the 4-channel Microstrip Tic-Tac-Toe RF coil Design for 7T MRI". BMES 2019
3. **Tales Santini**, Sossena Wood, Howard J. Aizenstein, Tamer S. Ibrahim. "Homogenous 64-channel RF transmit array for brain imaging at 7T, 9.4T, and 10.5T." ISMRM 2019
4. **Tales Santini**, Sossena Wood, Narayanan Krishnamurthy, Tiago Martins, Nadim Farhat, Salem Alkhateeb, Howard J. Aizenstein, Tamer S. Ibrahim. "Optimization of RF system for homogenous, consistent, and safe neuro imaging at 7T MRI" ISMRM 2019
5. Danesh Thirukumaran, **Tales Santini**, Sossena Wood, Nadim Farhat, Salem Alkhateeb, Tiago Martins, Howard Aizenstein, Enrico Novelli, Tamer S. Ibrahim. "Utilization of DTI analysis for Sickle Cell Disease related Cerebral Infarction". BMES 2019
6. Nadim Farhat, Helmet Karim, **Tales Santini**, Neilesh Vinjamuri, Howard Aizenstein, Enrico M Novelli, Tamer Ibrahim. "Default mode networks connectivity characterization in young adults with sickle cell disease using 7T resting functional magnetic resonance imaging." ISMRM 2019
7. **Tales Santini**, Fabrício Brito, Sossena Wood, Tiago Martins, Joseph Mettenburg, Howard Aizenstein, Marcelo Vieira, Tamer S. Ibrahim. *"Noise mitigation from high-resolution 7T MRI images"* In Proc. of the 26th International Society of Magnetic Resonance in Medicine Annual Meeting, Paris, France, 2018.
8. **Tales Santini**, Sossena Wood, Narayanan Krishnamurthy, Yutong Zhang, Howard Aizenstein, Tamer S. Ibrahim. *"New optimization strategies for RF shimming at UHF MRI*" In Proc. of the 26th International Society of Magnetic Resonance in Medicine Annual Meeting, Paris, France, 2018.
9. **Tales Santini**, Yujuan Zhao, Sossena Wood, Junghwan Kim, Nadim Farhat, Narayanan Krishnamurthy, Tiejun Zhao, Tamer S. Ibrahim. *"Experimental and Numerical Evaluations of Simultaneously Excited Eigenmodes in a 20-channel Transmit RF Array for 7 Tesla human MRI".* In Proc. of the 26th International Society of Magnetic Resonance in Medicine Annual Meeting, Paris, France, 2018.

10. Sossena Wood, **Tales Santini**, Nadim Farhat, Tiago Martins, Narayanan Krishnamurthy, Tamer Ibrahim. *"B1+ and Temperature Analysis in Two UHF RF Coils"*, In Proc. of the 26th International Society of Magnetic Resonance in Medicine Annual Meeting, Paris, France; 2018.
11. Sossena Wood, **Tales Santini**, Narayanan Krishnamurthy, Tiago Martins, Tamer Ibrahim. *"Comparison of Electric and B1+ Fields for Heterogeneous and Homogeneous Anthropomorphic Phantoms and Anatomical Models: Numerical Simulations and Experimental Findings"*, In Proc. of the 26th International Society of Magnetic Resonance in Medicine Annual Meeting, Paris, France; 2018.
12. Minseok Koo, **Tales Santini**, Neilesh Vinjamuri, Sossena Wood, Nadim Farhat, Tiago Martins, Salem Alkhateeb, Tamer S. Ibrahim. *"Building and Testing of the 64-channel Radio Frequency (RF) Head Coil for Ultra-High Field MRI Applications"* BMES 2018
13. Nadim Farhat, Julia Kofler, **Tales Santini**, Sossena Wood, Tiago Martins, Salem Alkhateeb, Shane McKeon, Howard Aizenstein, and Tamer S. Ibrahim. Utility of 7T postmortem MRI in investigating Alzheimer's Disease. Aging Institute research day, University of Pittsburgh, Pittsburgh, USA, 2018.
14. Sossena Wood, Tiago Martins, **Tales Santini**, Tamer Ibrahim, *"An electrically conductive SLA resin used for the Design of Anthropomorphic Phantoms"*, In Proc. of the 26th International Society of Magnetic Resonance in Medicine Annual Meeting, Paris, France; 2018.
15. Shane D. McKeon, Anusha Rangarajan, Minjie Wu, Nadim Farhat, **Tales Santini**, Sossena Wood, Tamer Ibrahim, Milos Ikonomovic, Julia Kofler, Oscar Lopez, Bill Klunk, Howard Aizenstein. "Co-registration of MRI-defined White Matter Lesions with Ex-Vivo Histopathology" BMES 2018.
16. **Tales Santini,** Junghwan Kim, Sossena Wood, Naraynan Krishnamurthy, Shailesh Raval, Tamer Ibrahim. *"A new RF coil for foot and ankle imaging at 7T MRI."* In Proc. of the 25th International Society of Magnetic Resonance in Medicine Annual Meeting, Honolulu, Hawaii, April 2017.
17. **Tales Santini,** Narayanan Krishnamurthy, Sossena Wood, Shailesh Raval, Yujuan Zhao, Anthony Fischetti, Minseok Koo, Howard Aizenstein, Tamer Ibrahim. *"64-channel Double-Octagon Tx Head Coil for 7T Imaging."* In Proc. of the 25th International

Society of Magnetic Resonance in Medicine Annual Meeting, Honolulu, Hawaii, April 2017.

18. Tamer Ibrahim, **Tales Santini**, Shailesh Raval, Narayanan Krishnamurthy, Sossena Wood, Junghwan Kim, Yujuan Zhao, Xiaoping Wu, Essa Yacoub, Howard Aizenstein, Tiejun Zhao. *"Towards Homogenous 7T Neuro Imaging: Findings and Comparisons between 7T TTT and NOVA RF Coil Systems."* In Proc. of the 25th International Society of Magnetic Resonance in Medicine Annual Meeting, Honolulu, Hawaii, April 2017.
19. Shailesh Raval, **Tales Santini**, Sossena Wood, Narayanan Krishnamurthy, Tamer Ibrahim, *"In-vivo (8x4) 32-ch Tx-only Body Array for UHF MR."* In Proc. of the 25th International Society of Magnetic Resonance in Medicine Annual Meeting, Honolulu, Hawaii, April 2017.
20. Neilesh Vinjamuri, **Tales Santini**, Sossena Wood, Tamer S. Ibrahim. "*Optimizing geometry of a 64-channel RF head coil*". BMES 2017
21. Sossena Wood, Narayanan Krishnamurthy, **Tales Santini**, Shailesh Raval, Tamer Ibrahim. *"Evaluation of an Anthropomorphic Phantom with In-Vivo Using Quantitative MRI."* In Proc. of the 25th International Society of Magnetic Resonance in Medicine Annual Meeting, Honolulu, Hawaii, April 2017.
22. Shane D. McKeon, Anusha Rangarajan, Minjie Wu, **Tales Santini**, Tamer S Ibrahim, Oscar Lopez, Howard Aizenstein. *"Evaluation of Segmentation Performance with 3T and 7T Magnetic Resonance Imaging using FreeSurfer"*. BMES 2017
23. Shane D. McKeon, Naomi Joseph, Anusha Rangarajan, Minjie Wu, Nadim Farhat, **Tales Santini**, Sossena Wood, Tamer Ibrahim, Milos Ikonomovic, Julia Kofler, Oscar Lopez, Bill Klunk, Howard Aizenstein. *"Co-Registration of In-Vivo and Ex-Vivo Human MRI Brain Images"*. BMES 2017
24. Fernando P. Santos, Stephen F. Smagula, Helmet Karim, **Tales Santini**, Howard J. Aizenstein, Tamer S. Ibrahim, and Carlos D. Maciel. *"Dynamic Bayesian Network Modeling of Hippocampal Subfields Connectivity with 7T fMRI."* Biosignals, 2016.
25. Narayanan Krishnamurthy, Yujuan Zhao, **Tales Santini**, Sossena Wood, Tiejun Zhao, and Tamer Ibrahim. *"Case Studies of 7T RF Shimming using Parallel Tx & Rx System."* International Society for Magnetic Resonance in Medicine, 2015.

26. Narayanan Krishnamurthy, Yujuan Zhao, Shailesh Raval, Junghwan Kim,Sossena Wood, **Tales Santini**, Tiejun Zhao, and Tamer S. Ibrahim. *"7T Multi-slab Whole-Head Homogenous and Low SAR T2 Acquisitions with Limited RF Power Amplifiers Capabilities."* International Society for Magnetic Resonance in Medicine, 2015.
27. Shailesh Raval, Tiejun Zhao, Narayanan Krishnamurthy, **Tales Santini**, Vijay S. Gorantla, and Tamer S. Ibrahim. *"Upper extremity neural and vascular imaging with UHF 7T MRI."* International Society for Magnetic Resonance in Medicine, 2015.
28. **Tales Santini,** Carlos Maciel. *"Project of an Active Circulator for Doppler Ultrasound Systems Application."* Brazilian Congress of Automation, 2012.

2.0 Background

2.1 Magnetic Resonance Imaging

2.1.1 The Magnetic Moment of the Atom and Static Magnetic Field

All matter in the universe is composed of atoms. A simplified model of the atom (Figure 1) includes a nucleus composed of protons (positively charged sub-particle), neutrons (without electrical charge and presented in all atoms but the hydrogen), and electrons (negatively charged).

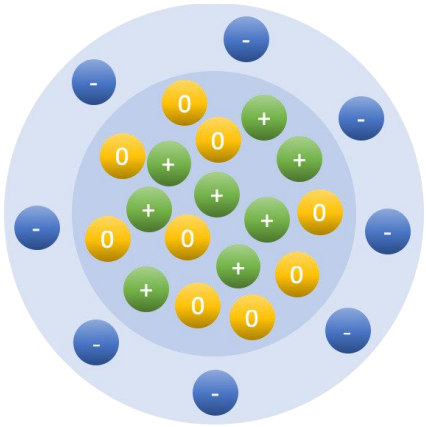

Figure 1: atomic model for the oxygen atom, with 8 protons (positively charged, represented by the green spheres), 9 neutrons (no electrical charge, represented by the yellow spheres), and 8 electrons (negatively charged, represented by the blue spheres)

The atomic mass (in Da, equivalent to $1.66 \times 10^{-27}\ kg$) is approximately equal to the number of protons plus the number of neutrons, since the electrons have a relatively small mass.

The charges inside the nucleus of atoms with an odd mass number become unbalanced and susceptible to the influence of an external magnetic field, behaving as small magnets. This behavior is called the magnetic moment of the atom, which has vector properties.

Without an external static magnetic field, the magnetic moment of the atom is randomly oriented (Figure 2a). In this situation, the vector sum of the magnetic moments, called Net Magnetization Vector (NMV) is null and, therefore, cannot be detected in macro-scale. When a strong static magnetic field (B_0) is applied, the magnetically active atoms align in either the direction of the applied magnetic field or in the opposite direction (Figure 2b), being that the number of atoms aligned in the B_0 direction (called low energy atoms) are slightly larger than in the opposite direction (high energy). This difference creates the NMV in the same direction of the B_0, and its intensity is proportional to the B_0 field intensity (Figure 2c). Hydrogen atoms at 7T intensities, for instance, have a difference of about 7.6 ppm between low and high energy spins.

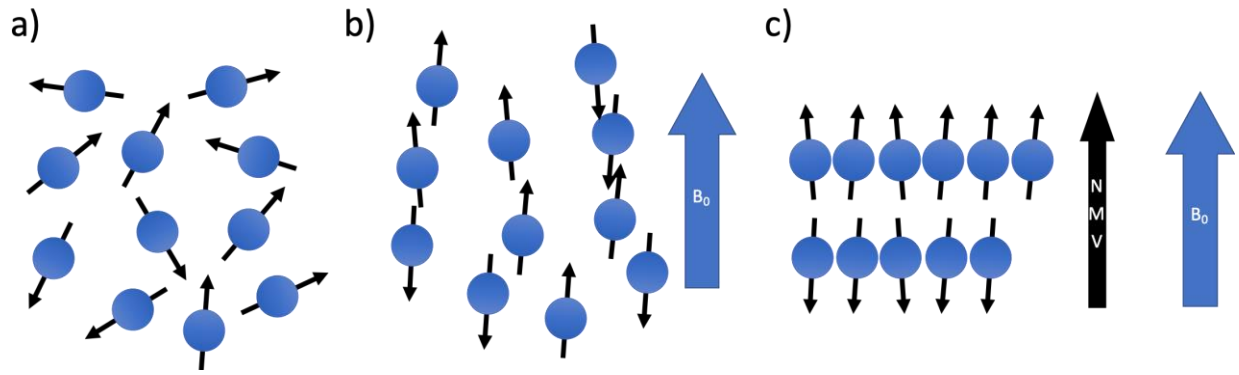

Figure 2: MR active nuclei. In a), without an external static magnetic field, the nuclei magnetic moment is randomly oriented. In b), the application of a strong magnetic field (B0) align the nuclei in either parallel or antiparallel directions in relation to the static magnetic field. In c), the number of nuclei aligned in parallel (low energy nuclei) is slightly larger than the nuclei aligned in antiparallel orientation (high energy nuclei), generating a Net Magnetization Vector (NMV)

2.1.2 RF Excitation and Recovery

If a circularly polarized magnetic field (B_1^+) with a specific frequency is applied over the NMV, it will change its direction, and precess until it loses the energy to the environment and returns to the B_0 orientation (Figure 3a). This resonance frequency of the nuclei is known as Larmor frequency and it is proportional to the B_0 intensity and the gyromagnetic constant of the medium (Table 1). The resonance frequency of the nuclei can be calculated by Equation 2-1 using the values from Table 1, valid for a homogenous medium.

Table 1: MR Properties of the MR Active Atoms Most Abundant in the Human Body [1]

Nucleus	Magnetic Moment [μ_N]	Gyromagnetic ratio λ [MHz/T]	Abundance in the human body [M]
Hydrogen (^{1}H)	2.79	42.58	88
Sodium (^{23}Na)	2.22	11.27	80×10^{-3}
Phosphorus (^{31}P)	1.13	17.25	75×10^{-3}
Oxygen (^{17}O)	-1.89	-5.77	16×10^{-3}
Fluorine (^{19}F)	2.63	40.08	4×10^{-6}

$$f_L = \gamma \cdot B_0 \qquad 2\text{-}1$$

where f_L is the Larmor frequency [Hz], γ is the gyromagnetic ratio [MHz/T], and B_0 is the static magnetic field [T].

The most abundant MR active atom in the human body is the hydrogen atom, due to their presence in water and fat. The hydrogen nuclei are also highly MR active, due to the presence of only one proton in its nucleus. This provides a high signal to noise ratio in soft tissues such as brain, muscles, and cartilage. For these reasons, the hydrogen atoms are the most used for clinical and research MR.

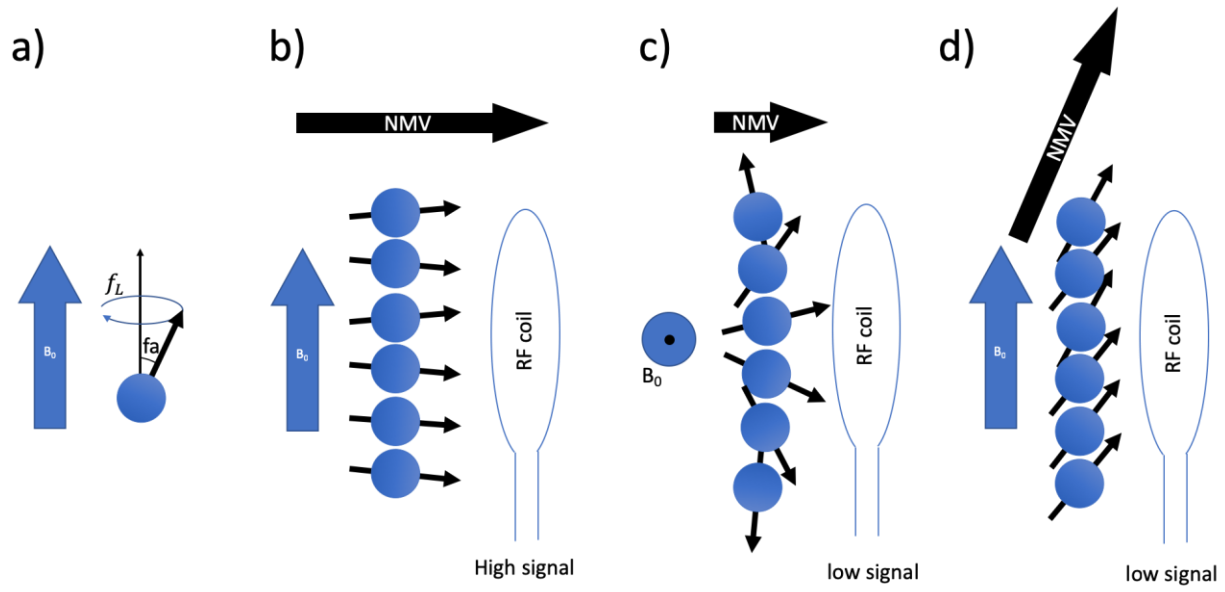

Figure 3: Magnetization and Relaxation. In a), after the application of a circularly polarized RF pulse at Larmor frequency, the magnetic moment of the proton starts to precess around the B0 orientation with a frequency equal to the Larmor frequency (f_L), and an angle from the B0, denoted by fa (flip angle). In b), the magnetic moment of the protons have a flip angle of 90 degrees and are in phase; this produces a maximum signal in the receive RF coil parallel to B0. In c), the flip angle is 90 degrees, but the magnetic moments are out of phase, leading to low signal in the receive RF coil. In d), the magnetic moment of the nuclei are in phase, but the flip angle is lower than 90 degrees, leading to low signal in the receive coil.

The flip angle of the NVM with the application of a circularly polarized magnetic field is defined by Equation 2-2:

$$f_a = \gamma \cdot B_1^+ \cdot t_p \cdot 360 \qquad 2\text{-}2$$

where f_a is the flip angle in degrees, γ is the gyromagnetic constant of the nuclei [MHz/T], B_1^+ is the circularly polarized magnetic field at Larmor frequency [μT], and t_p is the time of the pulse [s].

After the application of the RF pulse (Figure 3b), the NVM relaxation occurs in two ways: 1) the transverse relaxation, that is the dephasing of the magnetic moments of the nuclei (Figure 3c), which occurs according to the T2 constant of the tissues (Figure 4a); 2) the longitudinal relaxation, when the NVM moves towards B_0 direction, losing energy to the environment (Figure 3d), which is measured by the T1 constant of the tissue (Figure 4b).

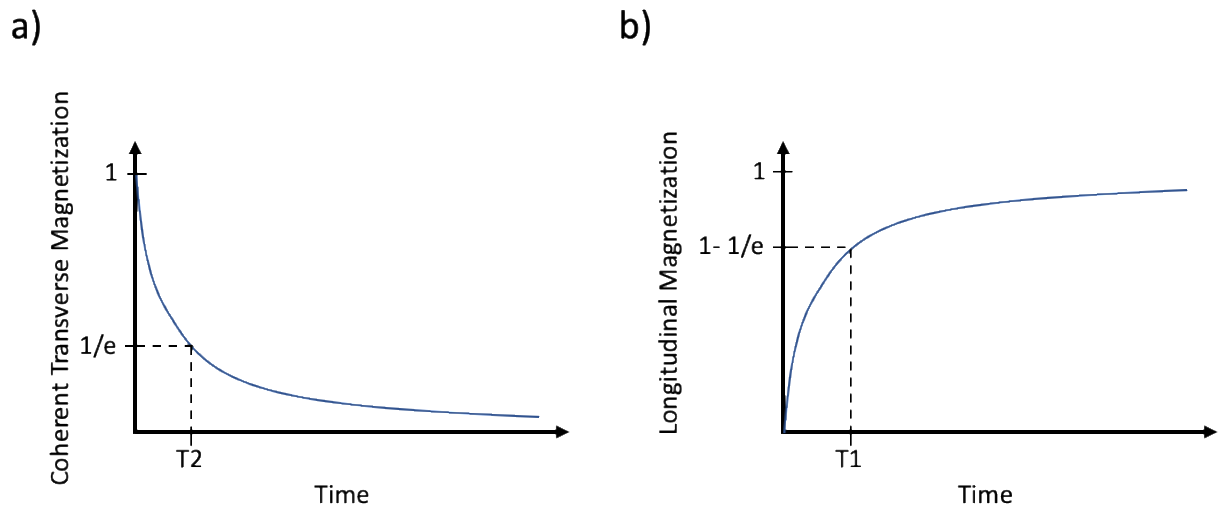

Figure 4: Relaxation of the NVM. In a), the transverse relaxation, generating the T2 time constant of the tissue. In b), the longitudinal relaxation, generating the T1 time constant of the tissue.

2.1.3 Gradient Coils, Spatial Encoding, and k-Space

In MRI scanners, the gradient coils are responsible for the spatial encoding of the acquired data. They are composed of conductive wires or metallic strips and are used to slightly modify the main magnetic field when a current is applied, causing a variation of the resonance frequency (Equation 2-1) of the material being scanned. This frequency variation can variate according to the spatial location of the material and, therefore, is used for spatial encoding. There are usually 3 gradient coils that are integrated into the scanner system, each one providing a gradient in the magnetic field in the X, Y, or Z directions, in Cartesian coordinates. Figure 5 shows an example of a fingerprint gradient coil; similar models are used in modern scanner systems. The gradient coils operate in the range of audible frequencies and are responsible for the loud noises heard during an MRI scan.

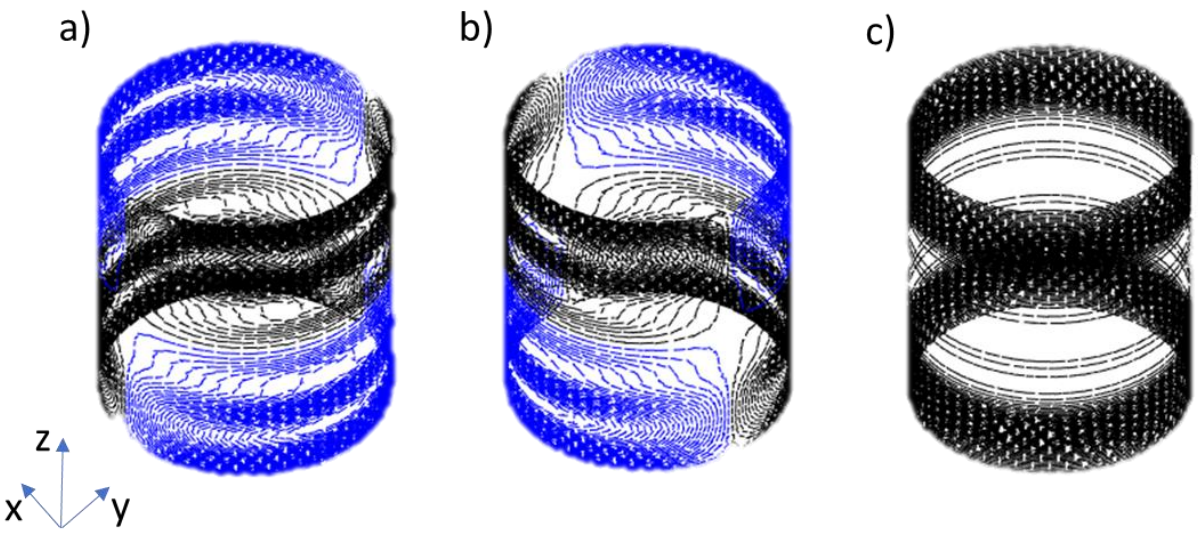

Figure 5: Example of gradient coil design. In a), the X gradient coil; in b), the Y gradient coil; in c), the Z gradient coil.

The Gradient coils create a slope in the Magnetic field intensity over the distance, as seen in Figure 6a. This changes the resonance frequency of the matter, making it possible to estimate the distance from the center by the frequency variation (Figure 6a). This is used to map the pixels and is defined as frequency encoding.

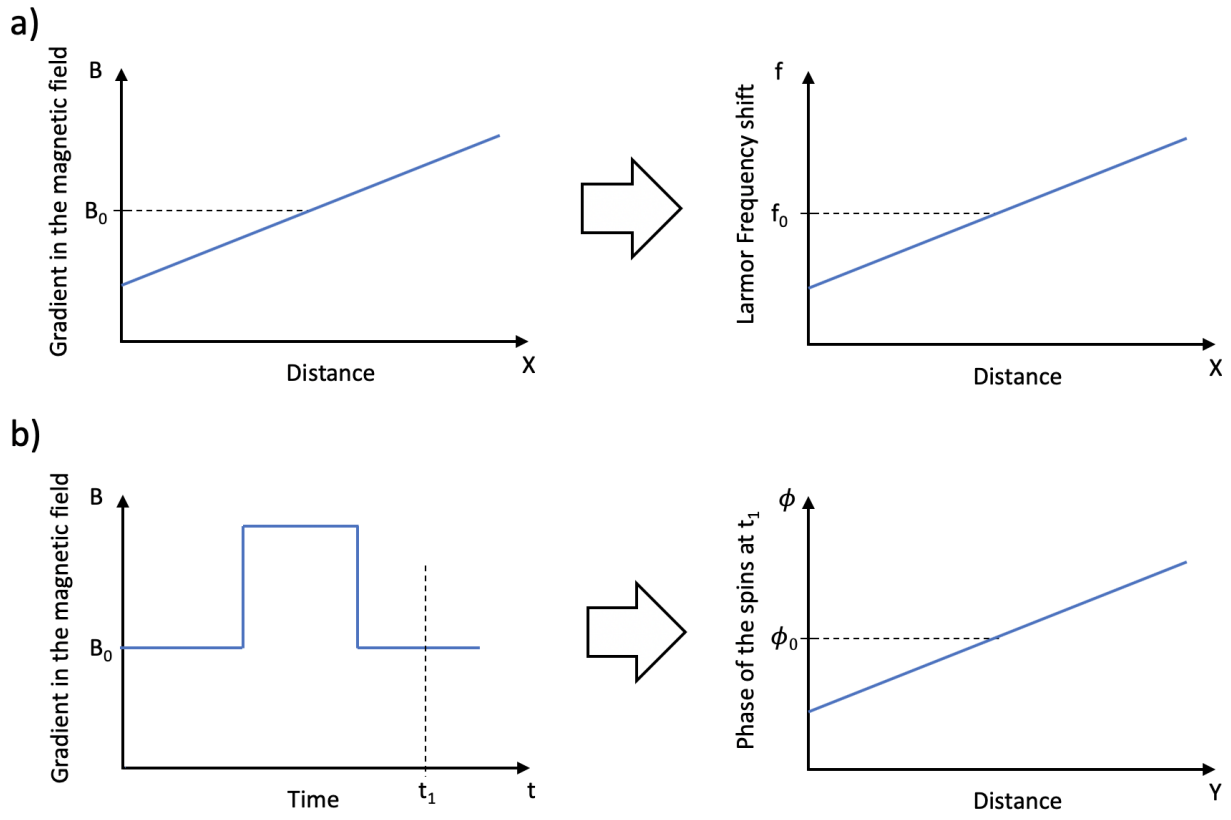

Figure 6: Effects of the Gradient coils. In a), an example of the linear gradient varying in X direction (figure on the left) and the frequency variation due to the gradient in the X direction (on the right); in b), a pulse in the gradient in the Y direction (on the left) and the variation of the phase due to the application of the pulse (on the right).

Similarly, when a square shaped pulse is applied to a gradient coil (Figure 6b), the Larmor frequencies on the matter are maintained before and after the application of the pulse. However, there is a phase shift that is dependent on the distance in an almost linear way (Figure 6b). This phenomenon can be used to map the pixels and it is defined as phase encoding.

Combining the phase and the frequency encoding, it is possible to map a specific pixel in the 2D cartesian plane. The selection of a specific slice is accomplished by applying another

gradient during the spin excitation, flipping the spins that are in the pulse bandwidth, therefore selecting a specific thin slice for the spin excitation. The phase and frequency encoding gradients are usually active during the signal reception portion of the MRI sequence.

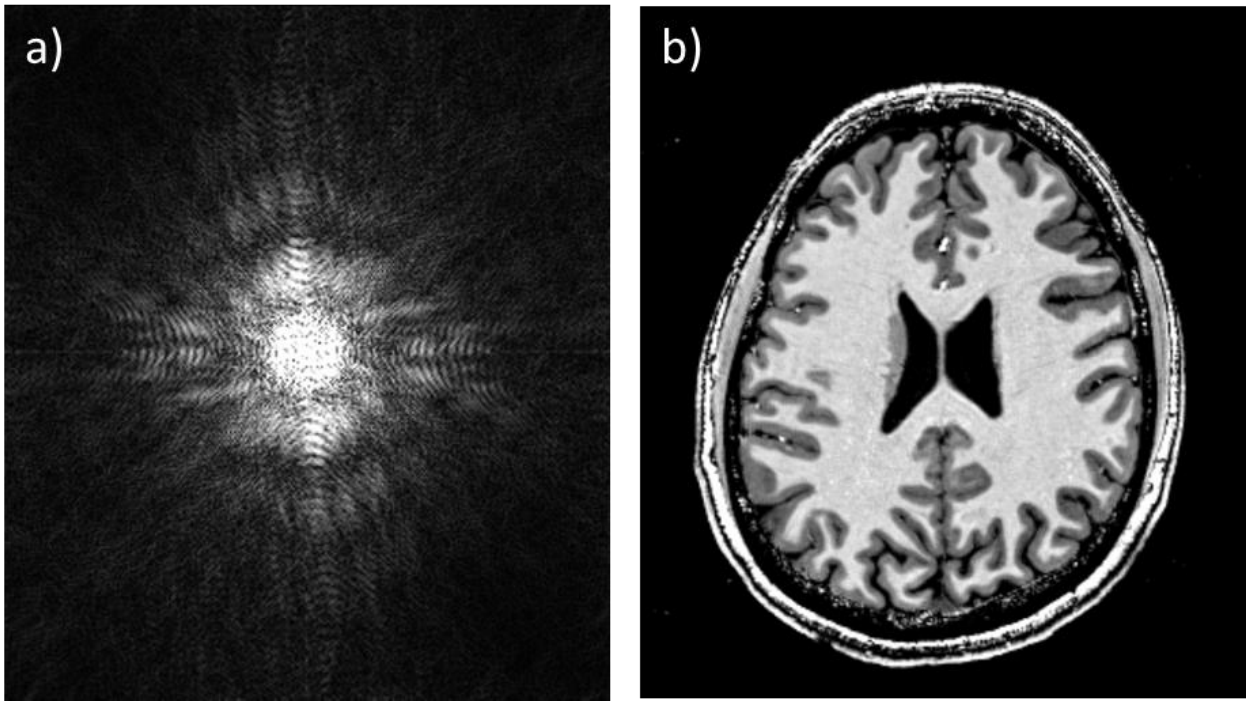

Figure 7: Example of MRI image in two domains, aquired using the Tic-Tac-Toe head RF system. In a), the k-space of the slice; in b), the image reconstructed using Fourier Transform.

The MRI data is acquired in the frequency domain, generating the k-space, as shown in Figure 7a. The image is then reconstructed using Fourier transform (Figure 7b). Several acceleration techniques (e.g. GRAPPA, partial Fourier, Fingerprinting, among other techniques) do not acquire the whole k-space, therefore making it necessary to apply algorithms to estimate the missing points in the k-space.

2.1.4 Gradient Echo and Spin Echo Phenomena

The MRI sequences are usually based on either the free induction decay (Figure 4), gradient echo, or spin echo phenomena. Figure 8a demonstrates the spin echo phenomena, in which a 90-degree flip angle pulse is followed by an inversion pulse (180-degree flip angle), the subsequent echo follows the T2 decay curve, recovering the dephasing caused by the T2* decay. Figure 8b shows the gradient echo phenomena, where an RF pulse is applied and the gradient is activated afterward, dephasing the spins. When the gradient is inverted, the gradient echo occurs, recovering the T2* decay.

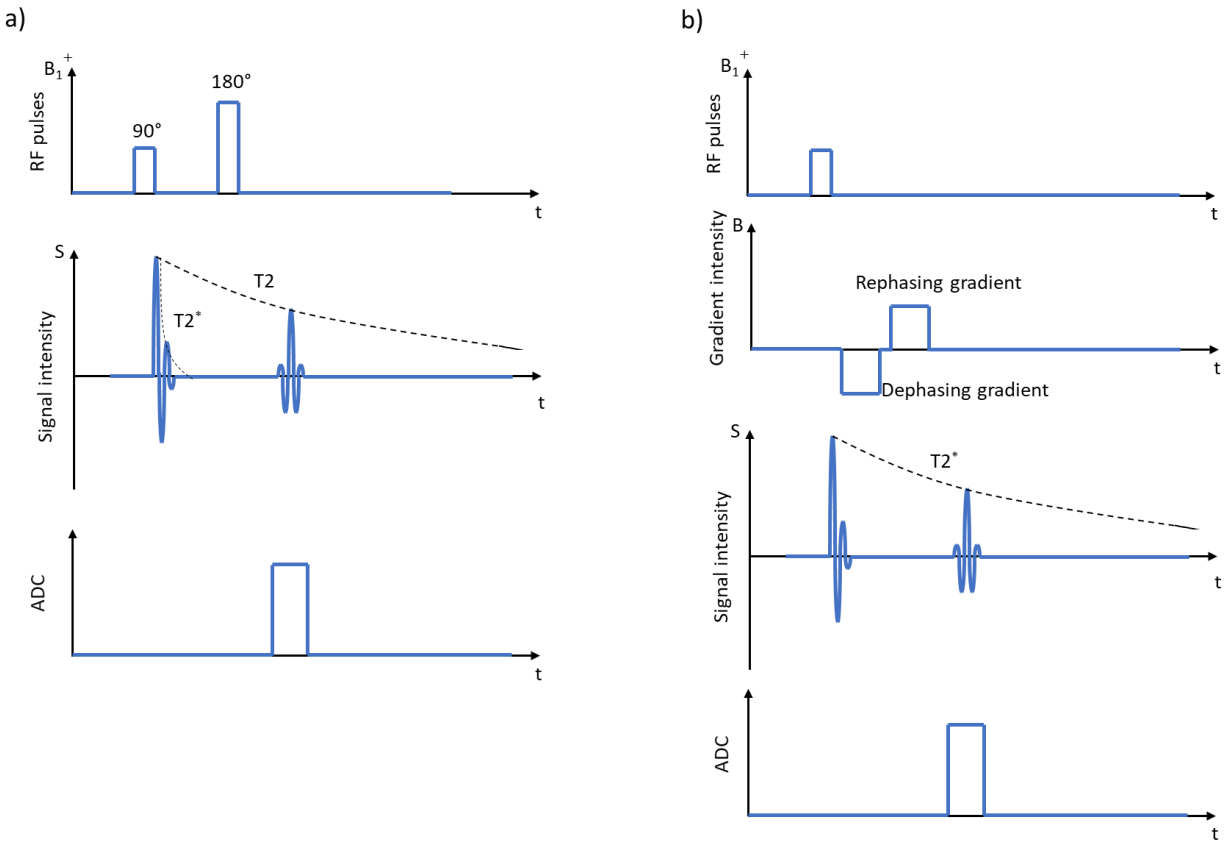

Figure 8: Simplified pulse scheme for the two basic MR phenomena. In a), Spin Echo, which two RF pulses are utilized (90-degree and 180-degree flip angle), the data is acquired during the echo by the analog-to-digital converters (ADC); in b), similarly, the Gradient Echo is presented. In this configuration, a low flip-angle pulse is applied, followed by dephasing and rephasing gradient pulses.

2.1.5 Radiofrequency Coils

The radiofrequency (RF) coils are responsible for the spin excitation and signal reception during the MRI scans. They can be divided into transmit coils, receive coils, and transceiver coils (capable of transmitting and receiving signal using the same RF coil).

2.1.5.1 Transmit Coils

The transmit RF coil is responsible for the spin excitation. They are designed with the intention of producing a homogenous circularly polarized magnetic field (B_1^+) over the entire region of interest. To protect the subjects against overheat or tissue damage, their design and operation must follow the guidelines for power deposition and specific absorption rate defined by the regulatory agencies (e.g. FDA and IEC).

The most widely used RF transmit coil in MRI scanners is the Birdcage coil (Figure 9). The Birdcage whole body coil is available already integrated into the scanner system in virtually all modern MRI clinical scanners with field intensity equal or below 3 Tesla. It is usually driven in quadrature mode (2 channels, spatially apart by 90 degrees in cylindrical coordinates). In clinical scanners with field intensity equal to or below 3 Tesla, the birdcage whole body coil is used for spin excitation of any part of the human body, including head, torso, and extremities. However, in MRI scanners with field intensity greater than 3 Tesla, the Body coil is not implemented in the system, because it fails to provide homogenous B_1^+ over large regions of interest (e.g., head and torso). Therefore, more advanced RF coil construction and methodology must be pursued; this subject will be explored in section 2.1.6

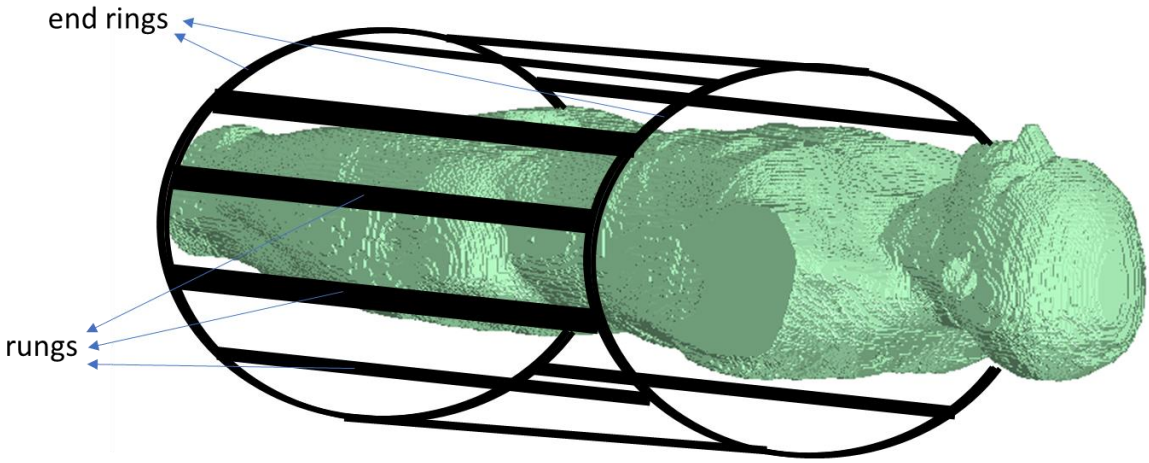

Figure 9: Simplified ilustration of the Birdcage RF body transmit coil. Integrated to the scanner systems with field intensity 3 Tesla or lower, this is the most used coil in commercial cilindrical MRI scanners.

2.1.5.2 Receive Coils

While the birdcage body coil is excellent in generating homogenous B_1^+ fields at 3T or below, this coil does not perform well when receiving MR signal: as the rungs of the birdcage are far from the region being scanned (the birdcage body coil is made to accommodate multiple body shapes) the received signal is relatively low. Additionally, it captures noise from the entire volume. Therefore, the signal-to-noise ratio (SNR) is very low for these coils working as a receiver (or transceiver). Moreover, modern acquisition techniques, such as parallel reception, utilize multiple coil elements to achieve high SNR and acquisition speed; these techniques are not suitable for the quadrature birdcage, which are typically built with only two channels.

Modern MRI scanners utilize a localized receive array for signal reception, normally ranging from 8 channels up to 64 channels. These receive coils are designed to be positioned as

close as possible to the portion of the body being scanned, which can be the torso, body extremities, or head and neck. The proximity of the region of interest combined with the higher number of coil elements provides excellent SNR and the possibility to use high acceleration factors for image acquisition. Figure 10 shows an example of receive array for head imaging; several loops are located close to the head.

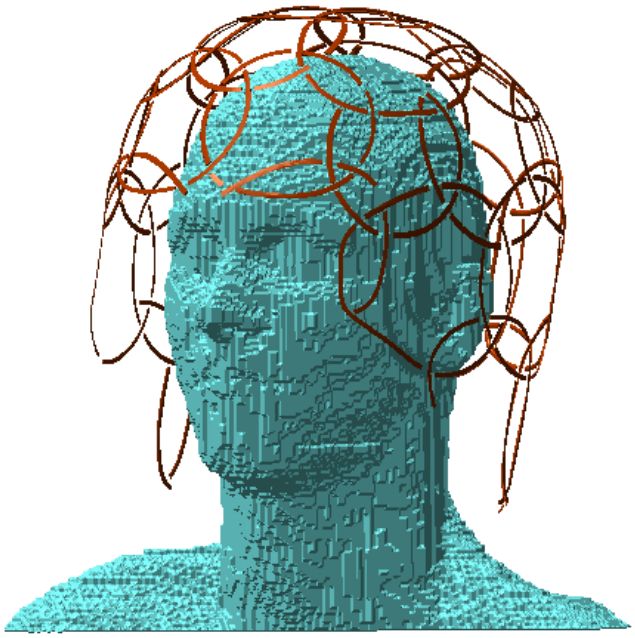

Figure 10: Illustration of a receive radiofrequency array composed of several loop coils.

2.1.6 Ultra-high-field MRI

Ultra-high-field (UHF) MRI is defined as scanners that work with 7T or higher static magnetic field. Among them, the most common is the 7T scanner, which was recently cleared by the regulatory agency FDA to be used clinically.

The major advantage in UHF MRI systems is the increased signal-to-noise ratio in the acquisitions. This is due to the increased active spins at higher fields (number of active spins is proportional to the magnetic field applied), which increases the intensity of the net magnetization vector (Figure 2). The improved SNR can be used to increase the resolution of the images or to decrease the scan time (with the use of higher acceleration factors). The higher field strength also enhances susceptibility effects, increasing the contrast in functional MRI (fMRI) and the vasculature conspicuity in susceptibility weighted imaging (SWI), shown in Figure 11. The longer T1 and shorter T2 and T2* constants can also enhance the contrast in structural images.

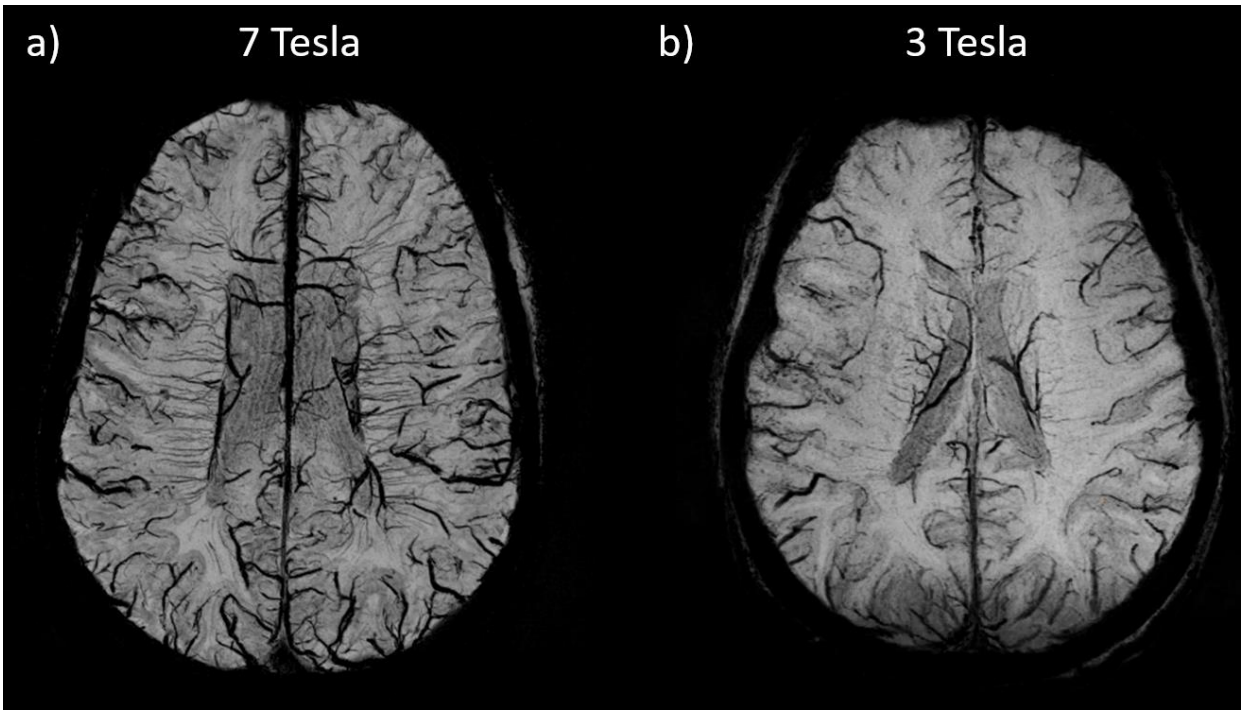

Figure 11: Susceptibility Weighted Imaging (SWI) comparison between 7 Tesla (a) and 3 Tesla (b), with minimal intensity projection of 15 mm in foot-head direction. At 7T, there is higher conspicuity of the veins, making it possible to observe small veins in the brain. The sequence parameters for the 7T acquisition are: 3D SWI, TE/TR = 8.16/23ms, resolution 0.375x0.375x1.5 mm3, acquisition time = 8 minutes, acquired using the Tic-Tac-Toe RF system. The sequence parameter for the 3T acquisition are: 3D SWI, TE/TR = 20/28, resolution 0.5x0.5x1.5 mm3, acquisition time = 9 minutes.

However, the shorter wavelength (see the comparison in Figure 12a) and the reduced skin depth can cause severe inhomogeneities in the spatial distribution of the radiofrequency fields. Regarding the B_1^+ field distribution, the inhomogeneities can cause regions of low contrast or voids in the image, substantially decreasing its diagnostic capabilities and potentially preventing brain abnormalities from being detected. Figure 12b shows an example of severe dropout in the signal

in a 7T high-flip-angle image acquisition using a commercial RF coil; the lower regions of the brain suffers a severe dropout in the signal.

The shorter wavelength, higher conductivity, and reduced skin depth also cause an increase in the power deposition in the tissues, measured by the specific absorption rate (SAR). Both the average and the peak SAR are affected, where the peak SAR is a major concern: the shorter wavelength can cause small regions with high SAR, which can increase local temperature and cause tissue damage. The peak SAR is challenging to be measured/calculated since it requires precise and reliable electromagnetic simulations and cannot be measured in-vivo during an MRI scanning.

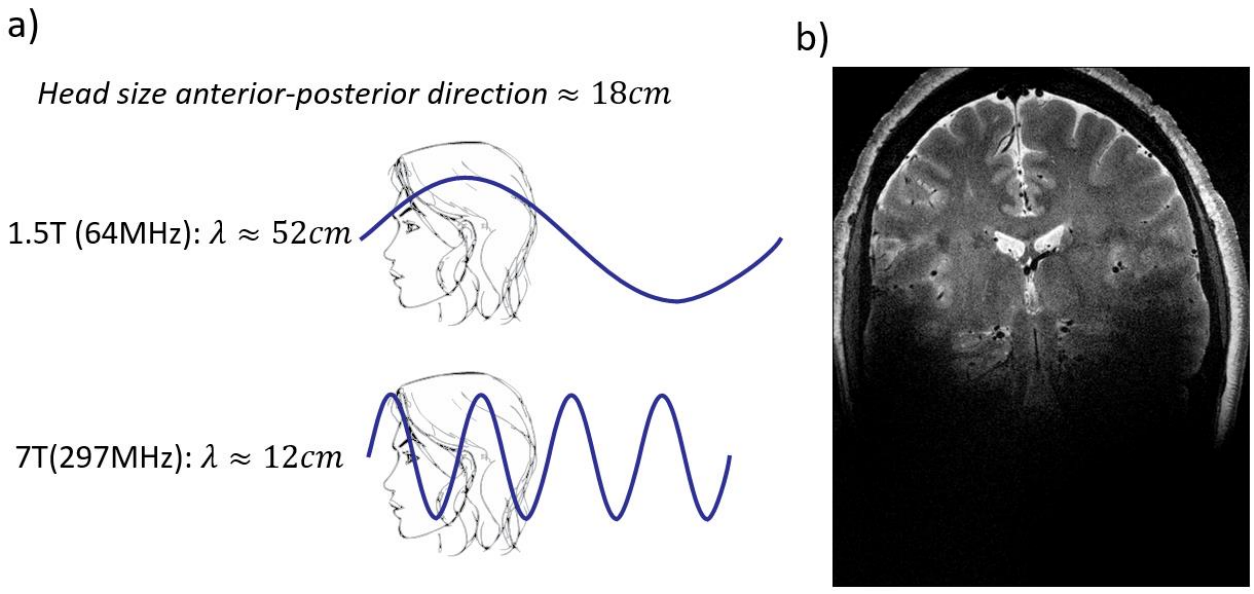

Figure 12: RF inhomogeneities at 7T MRI. In a), the schematic comparing 1.5 Tesla and 7 Tesla RF wavelength inside the tissues. In b), an in-vivo high-flip-angle sequence acquisition at 7T using a commercial RF coil, showing a severe signal dropout in the lower parts of the brain

2.2 Electromagnetic Simulations

Electromagnetic simulations are important in ultra-high field MRI because the B_1^+ field distribution and SAR maps cannot be estimated analytically. Using electromagnetic simulations, the B_1^+ field distribution can be estimated and optimized to improve homogeneity and efficiency. The average and peak SAR can also be estimated and reduced, assuring that SAR levels are below the regulatory and safety limits. The following subsections describe the Finite-difference time-domain (FDTD) method, which approximates Maxwell's equations and was used for the electromagnetic simulations in this work.

2.2.1 Maxwell's Equations

Maxwell's equations model the electromagnetic waves propagation. The derivative form of Maxwell's equations is shown in Equation 2-3, for a medium without Electric or Magnetic sources.

$$\begin{aligned} \frac{\partial \boldsymbol{B}}{\partial t} &= -\nabla \times \boldsymbol{E} - M && \text{Faraday's law} \\ \frac{\partial \boldsymbol{D}}{\partial t} &= -\nabla \times \boldsymbol{H} - J && \text{Ampere's law} \\ \nabla \boldsymbol{D} &= 0 && \text{Gauss' law} \\ \nabla \boldsymbol{B} &= 0 && \text{Gauss' law} \end{aligned} \qquad \text{2-3}$$

where $\boldsymbol{B}$ is the magnetic flux density, $\boldsymbol{E}$ is the electric field, $\boldsymbol{D}$ is the electric flux density; $\boldsymbol{H}$ is the magnetic field, M is the magnetic current density; and J is the electric current density.

In an isotropic, linear, and nondispersive media, the magnetic flux and the magnetic field are related to the magnetic permeability (μ): $\boldsymbol{B} = \mu \boldsymbol{H}$. Similarly, the electric flux and the electric field are related to the electric permittivity (ε): $\boldsymbol{D} = \varepsilon \boldsymbol{E}$. Therefore, Maxwell's equation can be written as Equation 2-4 for isotropic, linear, and nondispersive media and not enclosing a source.

$$\frac{\partial \boldsymbol{H}}{\partial t} = -\frac{1}{\mu}\Delta \times \boldsymbol{E} - \frac{1}{\mu}\sigma^{*}\boldsymbol{H}$$
$$\frac{\partial \boldsymbol{E}}{\partial t} = -\frac{1}{\varepsilon}\Delta \times \boldsymbol{H} - \frac{1}{\varepsilon}\sigma \boldsymbol{E} \qquad \text{2-4}$$

where σ is the electric conductivity and σ^{*} is the equivalent magnetic loss.

2.2.2 Yee Cell

The Yee cell is a discrete approximation of the domain of interest in electromagnetic simulations. The basic Yee cell is designed in a manner that every Electric field component is surrounded by four Magnetic field components, and every Magnetic field component is surrounded by four Electric field components. Figure 13 shows the cubic Yee cell, which was used in this work. Other types of cells are possible, such as rectangular, curved, triangular, among other geometries.

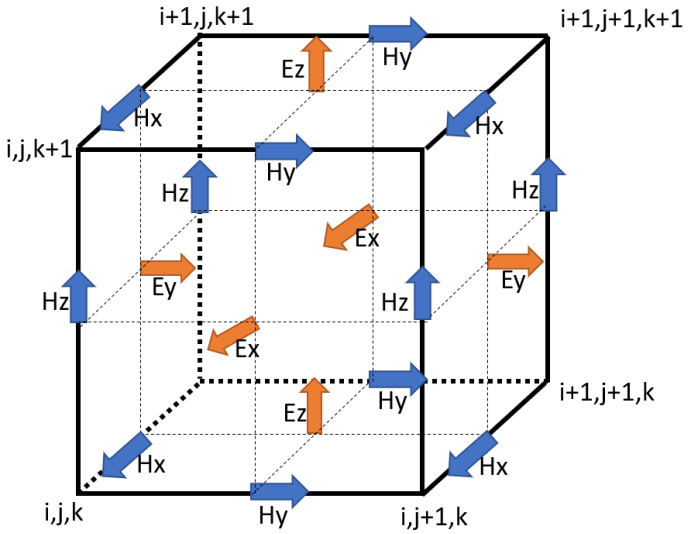

Figure 13: The yee cell. Every Electric field (E) component is surrounded by four Magnetic fields (H) components, and every H component is surrounded by four E components. i,j,k represents Cartesian coordinates. x,y,z represents the directions in Cartesian space.

2.2.3 The Finite-Difference-Time-Domain Method

The finite-difference-time-domain (FDTD) method aims to numerically solve Maxwell's curl equations using second-order approximations. The set of Equations 2-4 can be rewritten in Cartesian coordinates, resulting in the set of Equations 2-5, also valid for isotropic, linear, and nondispersive media, and not enclosing a source.

$$\frac{\partial H_x}{\partial t} = -\frac{1}{\mu}\left[\frac{\partial E_z}{\partial y} - \frac{\partial E_y}{\partial z} + \sigma^* H_x\right]$$

$$\frac{\partial H_y}{\partial t} = -\frac{1}{\mu}\left[\frac{\partial E_x}{\partial z} - \frac{\partial E_z}{\partial x} + \sigma^* H_y\right]$$

$$\frac{\partial H_z}{\partial t} = -\frac{1}{\mu}\left[\frac{\partial E_y}{\partial x} - \frac{\partial E_x}{\partial y} + \sigma^* H_z\right]$$

$$\frac{\partial E_x}{\partial t} = \frac{1}{\varepsilon}\left[\frac{\partial H_z}{\partial y} - \frac{\partial H_y}{\partial z} + \sigma E_x\right] \qquad 2\text{-}5$$

$$\frac{\partial E_y}{\partial t} = \frac{1}{\varepsilon}\left[\frac{\partial H_x}{\partial z} - \frac{\partial H_z}{\partial x} + \sigma E_y\right]$$

$$\frac{\partial E_z}{\partial t} = \frac{1}{\varepsilon}\left[\frac{\partial H_y}{\partial x} - \frac{\partial H_x}{\partial y} + \sigma E_z\right]$$

Considering that the *H* fields are updated at the time-step n, and the *E* fields are updated at the time step $n + \frac{1}{2}$, the set of equations 2-5 can be written in the fine-difference form (Equation 2-6), demonstrated only to E_x for brevity, but it can be expanded to the all E and H fields by analogy.

$$\frac{E_x\big|_{i,j+\frac{1}{2},k+\frac{1}{2}}^{n+\frac{1}{2}} - E_x\big|_{i,j+\frac{1}{2},k+\frac{1}{2}}^{n-\frac{1}{2}}}{\Delta t}$$

$$= \frac{1}{\varepsilon_{i,j+\frac{1}{2},k+\frac{1}{2}}}\left(\frac{H_z\big|_{i,j+1,k+\frac{1}{2}}^{n} - H_z\big|_{i,j,k+\frac{1}{2}}^{n}}{\Delta y} - \frac{H_y\big|_{i,j+\frac{1}{2},k+1}^{n} - H_y\big|_{i,j+\frac{1}{2},k}^{n}}{\Delta z}\right.$$

$$\left. - \sigma_{i,j+\frac{1}{2},k+\frac{1}{2}} \cdot \frac{E_x\big|_{i,j+\frac{1}{2},k+\frac{1}{2}}^{n+\frac{1}{2}} - E_x\big|_{i,j+\frac{1}{2},k+\frac{1}{2}}^{n-\frac{1}{2}}}{2}\right)$$

$$E_x\big|_{i,j+\frac{1}{2},k+\frac{1}{2}}^{n+\frac{1}{2}} =$$

2-6

$$\frac{\left(1 - \frac{\sigma_{i,j+\frac{1}{2},k+\frac{1}{2}}\,\Delta t}{2\varepsilon_{i,j+\frac{1}{2},k+\frac{1}{2}}}\right)}{\left(1 + \frac{\sigma_{i,j+\frac{1}{2},k+\frac{1}{2}}}{2\varepsilon_{i,j+\frac{1}{2},k+\frac{1}{2}}}\right)} E_x\big|_{i,j+\frac{1}{2},k+\frac{1}{2}}^{n-\frac{1}{2}}$$

$$+ \frac{\left(\frac{\Delta t}{\varepsilon_{i,j+\frac{1}{2},k+\frac{1}{2}}}\right)}{\left(1 - \frac{\sigma_{i,j+\frac{1}{2},k+\frac{1}{2}}\,\Delta t}{2\varepsilon_{i,j+\frac{1}{2},k+\frac{1}{2}}}\right)}\left(\frac{H_z\big|_{i,j+1,k+\frac{1}{2}}^{n} - H_z\big|_{i,j,k+\frac{1}{2}}^{n}}{\Delta y}\right.$$

$$\left. - \frac{H_y\big|_{i,j+\frac{1}{2},k+1}^{n} - H_y\big|_{i,j+\frac{1}{2},k}^{n}}{\Delta z}\right)$$

The FDTD method is based on Equation 2-6. For each time step, the E fields and the H fields are updated. The simulations are run until the steady state is achieved, usually in the order

of 100,000 to 300,000 time-steps for the simulations presented in this work. On the edges of the region of interest, perfect matching layers are implemented to absorb the irradiating electromagnetic waves.

2.2.4 Transmission Line Modeling

An accurate estimation of the scattering parameters is important as it gives information about the coupling among the transmit channels, the reflection coefficient, and the bandwidth/Q-factor of the transmit elements of the RF coil. A virtual transmission line, independent of the FDTD simulations, was modeled according to Equation 2-7 and Figure 14.

$$I_{k+\frac{1}{2}}^{n+\frac{1}{2}} = I_{k+\frac{1}{2}}^{n-\frac{1}{2}} - \frac{1}{Z_0}\frac{v\Delta t}{\Delta \mathrm{x}}\left(V_{k+1}^{n} - V_{k}^{n}\right)$$
$$V_{k}^{n+1} = V_{k}^{n} - Z_0\frac{v\Delta t}{\Delta \mathrm{x}}\left(I_{k+\frac{1}{2}}^{n+\frac{1}{2}} - I_{k-\frac{1}{2}}^{n+\frac{1}{2}}\right) \qquad 2\text{-}7$$

where I is the current, V is the voltage, k is the spatial location (from 0 to end), n is the iteration, v is the velocity of the traveling wave, Δt is the time step, Δx is the spatial step, and Z_0 is the characteristic impedance of the transmission line.

The virtual transmission line can be integrated with the FDTD domain by the V_{end} and $I_{end+\frac{1}{2}}$. Equation 2-8 shows the example of a transmission line being injected in the +Z direction.

$$\mathrm{E_z}(i,j,k-1-m) = \frac{V_{end}^{n}}{\Delta x * L}$$

$$I_{end+\frac{1}{2}}^{n+\frac{1}{2}} = I_{end+\frac{1}{2}}^{n-\frac{1}{2}} - \Delta x\left(H_x^{n+\frac{1}{2}}(i,j-1,k-1) + H_x^{n+\frac{1}{2}}(i,j,k-1)\right) + \qquad \text{2-8}$$

$$\Delta y\left(H_y^{n+\frac{1}{2}}(i-1,j,k-1) + H_y^{n+\frac{1}{2}}(i,j,k-1)\right)$$

where E_z is the Electric field component, L is the distance between the strut and the shield, m variants from 1 to L, H_x and H_z are the Magnetic field components, Δx and Δy are the spatial steps in the x and y from the Cartesian coordinates, i, j, k are the position of the transmission line interface with the FDTD domain.

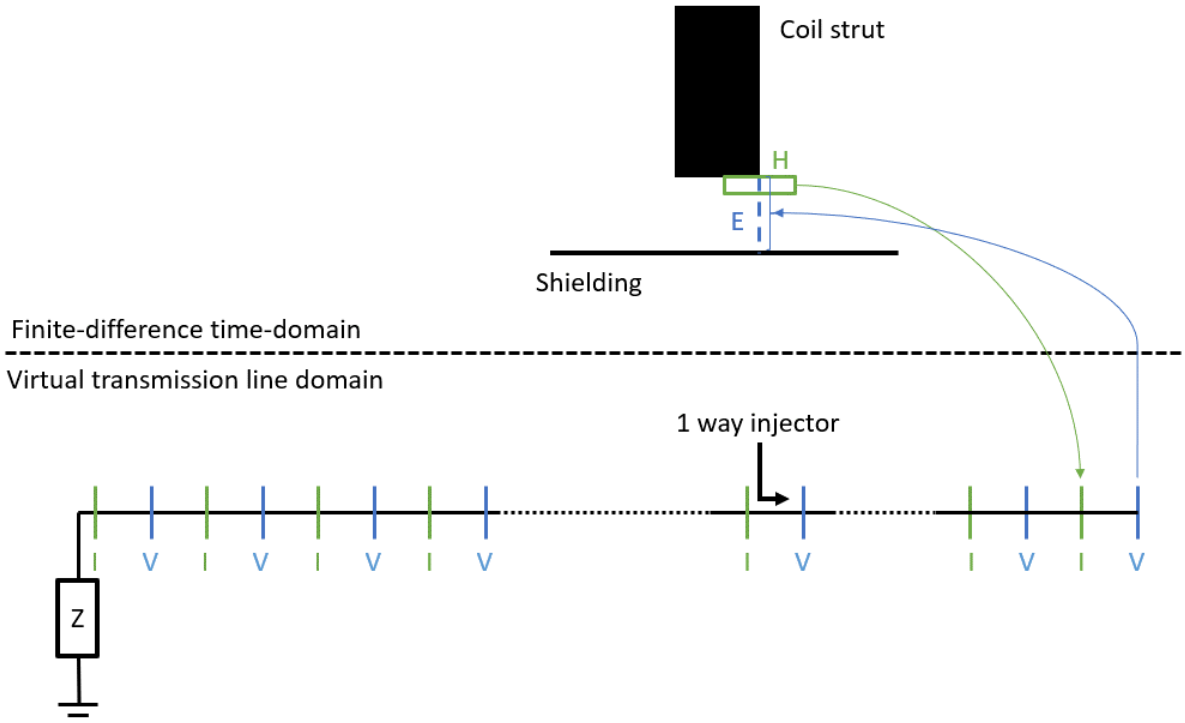

Figure 14: Schematic of the transmission line model and its integration with the FDTD.

2.2.5 Superposition Principle and RF Shimming

The superposition principle is valid for Electromagnetic waves and it states that the resultant electromagnetic wave is equivalent to the sum of the individual components. Figure 15 illustrates the interaction between two waves traveling in opposite directions in the one-dimensional space; it can occur either constructive electromagnetic interactions (Figure 15a) or destructive interactions (Figure 15b). The same principle is valid for the three-dimensional space and for multiple sources of electromagnetic waves.

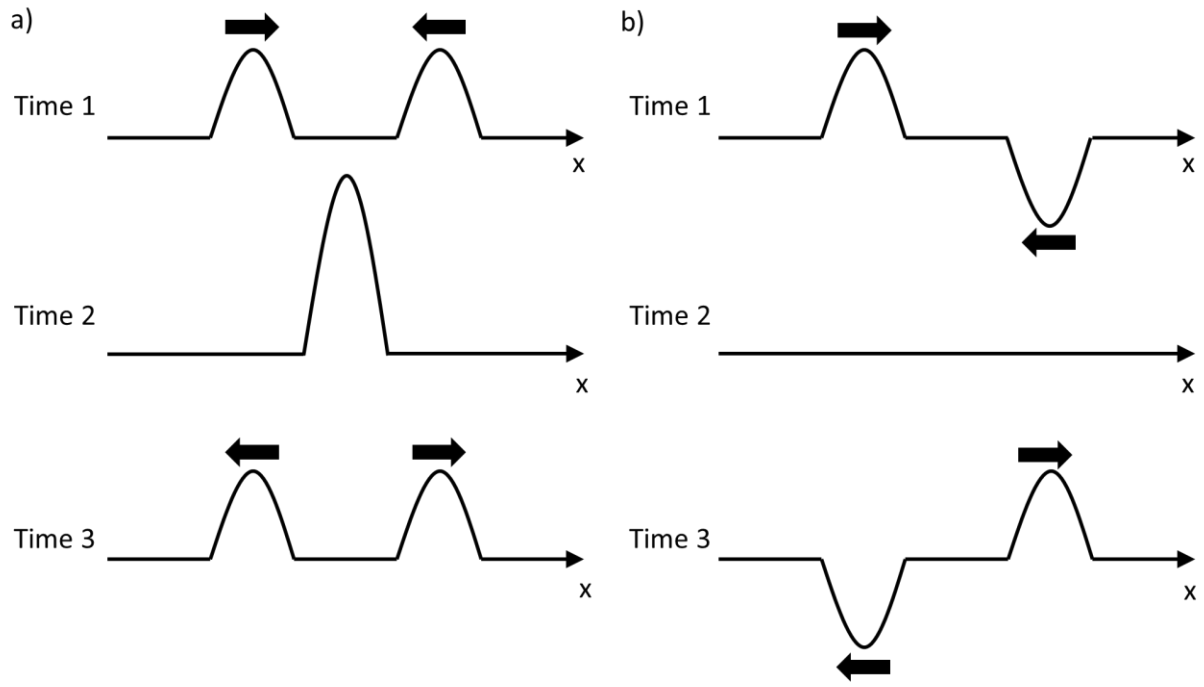

Figure 15: illustration of the superposition of two waves traveling in one-dimensional space. In a), constructive wave interaction; In b), destructive interaction.

The superposition principle can be used to manipulate the Magnetic and Electric field inside the media. This can be done by positioning several coils/antennas around the media (Figure 16) and optimizing the amplitude and phase of each coil/antenna that achieves the desired RF performance inside the media. In MRI, this technique is known as RF shimming, and it can be used to optimize the B_1^+ field distribution (usually for improving homogeneity and efficiency) and reduce the peak and average SAR in the tissues. This technique will be used in several Chapters of this dissertation.

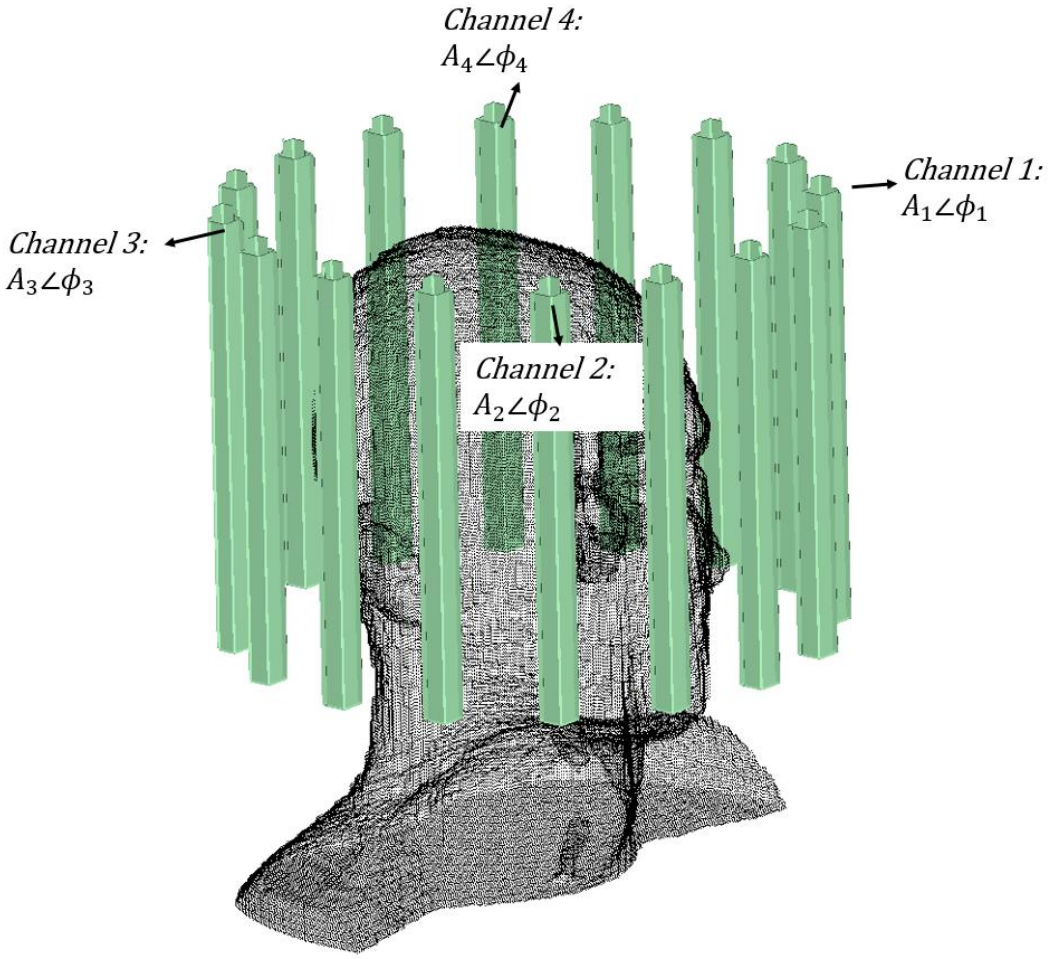

Figure 16: The superposition principle allows that several channels position around the head can have its phases and amplitudes optimized towards a specific objective, usually to improve the B_1^+ homogeneity and efficiency and to minimize the SAR. A_n is the the amplitude of the signal in the channel n; ϕ_n is the phase of the signal in the channel n.

3.0 Foot and Ankle RF System for UHF MRI

3.1 Introduction

Magnetic resonance imaging (MRI) has been used to investigate a wide range of abnormalities, injuries and diseases related to musculoskeletal tissues, such as cartilage degeneration [38, 39], bone marrow edemas [40], osteoarthritis [37, 39-41], osteoporosis [39, 42], and ligament/tendon insures [37, 43]. While most of the clinical applications rely on images acquired at 1.5 or 3 Tesla (T) scanners, the enhanced contrast and signal-to-noise ratio (SNR) provided by ultra-high field (UHF, ≥7T) MRI can be highly attractive for musculoskeletal imaging [44]. The increased SNR can be traded to increase the spatial resolution of the images [16] or to decrease the scan time [45] (although the T1 relaxation is longer at UHF, higher levels of accelerations can be used due to the increased SNR). On the other hand, the increased B_1^+ (circularly polarized magnetic field responsible for excitation) inhomogeneities, increased chemical shift, and increased peak and average specific absorption ratio (SAR) present great challenges in the translation of the UHF research to a reliable clinical standard [13].

To address the problems in B_1^+ inhomogeneity and high SAR, multi-channel radiofrequency coils have been developed for various parts of the body [46]. Moreover, due to the lack of integrated body coil in UHF scanners (usually available at 1.5T and 3T scanners), the RF coil must work as either a transceiver or transmit (Tx)-only/receive (Rx)-only pairs should be built. Additionally, radiofrequency (RF) shimming techniques can potentially improve the B_1^+ homogeneity and efficiency in a specific region of interest, while reducing the global and local SAR [47-49].

To the best of our knowledge, there are few research groups that have developed RF coils specific for 7T imaging of the foot/ankle [50, 51], as most of the studies use commercial knee coils [2, 43, 52-55] or head coils [56-59] for imaging these parts of the body. This is not optimal because the subject may be asked to stay in an uncomfortable position (e.g., foot in a high angle) and the coil may not be suitable and/or optimal for all foot sizes.

In this study, we provide details and design parameters for a 7T transmit (Tx) RF coil dedicated for foot and ankle imaging. The design was adapted from the Tic-Tac-Toe concept utilized in imaging for a wide variety of body organs at 7T [25, 26, 29-31, 33]. The coil's magnetic and electric field distributions, input impedance, coupling matrix were simulated using the finite-difference time-domain (FDTD) method in a homogenous cylindrical phantom model. The B_1^+ maps and scattering parameters of the constructed RF coil were experimentally measured in a cylindrical phantom with assigned conductivity and permittivity equal to the average values present in the lower leg of the Duke model (IT'IS Foundation, Switzerland) and the results were compared with the simulations. The coil's SAR and B_1^+ field distributions calculated inside Duke's anatomically detailed lower leg human model were also attained using FDTD method. Finally, in-vivo B_1^+ mapping and preliminary images using T2-DESS sequence were acquired without the use of a dedicated Rx-only insert.

3.2 Methods

3.2.1 Transmit Coil Design

A Tx RF coil for foot and ankle imaging at 7T was designed based on the Tic-Tac-Toe (TTT) family (a Tx RF coil design inspired by the cross-pole antenna [25-27, 29-31, 60]). The Tx RF coil is composed of eight squared-shape transmission lines, electrically connected to each other in a 2x2 Tic-Tac-Toe format (Figure 17a and Figure 17b). The dimensions of the coil were 228.6 x 228.6 mm^2 in *XY* directions and 16.8mm in *Z* direction, which is the direction of the static magnetic field (B_0) (see Figure 17a). The inner rods of the transmission lines were made of solid squared-shape copper (McMaster-Carr, USA), with the cross-section dimensions of 6.35x6.35mm^2 (see Figure 17b). The outer strut was built from an 8μm think single-layered copper sheet (Polyflon, Germany). A 3D-printed polycarbonate inner dielectric was designed using Solidworks (Solidworks, USA); it offered support for both the inner rods and outer struts, and defined the relative permittivity of the inner core of the transmission line to be equal to 2.4. The complete assembly of the 4-channel transmit array is shown in the Figure 17a.

The center pin of the excitation transmission lines was connected to the outer strut of the coil while the inner rod was connected to the shield/ground. Matching and tuning rods were placed in an alternated fashion, so that the coil had 4 excitation ports with matching rods, and 4 tuning rods, without excitation (Figure 17b). The Tx RF coil can be tuned and matched to 50 Ohms at 297.2MHz (Larmor frequency for ^1H at 7T) by changing the rods' lengths, which affect the coil reactance and allows the resonant frequency of the RF circuit to be adjusted to the scanner's Larmor frequency.

An RF shielding composed of double-layered copper sheets – $4\mu m$ thick each layer (or approximately half of skin depth for copper at 7T), with a 0.254mm-thick dielectric in between (Polyflon, Germany) – was placed to cover the transmitting elements as described in Figure 17. Split cuts were made in the copper sheets to effectively open the low-frequency eddy currents (induced as a result of the gradient fields) pathways, thus avoiding the potential fast gradient switching artifacts while maintaining the RF characteristics associated with the Tx coil as described in [60]. The shields were extended to enclose the entire lower leg, except for a cavity on the top to accommodate the toes, thus allowing all sizes of feet and placement positions (Figure 17d and Figure 17e). The overall size of the coil is 250x250x290mm^3 (Figure 17e).

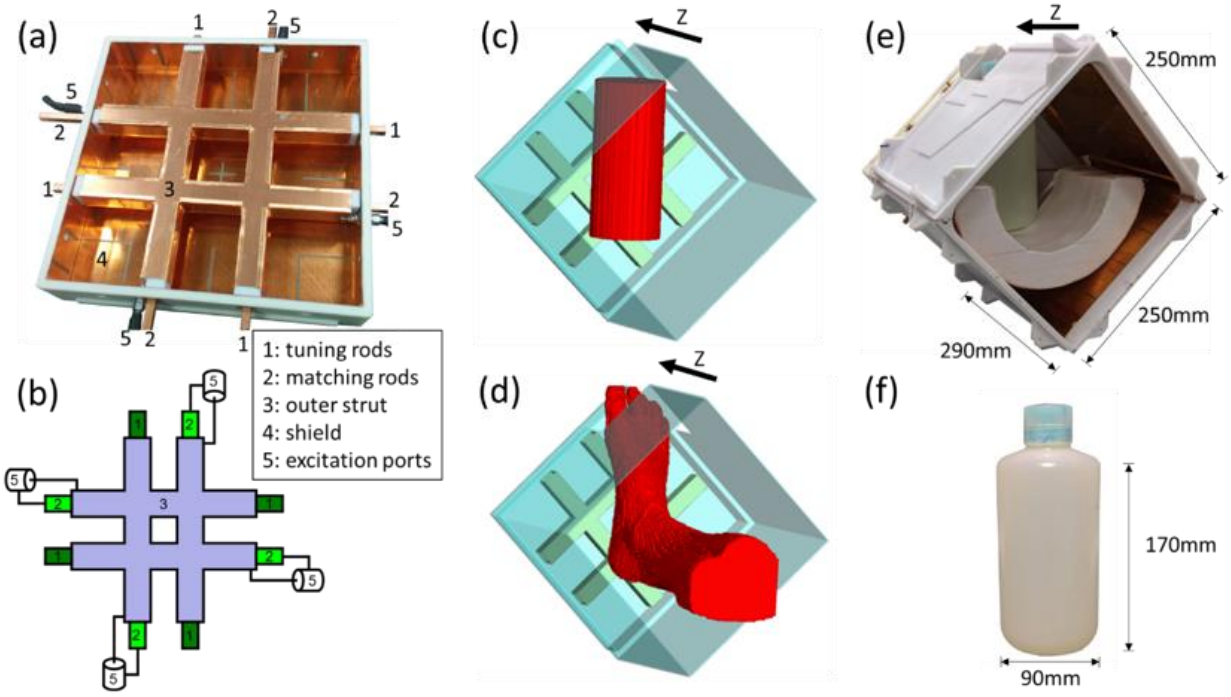

Figure 17: Design of the TTT foot and ankle Tx RF coil. In (a), the assembled coil without the shielding frame. In (b), the schematic of the RF coil. In (c), the FDTD grid of the simulated coil with a homogenous phantom as the load. In (d), the FDTD grid of the RF coil including the right lower leg model extracted from Duke model. In (e), the assembled coil, with the external shielding frame and the homogenous phantom. In (f), the homogeneous phantom used in the B_1^+ map acquisition, having relative permittivity of 39 and conductivity of 0.49 S/m (average values from the lower leg of the Duke model).

The lengths of the inner rods for tuning/matching of the RF coil were estimated using finite-difference time-domain (FDTD) simulations, and then fined-tuned in the bench while the coil was loaded with a homogenous phantom – that corresponds to the averaged values of permittivity and conductivity of the Duke virtual family model at 297MHz. The coupling of the RF coil is inherently high by its design [26]; therefore, changing one rod can affect all the channels. The s-

matrix was measured using a network analyzer (Model E5062A, manufactured by Agilent Technologies).

3.2.2 Finite-Difference Time-Domain Simulations

The coil structure was modeled using Matlab (MathWorks, USA), and the FDTD grid was exported in a regular-spaced grid with 300x300x304 Yee-cells and resolution of 1.6mm in all directions: X, Y, and Z. A validated in-house developed finite-difference time-domain (FDTD) software [61] was used to simulate the RF behavior of the coil/shields on a homogeneous phantom (Figure 17c) and the anatomically detailed human lower leg model (Figure 17d). The FDTD package incorporates true transmission line modeling for capturing the mechanism of excitation and reception, and, therefore, accurately predicting coil input impedance and coupling between coil elements [25, 26, 62, 63].

The pulse used in the FDTD model was a modified differentiated Gaussian pulse with a period of 5.7ns. The temporal resolution was 1ps and the simulation ran for 100.000 times steps, what is equivalent to 50 periods of the pulse, which was enough time to achieve steady state. The transmission line voltage (V) and current (I) in the time domain were stored and the s-parameters were calculated based on the transmit and reflected signal in the channels and the isolated input pulse.

The human lower leg model was extracted from the Duke model, and the homogenous phantom was simulated with relative permittivity of 39 and conductivity of $0.49\ S/m$, both values derived from the average values of the lower leg Duke model. The FDTD software generates the frequency domain (by Discrete Fourier Transform (DFT) of the time domain data) of the Electric (E) and Magnetic (B) fields (in all directions of the Cartesian space). Each individual channel was

simulated using a local cluster computer, 6 threads per channel, totaling about 8 hours of computational time. The B_1^+ field was extracted, and the associated SAR was calculated by Equation 3-1 and averaged per 10g of tissue.

$$SAR(x,y,z) = \frac{0.5*\sigma(x,y,z)*|\bar{E}|^2(x,y,z)}{\rho(x,y,z)} \quad 3\text{-}1$$

where σ is the conductivity in S/m, $\bar{E}$ is the electric field vector in V/m, ρ is the density in kg/m^3, and x, y, z are the positions in the Cartesian coordinates.

In addition to SAR values, the B_1^+ field distribution was evaluated using three metrics: 1) coefficient of variation (CV), which is a global homogeneity metric defined by the standard deviation divided by the mean of the signal in a region of interest; 2) maximum of the signal divided by the minimum (max/min), which accounts for local signal voids and bright spots; and 3) mean value of the signal, which measures the efficiency of the RF coil.

3.2.3 Experiments

The coil was tested in a 7T Human Scanner (Siemens Magnetom, Germany). A transmit/receive (T/R) switch box was utilized so that the same RF coil could be used to transmit and receive signal. The system can operate either in the single-channel mode, using a 4-way Wilkinson power splitter, or it can use the pTx mode available in the scanner to operate as a 4-channel transmit array. Constant phase shifters (with 90-degree increments) were added in the transmission lines to produce 4-port quadrature excitation.

B_1^+ mapping was acquired in a homogeneous cylindrical phantom (Figure 17f) and in-vivo. The phantom is composed of 80% of denatured ethanol, 20% of water, and 9.85g/L of sodium chloride [64]. The in-vivo scans were conducted under a study approved by the University of Pittsburgh Institutional Review Board. The sequence used was a saturated turbo FLASH with the following parameters: TE/TR = 1.09/3000ms, resolution 3.1x3.1x3.1mm^3, FOV 112x200, 36x64 acquisition matrix, six flip-angles for pre-saturation variating from 0 to 90 degrees, total time of scan of 6 minutes. The data was then fitted to a cosine function using MATLAB and the B_1^+ map was calculated and scaled for a total power input of 1W (i.e., 0.25W in each excitation port).

Preliminary in-vivo image acquisition (without the use of a dedicated Rx-only insert) was performed using the 3D T2-DESS sequence, with the following parameters: TE/TR = 5/20ms, resolution 0.62x0.62x0.62mm^3, FOV 200x200, 320x320 acquisition matrix, 25 degrees of flip-angle, acquisition time = 13:56min, and reference voltage = 300V.

3.3 Results

3.3.1 Scattering Parameters

Using the homogeneous cylindrical phantom as a load, a reflection coefficient (S_{xx}) lower than $-20dB$ was achieved (experimentally and with FDTD simulations) for all 4 channels. The comparison between the simulated and measured scattering parameters from one representative channel is shown in the Figure 18a and Figure 18b. Figure 18c shows the measured s-matrix for all four channels of the designed RF coil. The mean measured reflection coefficient was $-30.4dB$, while the average coupling among opposite ports (e.g. S13 and S24) was $-4.11dB$ and the average

coupling among adjacent ports (e.g. S12, S23, …) was $-9.56dB$. Note that high coupling between opposite ports is a unique characteristic of the TTT coil family, which happens at the cost of reduced B_1^+ per input power, but promotes B_1^+ homogeneity and RF field consistency with different loads, as demonstrated in prior studies [25-27, 30, 65].

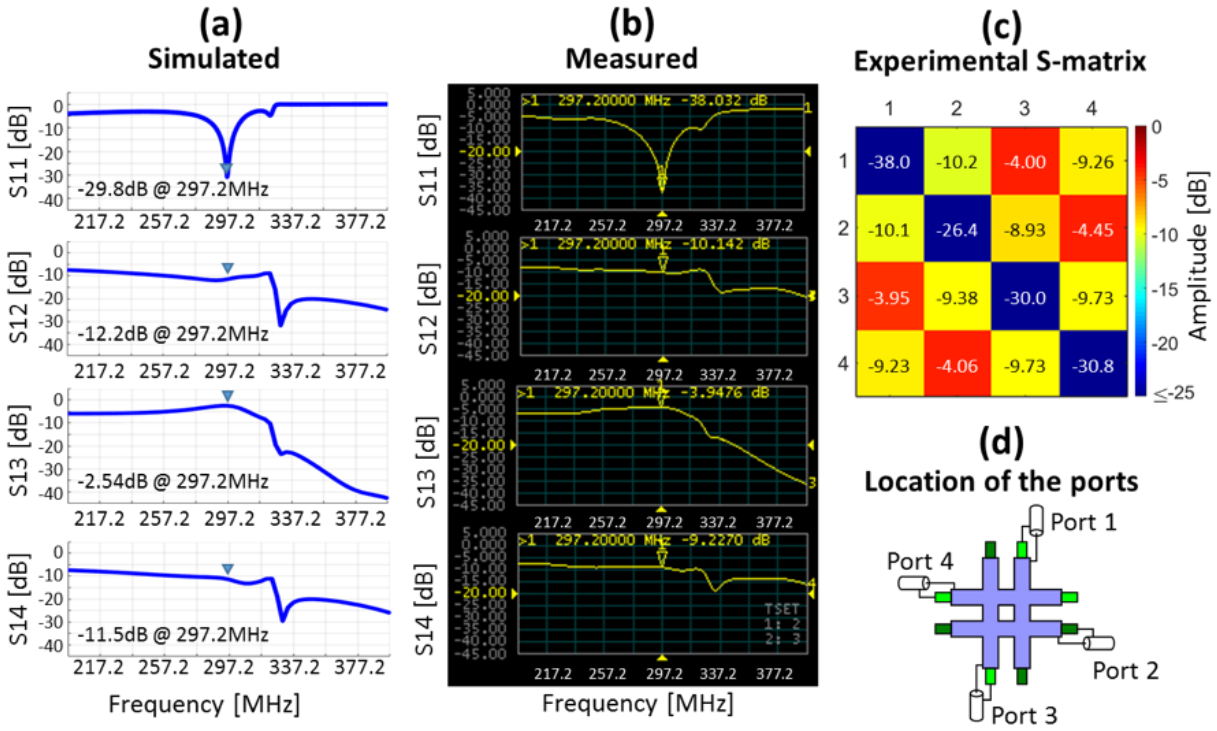

Figure 18: Scattering parameters of the designed RF coil. In (a) the results from FDTD simulations of channel 1. In (b) the experimental measurements of transmit and reflection coefficients of channel 1. In (c) the experimental s-matrix with the measurements from the 4 channels. In (d), the locations of the ports used in the s-parameters simulation and measurement.

3.3.2 Simulated and Experimental Data

Figure 19a presents the B_1^+ field distribution, normalized for 1W of total input power. The average simulated B_1^+ field intensities on the dotted lines are 0.75μT, 0.74μT and 0.76μT in the sagittal, coronal and axial planes respectively. The measured B_1^+ field intensities are shown in the Figure 19b and have the average values, on the dotted lines, of 0.57μT, 0.58μT and 0.61μT for the sagittal, coronal and axial planes, respectively. The simulated and measured B_1^+ fields from the individual channels are shown in the Figure 19d and Figure 19e, respectively.

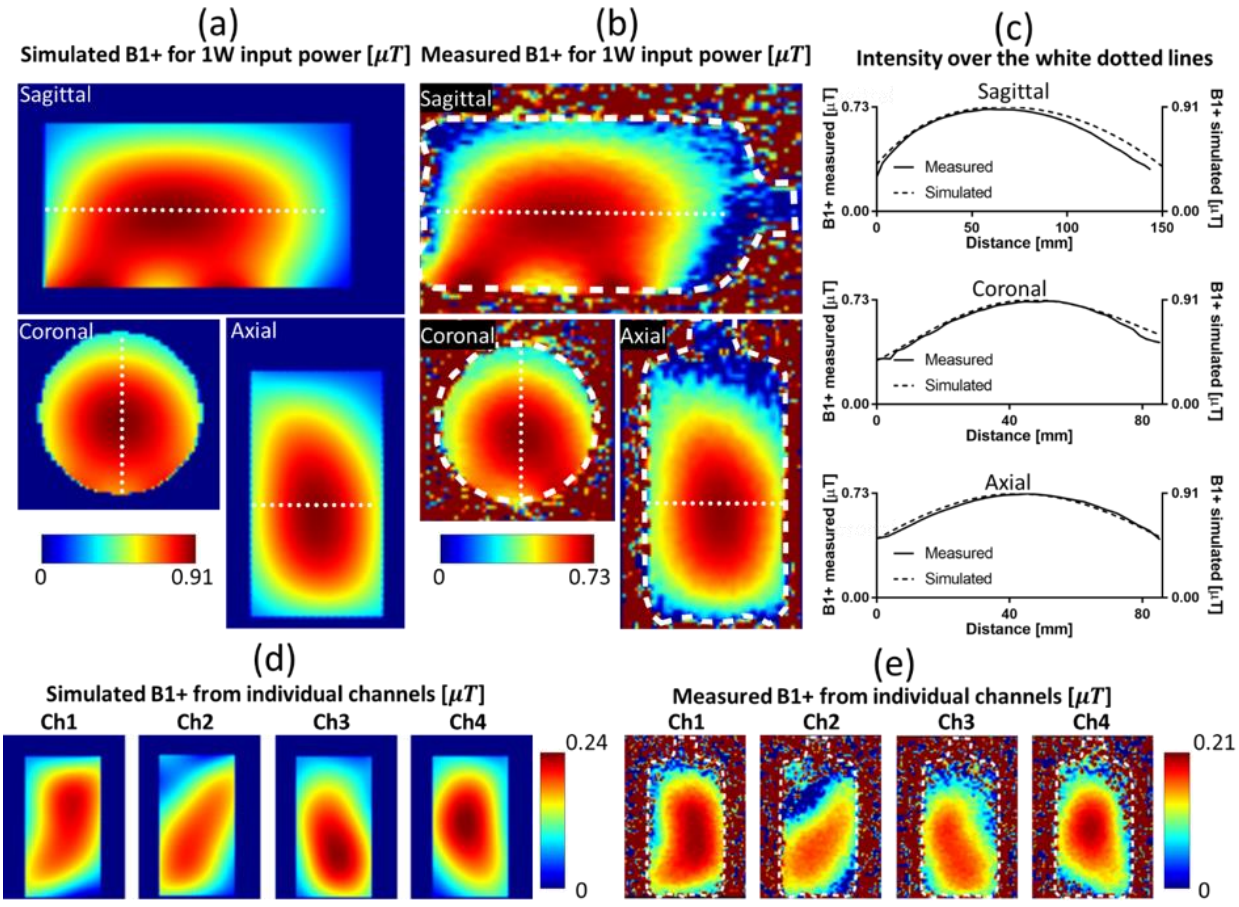

Figure 19: Simulations and measurements in a homogenous phantom with relative permittivity 39 and conductivity 0.49 S/m. In (a), the simulated B_1^+ map for 1W of total input power, calculated from FDTD simulations; In (b), the measured B_1^+ for 1W of total input power; In (c), the intensity plots of the B_1^+ maps over the dotted lines on the figures, in all planes; In (d), the axial slices of the simulated individual channels scaled for 0.25W of input power; In (e), the measured B_1^+ maps of the individual channels scaled for 0.25W of input power.

3.3.3 Imaging

The simulated B_1^+ field and SAR distributions with the lower human leg model are shown in the Figure 20a and Figure 20e respectively, both scaled for 1W of total input power. The peak SAR was 0.34W/Kg for 10g while the average SAR was 0.07W/Kg for 10g over the whole lower leg. The in-vivo B_1^+ mapping is shown in the Figure 4c. The conductivity and relative permittivity maps are shown in the Figure 20b and Figure 20d respectively. Figure 20f shows the three regions of interest (ROI) used to calculate the stats of the simulated B_1^+ fields in the foot/ankle. For the mid foot, the stats are: CV = 28.8%, max/min = 8.13 and mean = 0.43μT. For the calcaneus, the stats are: CV = 15.6%, max/min = 2.76 and mean = 0.56μT. In the ankle, the stats are: CV = 23.9%, max/min = 5.34 and mean = 0.33μT. For the in-vivo measurements (Figure 4c), the mean B_1^+ is equal to 0.29μT, while the average over the entire foot from simulations is equal to 0.42μT. Figure 20g shows a preliminary in-vivo image acquisition in a healthy subject.

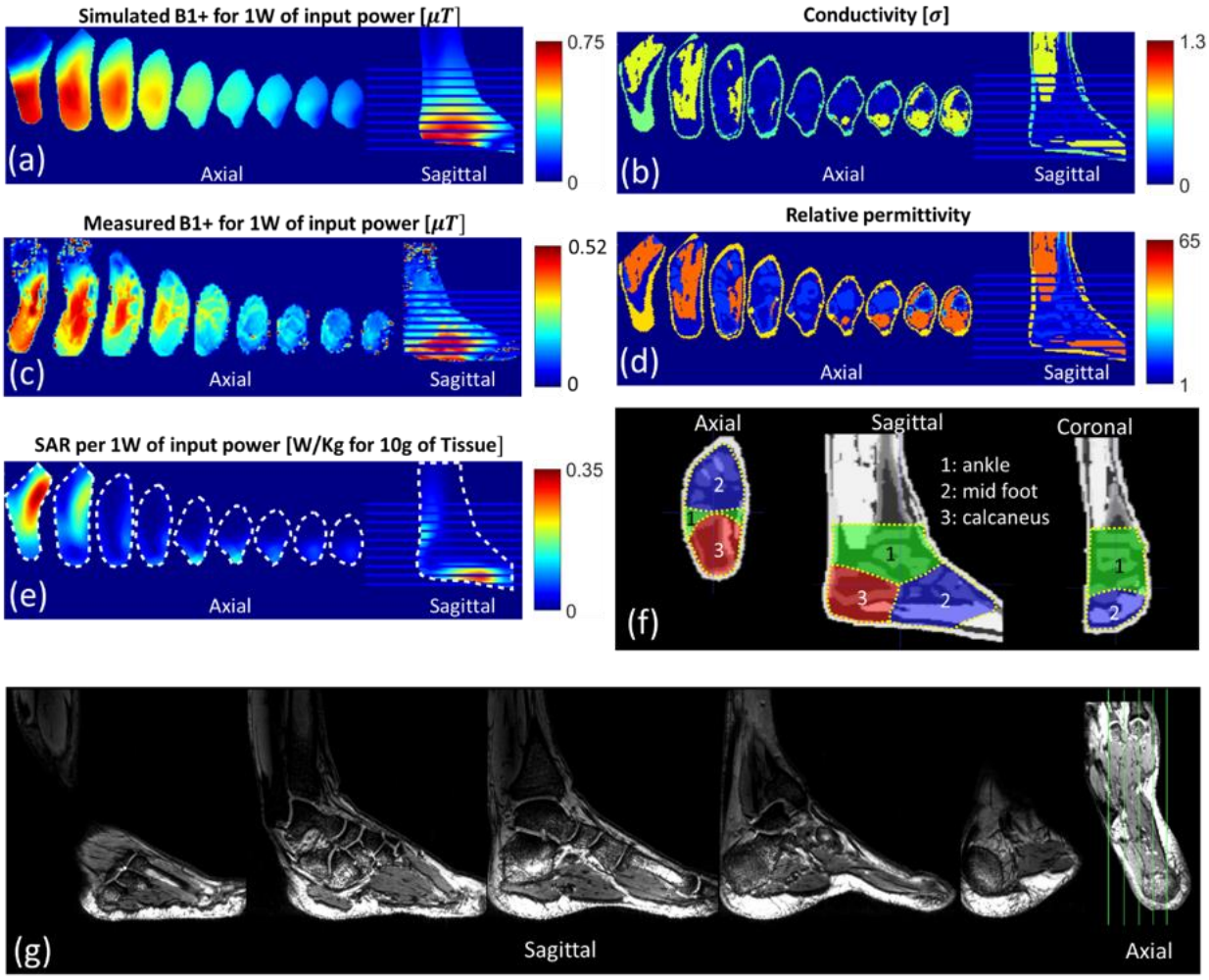

Figure 20: Simulations of the Tx coil with the foot model extracted from Duke virtual family. In (a), the simulated B_1^+ field distribution for 1W of total input power (not accounting for losses in the cables/splitter/TR box); In (b), the conductivity map for the tissues at 297MHz; In (c), the in-vivo B_1^+ mapping, scaled for 1W of total input power; In (d), the relative permittivity map for the tissues at 297MHz; In (e), the SAR map per 1W of total input power; In (f), the regions of interest used to calculate the statistics of the B_1^+ distribution, plotted over the permittivity maps in the three planes; In (g), multiple slices of an in-vivo 3D T2-DESS acquisition at 7T, with a resolution of 0.6mm isotropic.

3.4 Discussion and Conclusion

The lack of Tx body coil for 7T MRI forces the development of transmit coils dedicated for certain parts of the body. Due to the absence of commercial RF coil specific for foot/ankle at 7T, most sites use knee coils [2, 43, 52-55] or head coils [56-59] for imaging the foot/ankle. This situation is not optimal for several reasons. In the case of knee coils (usually have a cylindrical shape and were developed to close fit a knee), the foot has to stay in a high angle position (the recommended position is less than 20 degrees of flexion [37]). This makes imaging unviable in cases like fracture or severe disease that impairs the movement of the foot. In the case of head coils, different sizes of foot may not fit due to the limited space available. The proposed TTT Tx coil has its elements positioned in the XY plane of the scanner; therefore, the foot and ankle can be imaged in a relaxing position. Furthermore, the proposed TTT RF coil does not have any lumped elements as it utilizes distributed capacitances, which help in terms of robustness and manufacturing. Due to the relatively large size and the gap in the RF shielding (Figure 17d), any size of foot and lower leg can be scanned. Moreover, it is possible to adjust the position of the foot based on the region of interest.

An accurate simulation of the coil and the transmission lines is essential to ensure its performance and to predict SAR, since the in-vivo local SAR cannot be accurately measured in real time by the MRI scanner. The precise modeling of the true transmission line excitation was demonstrated by the close matching of the simulated and measured scattering parameters in Figure 18a and Figure 18b, respectively. Slight differences in the offset of transmission for opposite ports (S13) can be explained by losses in the system that were not included in the simulations, such as losses in the cables, coil copper, and connectors. The high coupling between opposite ports in the

array (S13) may decrease the coil efficiency, yet other studies have demonstrated its potential to increase the B_1^+ fields homogeneity, decrease SAR and increase load insensitivity [25-27].

The comparison between the measured and simulated B_1^+ in the homogeneous phantom is highly favorable. Although the model approximates the phantom to a cylindrical structure (the real phantom has a bottleneck to facilitate the filling), the pattern was almost identical (Figure 19a and Figure 19b). Graphs with the B_1^+ intensity over the dotted line were plotted in all 3 planes, and further reinforced the similarities between measured and simulated data. The difference in the scale (about 20%) can be explained by the losses in the cables, coil plug, T/R switch, 4-way splitter and connectors in the coil, that are not included in the simulations. The same level of similarities is seen in the B_1^+ mapping of the individual channels.

The comparison between in-vivo measured and simulated B_1^+ fields reveals a similar pattern of the field distribution. The in-vivo measured B_1^+ mean is about 30% lower, while in the homogenous phantom this difference was about 20% (attributed to splitters/cables/TR box). The additional difference in the mean value can be explained by differences in the position of the foot inside the coil and by the high amount of bones in the foot, which makes the B_1^+ measurement challenging due to the low signal produced by the bone tissues.

Based on the simulated mean values of the B_1^+ in different regions of the lower leg, it will be necessary to apply 273V, 210V and 356V, respectively, on the mid foot, calcaneus and ankle to produce an average of 180° flip angle, using 1ms square-shaped pulse (equivalent to $11.74\mu T$) in these regions of interest.

There are limited publications about development of RF coils for 7T MRI specific for ankle and foot in the literature. Orzada et al. [51] developed an open design transceiver using 8 microstrip elements. Although 20% of deviation in the B_1^+ in a human foot was reported, very limited number

of pixels were acquired rendering the experimental measurements to be less accurate. The highest peak SAR was reported to be 4.73 W/Kg for 10g per 1W input power as opposed to 0.34 W/Kg for 10g per 1W input power with the TTT coil (a ratio of 13.91). The peak B_1^+ in the TTT simulations however was 11.25 μT for 150V input (1ms pulse duration) against 32 μT experimentally measured by Orzada et al [51]. While this shows increase of power by a factor of 8.09 with the TTT design (in order to achieve the same average B_1^+), the peak SAR (which would approach the FDA/IEC limits before the average SAR [66]) is 13.91 times lower, and therefore the SAR efficiency is substantially better with the TTT coil. While Wright et al. [50] developed an innovative Helmholtz pair transmit-only with a 4-channel Rx-only array, no metric (e.g., B_1^+ mean or peak, and/or SAR in the foot model simulations) that can be used to compare directly with this work was reported. Furthermore, the homogenous cylindrical phantoms (relative permittivity of ~78 and a conductivity of ~0.66 S/m) used in [50] are not comparable to the phantom utilized in this work (in the simulations and experiments) as it has a relative permittivity of 39 and a conductivity of 0.49 S/m, representing the average values of the lower leg of the Duke model.

The coil was able to produce high resolution images using the 3D T2-DESS sequence. Further improvements in this work can be done by building an Rx-only insert with a proper decoupling system that can be integrated with the proposed Tx coil (not suitable for optimal receive operation due to its high coupling). The Rx-only insert should not significantly affect the RF performance of the Tx coil [62], and shall improve SNR for performing human imaging experiments. Moreover, RF shimming can potentially be used to improve the B_1^+ homogeneity and reduce SAR. Finally, the position of the foot can be fine-tuned to assure the best coil performance.

In this study, we designed and evaluated a new 4-channel TTT Tx RF coil for foot and ankle imaging at 7T MRI. Excellent agreement is observed between the RF simulations and

experimental measurements in a homogeneous phantom. Homogenous B_1^+ field distribution as well as acceptable peak/global SAR levels were observed in FDTD simulations of an anatomically detailed lower leg human model. In-vivo experiments were performed successfully. Future work will include the construction of an Rx-only array for high SNR and parallel imaging.

3.5 Publications Related to this Chapter

Tales Santini, Junghwan Kim, Sossena Wood, Narayanan Krishnamurthy, Nadim Farhat, Carlos Maciel, Shailesh Raval, Tamer Ibrahim. *"A new RF Transmit Coil for Foot and Ankle Imaging at 7T MRI."* Magnetic Resonance Imaging, 2018.

Tales Santini, Junghwan Kim, Sossena Wood, Narayanan Krishnamurthy, Shailesh Raval, Tamer Ibrahim,. *"A new RF coil for foot and ankle imaging at 7T MRI."* In Proc. of the 25th International Society of Magnetic Resonance in Medicine Annual Meeting, Honolulu, Hawaii, April 2017.

4.0 In-vivo and Numerical Analysis of the Eigenmodes Produced by a Multilevel Tic-Tac-Toe head Transmit Array for 7 Tesla MRI

4.1 Introduction

Ultrahigh-field (UHF) magnetic resonance imaging (MRI) can be exploited for medical research and applications through its higher resolution anatomical imaging, inherent higher contrast, and improved spectroscopy. However, there are technical and physical challenges associated with UHF imaging that have not been completely addressed yet: a) the inhomogeneous distribution of the circularly polarized transmit fields (B_1^+), responsible for excitation [7, 8, 67, 68]; b) the potentially higher power deposition in the tissues [69, 70]; c) the absence of commercial transmit body coil integrated into the system (commonly seen at lower fields); and d) the difficulty to supervise the local specific absorption rate (SAR) [71].

Several designs of radio-frequency (RF) transmit arrays have been proposed to improve the RF (B_1^+ and SAR) performance at UHF MRI [72-75]. A major advantage of these multichannel systems is that the channels of the RF arrays can be manipulated to operate at specific amplitudes and phases, having the potential to optimize a certain characteristic of the RF fields distribution (usually improving B_1^+ homogeneity and/or efficiency and minimizing SAR.) To determine these operational points, some techniques have been applied, among them the eigenmodes approach; for instance, the two-dimension image uniformity of a spherical phantom was 10% by linearly combining four harmonics modes [76]. Moreover, two time-interleaved acquisitions using different modes have shown improvement in the homogeneity without increasing the time of acquisition [77]. Eigenmode approaches have also been utilized to analyze the signal-to-noise ratio

(SNR) behavior of phased array receive coils [78, 79] and to increase the acceleration factor in parallel imaging [80].

In this work, a description and an excitation paradigm are presented for a 20-channel, five-sided Tic-Tac-Toe (TTT) RF transmit array design for 7 Tesla (T) MRI [73]. The RF coil performance (B_1^+ and SAR) was studied using the eigenmodes approach. The modes were numerically calculated from finite-difference time-domain (FDTD) simulations and experimentally verified in-vivo and on a spherical phantom with a 7T human MRI scanner. Using the designed RF array, up to five eigenmodes can be excited simultaneously. The combination of these eigenmodes has the potential to achieve an efficient and homogeneous B_1^+ field distribution with low levels of SAR at UHF MRI.

4.2 Methods

4.2.1 RF coil Design and Construction

The TTT coil design has been applied to several UHF human MRI applications, including head [20, 31, 73, 81], breast [25, 26], torso [33], and foot [35, 82]. Figure 21 (a) shows the schematic diagram of a four-element 2x2 TTT transmit array design. The coil is composed of eight square-shaped transmission lines electrically connected to each other in a tic-tac-toe fashion. The outer strut was built from 8μm-thick single-sided copper sheets (Polyflon, Germany). The inner rods are composed of solid square-shaped copper (McMaster-Carr, USA) partially inserted into the outer strut, creating a squared shape coaxial transmission line. The dimensions of the outer strut are 228.6 × 228.6 × 19.0 mm^3.

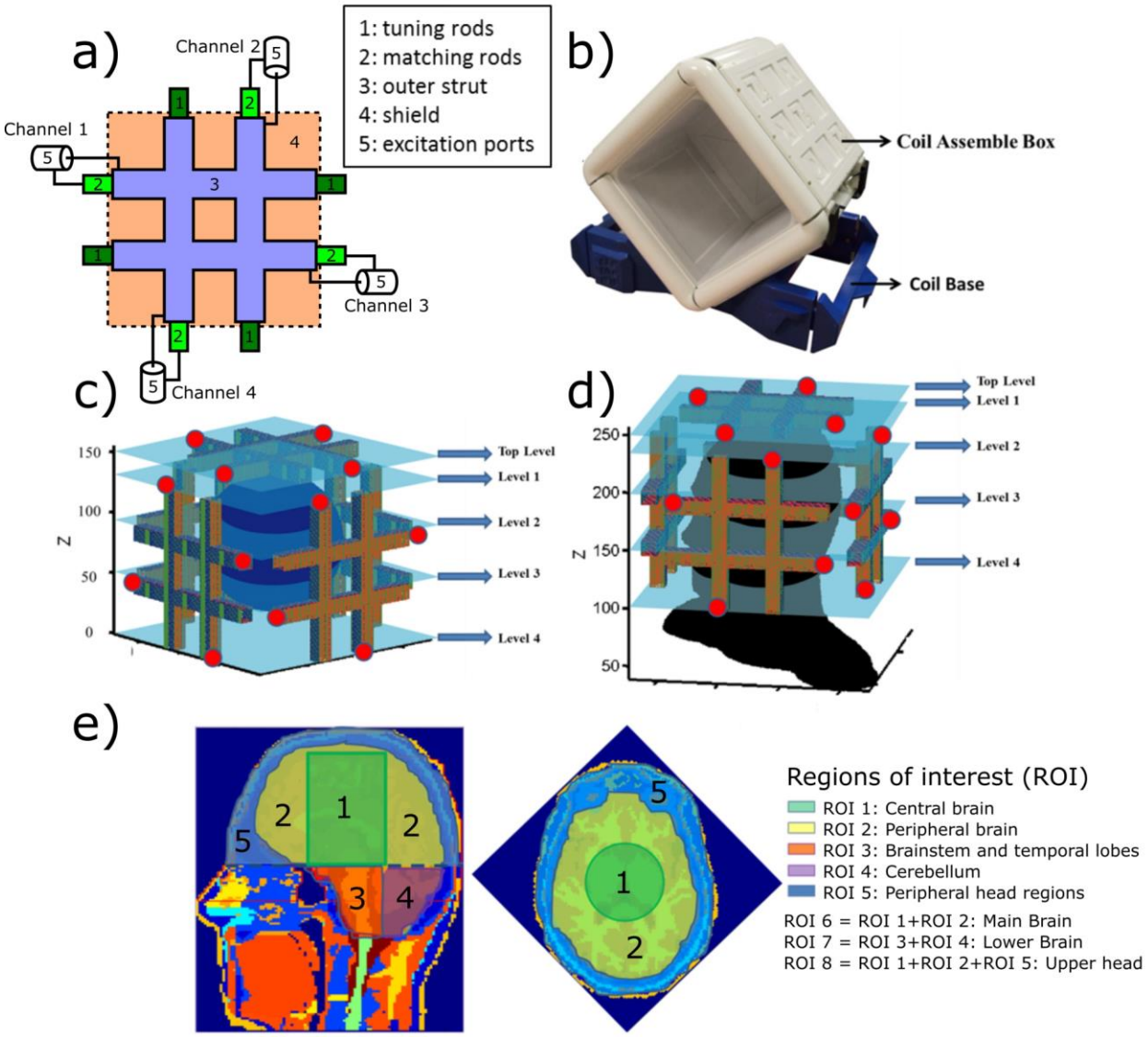

Figure 21: Coil schematic diagram, load position and regions of interest. In (a), the schematic diagram of a four-element, 2x2 Tic-Tac-Toe array design. The copper rods (1 and 2) are partially inside the copper struts (3) providing matching and tuning to the RF coil. In (b), the assembled RF coil system, composed of 5 sets/sides of the 2x2 Tic-Tac-Toe transmit arrays (total of 20 transmit elements.) In (c), FDTD spherical (~17cm in diameter) water phantom model (108 by 108 by 108 Yee cells with isotropic resolution of ~1.6mm). The red dots indicate the excitation points of the three visible sets of the 2x2 Tic-Tac-Toe arrays. The 5 levels of the coil in Z direction are shown. In (d), the Duke Virtual Family Adult Head Model (114 by 117 by 144

Yee cells with isotropic resolution of ~1.6mm). In (e), the head model was divided into 8 different regions of interest (ROI) as indicated by the color code and the numbers.

The excitation ports of one side (four channels) are also shown in Figure 21 (a). Tuning and matching of the coil is performed by changing the length of the inner rods inside the outer struts, presenting similar performance in terms of s-parameters as the demonstrated in [35]. The RF copper shielding is located at the back of the coil struts (with a gap of 15.8mm) and it functions as the ground of a cavity resonator, being responsible for both increasing the RF efficiency and preventing RF leaking. The RF copper shielding is composed of double layer 4μm thick copper sheets (Polyflon, Germany) and it was slotted with specific patterns to reduce eddy currents while the RF performance is maintained, as demonstrated in [83]. The non-metal parts of the array were 3D printed using polycarbonate (Stratasys, USA).

Figure 21 (b) shows the assembled RF coil system which is composed of five sides of the four-element 2x2 Tic-Tac-Toe transmit array (earlier described), resulting in a total of twenty transmit channels/excitation ports. The channels of the RF array were tuned and matched on the bench using the Agilent Network Analyzer Model E5062A (Santa Clara, US). While the five sides of the four-element 2x2 TTT transmit array are inherently decoupled from each other (less than -16dB), on any 2x2 side, the coupling among the adjacent transmit channels (S12 and S14) is about -9 to -11 dB, and the coupling between opposite elements (S13) is about -3 to -4 dB.

4.2.2 Finite-Difference Time-Domain Simulations

An in-house FDTD software package with an accurate transmission-line feed mechanism [84] was implemented to model the RF performance of the 20-channel TTT transmit array. This simulation package has been previously utilized and verified [25, 26, 60, 61, 65, 84-87]. The RF

fields were calculated with the coil loaded with a homogeneous spherical phantom model (diameter=17.1cm, conductivity=0.46 S/m and relative permittivity=79.0) and a human head model ($18.2cm \times 18.7cm \times 23.0cm$), which was extracted from the Virtual Family Duke Model [88]. The resolution of the models is ~1.6mm isotropic per voxel and the simulation was run until a steady state was achieved (100,000 time-steps, time resolution of 3 ps). Figure 21 (c and d) shows respectively the relative position of the homogenous spherical phantom and the human head model inside the RF array. The excitation points are identified by the red dots.

The B_1^+ field distribution was analyzed in eight regions of interest (ROI) described in Figure 21 (e). The ROIs are based on human head anatomical characteristics as well as the electromagnetic characteristics of the coil.

4.2.3 Calculation of the Eigenmodes

The current distributions induced on the RF coil elements can be controlled by manipulating the amplitude and phase of the voltages feeding the excitation ports. A specific current distribution induced on the elements of the RF coil also determines an eigenmode [89]. Consequently, the B_1^+ field distribution and SAR can be manipulated as a result of the superposition of fields produced by the individual elements. In this work, the set of B_1^+ field distributions was arranged by:

$$\boldsymbol{C} = \begin{pmatrix} B_{1(1)}^+ & \cdots & B_{L(1)}^+ \\ \vdots & \ddots & \vdots \\ B_{1(n)}^+ & \cdots & B_{L(n)}^+ \end{pmatrix} \quad \text{4-1}$$

where $\boldsymbol{C}$ is the B_1^+ field matrix generated by an array with L transmit channels, n is the number of Yee cells inside the ROI. $\boldsymbol{C} * \boldsymbol{C}$ gives the correlation among the channels of the array; therefore, the eigenmodes can be calculated by:

$$(\boldsymbol{C} * \boldsymbol{C})\boldsymbol{v} = \boldsymbol{\lambda v} \qquad 4\text{-}2$$

where $\boldsymbol{v}$ is a unitary matrix of eigenvectors; $\lambda = \begin{pmatrix} \lambda_1 & \dots & 0 \\ \vdots & \ddots & \vdots \\ 0 & \dots & \lambda_L \end{pmatrix}$ is a diagonal matrix of eigenvalues. With solutions for Equation 4-2, $\boldsymbol{Cv}$ is the spatially pseudo-independent fields or eigenmodes of the transmit coil; $\boldsymbol{v}$ gives the phase and amplitude of each coil channel; λ_i represents the field energy for eigenmode i.

The transmit array was grouped into five levels of four elements along the static magnetic field (Z) direction: Top_Level, Level_1, Level_2, Level_3, and Level_4 (see Figure 21 (c and d)). The eigenmodes were calculated in each Z level of the transmit array by applying Equation 4-2 on the simulated B_1^+ field distributions; thus totaling four different excitation field patterns per level and 20 in total. Since the magnetic field distribution and SAR are two major concerns for 7T imaging, the attributes of the modes and coil Z levels were evaluated using three criteria:

1) average B_1^+ intensities inside each ROI for each Z level and mode, scaled for 1W input power per channel (totaling 4W for one Z level);

2) B_1^+ homogeneity calculated by the coefficient of variation (CV) inside each ROI for each Z level and mode;

3) average and peak SAR over the whole head volume (from the top of the neck) for each Z level and mode, scaled for 1W input power per channel (totaling 4 W for one Z level).

Please note that IEC/FDA limits the SAR in 3.2 W/kg for 10g of tissue inside the human head [66]. SAR levels were therefore evaluated in terms of average SAR over the whole head volume, peak SAR over any 10g of tissues, and safety excitation efficiency (SEE) [90], defined as average B_1^+ intensity over the combined volume of all eight ROIs divided by the average SAR over the whole head volume [$\mu T\sqrt{kg}/\sqrt{W}$].

The eigenmodes were combined using an optimization of the 20-channel B_1^+ fields. The optimization aims at minimizing the CV of the B_1^+ field distribution within the ROI that encapsulates the whole head above and including the cerebellum and excluding the nasal cavities. The resultant field distribution was then scaled by 1W of total input power and the SEE was calculated based on the average B_1^+ field in the ROI divided by the square root of the average SAR for the whole head.

4.2.4 MRI Experiments

The FDTD calculated eigenmodes were experimentally verified using the constructed 20-channel transmit array. The MR experiments were conducted using a 7 Tesla MRI scanner (Siemens MAGNETOM, Germany). This study was approved by the University of Pittsburgh's Institutional Review Board (IRB PRO17030036). One healthy volunteer was scanned after signing a written informed consent. The phantom MRI imaging experiment and the in-vivo study were conducted by acquiring relative B_1^+ maps using Turbo Flash MRI sequence; the outputs of this MRI sequence are: 1) the B_1^+ distribution for each transmit channel (scaled to the square root of

the sum of the square of all connected transmitting channels); and 2) the relative phases. The sequence parameters used were: TE/TR=2.34/160ms, resolution 3.2mm isotropic, flip angle 12 degrees. The scanner is equipped with 8 channels in the parallel transmit (pTx) mode with 1kW power amplifier per channel (8kW in total). These 8 transmit-channels were connected to the RF array in 2 Z Levels (each level has 4 channels) in each B_1^+ mapping experiment. Level_1 (most homogeneous level) was always connected in addition to another level (Figure 21d) per one B_1^+ mapping measurement. The 4 transmit-channels not connected to Level_1 were manually changed to another level until all the B_1^+ maps were acquired for all (5) Z levels. A transmit/receive (T/R) switch box was used to receive the signal from all 20 channels for any B_1^+ mapping acquisition. The transmit channels of the coil that were not used in a specific B_1^+ mapping acquisition were terminated with 50Ω loads through the T/R box.

4.3 Results

4.3.1 Eigenmodes

By applying Equation 2-3 on the FDTD-simulated B_1^+ fields, the phases and amplitudes of the eigenmodes were obtained for each Z level of the transmit array; the results are presented in Table 1. Four modes were identified, and these modes presented uniformly distributed relative phase shifts and constant amplitudes among the 4 channels of each Z level: Mode_1 (named as quadrature) presents phase increments of ~90°; Mode_2 (opposite-phase) has increments of ~180°; Mode_3 (anti-quadrature) presents increments of ~270°; and Mode_4 (zero-phase) has increments of ~0° or ~360°. There were minor phase (<8°) and amplitude (<8%) deviations among the 5

different Z levels, which is impacted by the position of the load inside the RF coil. For practical purposes, the phases were kept as multiples of 90° and the amplitudes were considered to be the same for all channels.

Table 2: FDTD-Calculated Relative Phases and Amplitudes Associated with the Eigenmodes of the Array's Five Z levels. The coil was Loaded with a Homogeneous Spherical Phantom.

		Mode1 (Quadrature)	Mode2 (Opposite-phase)	Mode3 (Anti-quadrature)	Mode4 (Zero-phase)
Top Level	Phases	(0°, 90.7°, 179.4°, 268.6°)	(0°, 181.1°, 0.3°, 179.3°)	(0°, 270.1°, 180.3°, 90.2°)	(0°, -0.1°, -0.6°, 0.5°)
	Amplitudes	(0.50, 0.50, 0.50, 0.50)	(0.49, 0.50, 0.51, 0.50)	(0.50, 0.50, 0.50, 0.50)	(0.50, 0.50, 0.50, 0.50)
Level1	Phases	(0°, 87.7°, 173.5°, 265.5°)	(0°, 179.4°, -0.5°, 180.1°)	(0°, 267.1°, 178.8°, 89.7°)	(0°, -2.3°, -7.3°, -4.7°)
	Amplitudes	(0.49, 0.53, 0.51, 0.47)	(0.50, 0.50, 0.50, 0.50)	(0.50, 0.50, 0.50, 0.50)	(0.51, 0.47, 0.49, 0.53)
Level2	Phases	(0°, 91.2°, 178.8°, 266.9°)	(0°, 181.1°, 5.4°, 184.1°)	(0°, 270.1°, 182.1°, 92.0°)	(0°, 0.8°, -4.5°, -4.6°)
	Amplitudes	(0.47, 0.54, 0.53, 0.46)	(0.50, 0.49, 0.50, 0.51)	(0.51, 0.50, 0.49, 0.50)	(0.52, 0.47, 0.48, 0.52)
Level3	Phases	(0°, 91.6°, 180.0°, 268.3°)	(0°, 180.5°, 1.3°, 180.7°)	(0°, 270.1°, 180.0°, 89.9°)	(0°, 1.3°, -1.2°, -2.4°)
	Amplitudes	(0.48, 0.51, 0.52, 0.49)	(0.50, 0.49, 0.50, 0.51)	(0.50, 0.50, 0.50, 0.50)	(0.51, 0.49, 0.49, 0.51)
Level4	Phases	(0°, 89.8°, 179.5°, 89.7°)	(0°, 179.8°, -0.4°, 179.8°)	(0°, 269.8°, 179.5°, 89.7°)	(0°, -0.2°, -0.8°, -0.5°)
	Amplitude	(0.50, 0.50, 0.50, 0.50)	(0.50, 0.50, 0.50, 0.50)	(0.50, 0.50, 0.50, 0.50)	(0.50, 0.50, 0.50, 0.50)

4.3.2 B_1^+ Field and SAR Comparison of the Eigenmodes

The FDTD-calculated B_1^+ field distribution of all modes for all the Z levels are presented in Figure 22 (a). When comparing the eigenmodes in different Z Levels, the following observations are noted:

a) Mode_1 (quadrature) generally provides high B_1^+ intensity in the central regions of the head/brain with the bright spot generally moving along the Z direction for distinctive Z levels;

b) Mode_2 (opposite-phase) generates peripheral brain excitation;

c) Mode_3 (anti-quadrature) generally excites the periphery of the head;

d) Mode_4 (zero-phase) excites the lower brain (cerebellum and temporal lobes).

The B_1^+ field phase distribution maps are shown in Figure 22 (b) (note that $-2\pi = 2\pi$, i.e., the intense blue color is equal to the intense red color in the colorbar).

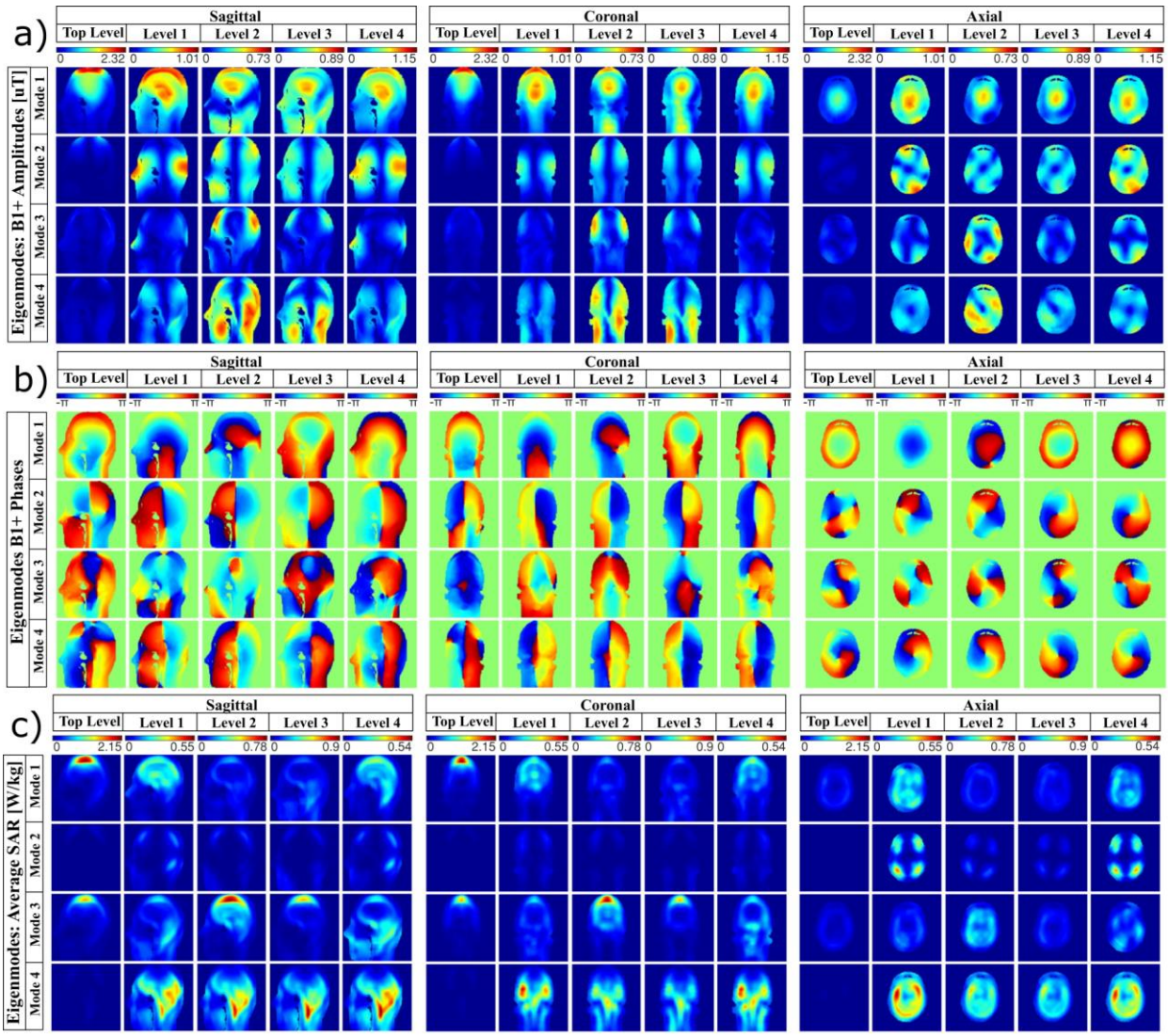

Figure 22: Simulated B_1^+ field and SAR distributions of the Eigenmodes in the Duke head model for each level (shown in Figure 21.) The central slices in sagittal, coronal, and axial planes are shown. In (a), the amplitude of B_1^+ field distributions, in μT for 1W input power per channel (total 4W as each level contains 4 channels). For the four Eigenmodes per level, the colorbar is scaled from 0 to the maximum. In (b), the phase of the B_1^+ field distribution in radians. In (c), the SAR distributions in W/kg for 10g of tissues per 1W input power per channel (total 4W). The coil was loaded with the Duke Virtual Family Adult Head Model

The values of B_1^+ field intensities for all modes, levels, and ROIs are presented in Figure 23, from which we can note that:

Top_level produces an efficient excitation in the upper head (ROIs 1, 2, 5, 6, and 8) when operating in Mode_1, presenting an average B_1^+ intensity of 0.73μT for 1W input power per channel (total 4 W) in these ROIs.;

Level_1 and Level_4 are also efficient operating in Mode_1, producing an average B_1^+ of 0.54μT in the ROIs 1, 2, 3, 5, 6, and 8;

Levels 2 and 3 produces an efficient excitation in the lower brain (ROIs 3, 4, and 7) when operating in Mode_4, presenting an average B_1^+ of 0.48μT in these regions.

The CV of the B_1^+ field intensities over the specified eight ROIs for different modes and levels are shown in Figure 24.

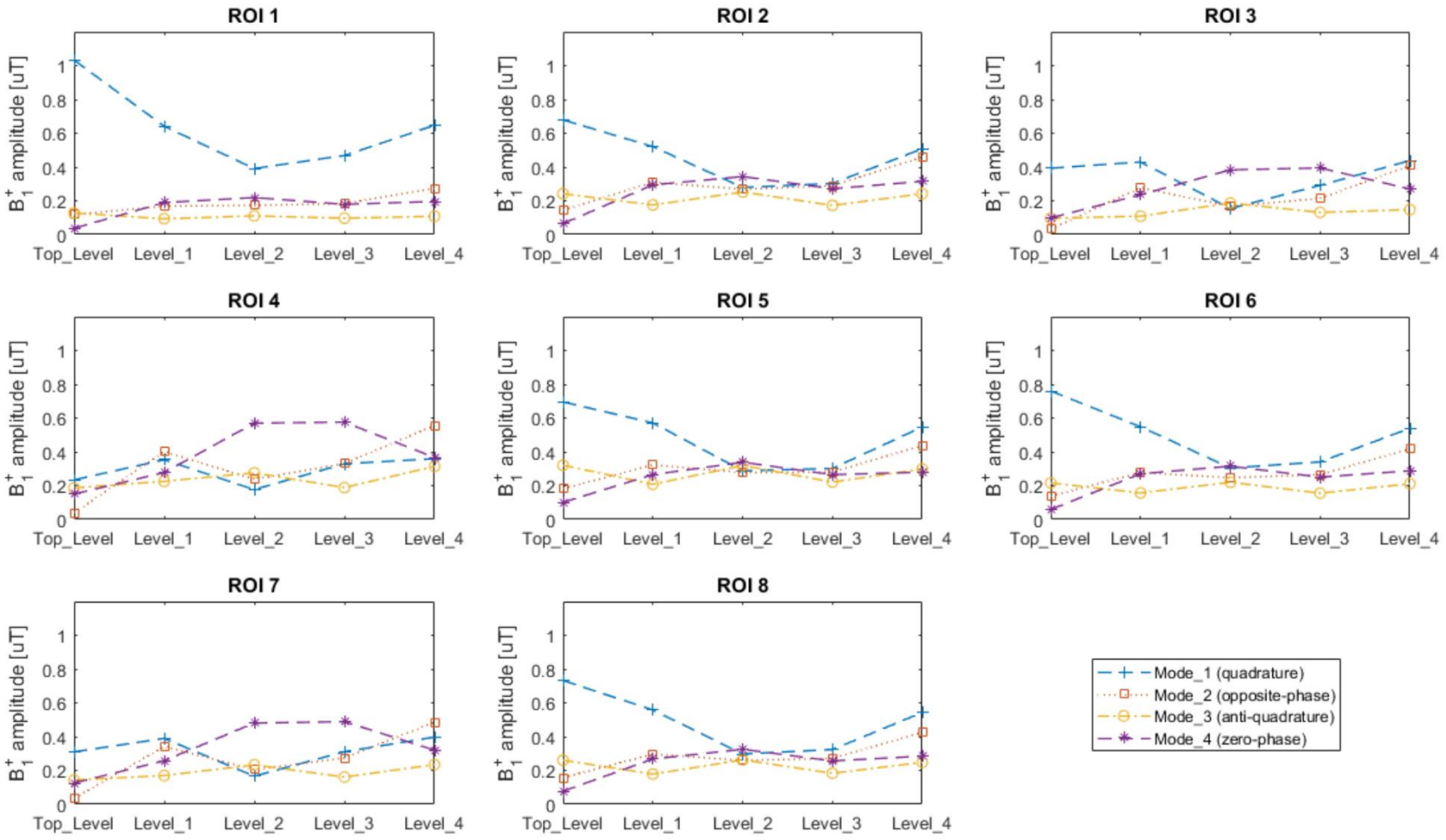

Figure 23: Average B_1^+ intensities calculated inside the 8 different regions of interest (ROIs) shown in Figure 21 (e) for each Z level of the RF array shown in Figure 21 (d). The scale is in μT for 1W input power per channel (total 4W).

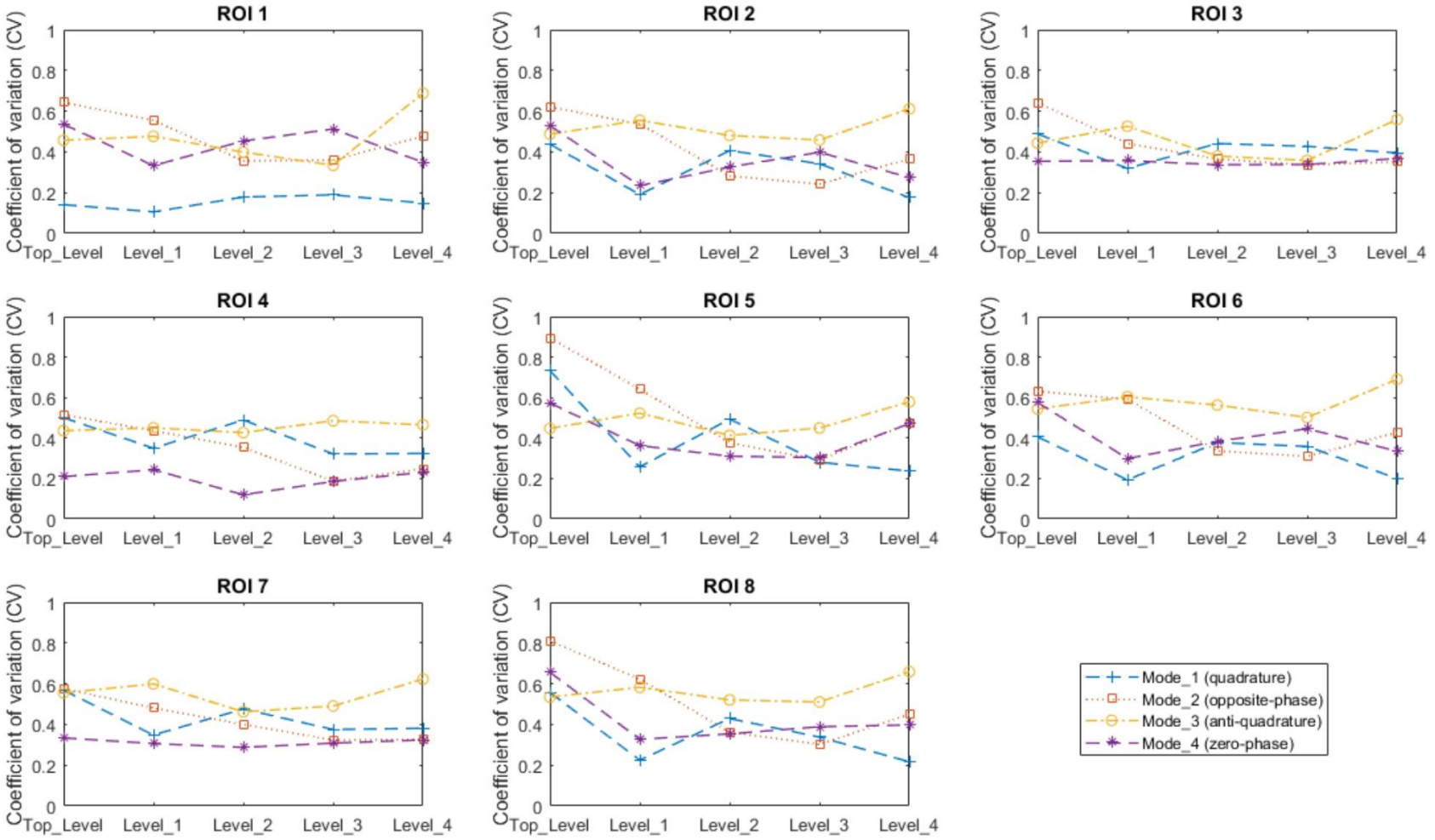

Figure 24: Coefficient of variation (standard deviation over the mean of B_1^+ field distribution) calculated inside the 8 different regions of interest (ROIs) shown in Figure 21 (e) for each Z level of the RF array shown in Figure 21 (d).

The numerically calculated SAR distributions for all eigenmodes from all Z levels are shown in Figure 22(c). Preferable modes present higher average B_1^+ intensity and lower peak and average SAR. The following observations are noted:

a) the SAR distribution significantly varies for different eigenmodes and Z levels;

b) the highest SAR regions usually correspond to lower intensities of B_1^+;

c) Top_level operating in Mode_1 produces the highest peak SAR, but it is also B_1^+ efficient;

d) Levels 1 and 4 produce homogeneous SAR distribution when operating in Mode_1;

e) Mode_4 produces higher levels of SAR in the lower brain regions (except Top_level);

f) Mode_1 usually produces low levels of average and peak SAR (except in Top_level) and high levels of SEE.

Figure 25 shows the average/peak SAR and SEE values for all Z levels and eigenmodes of the transmit array.

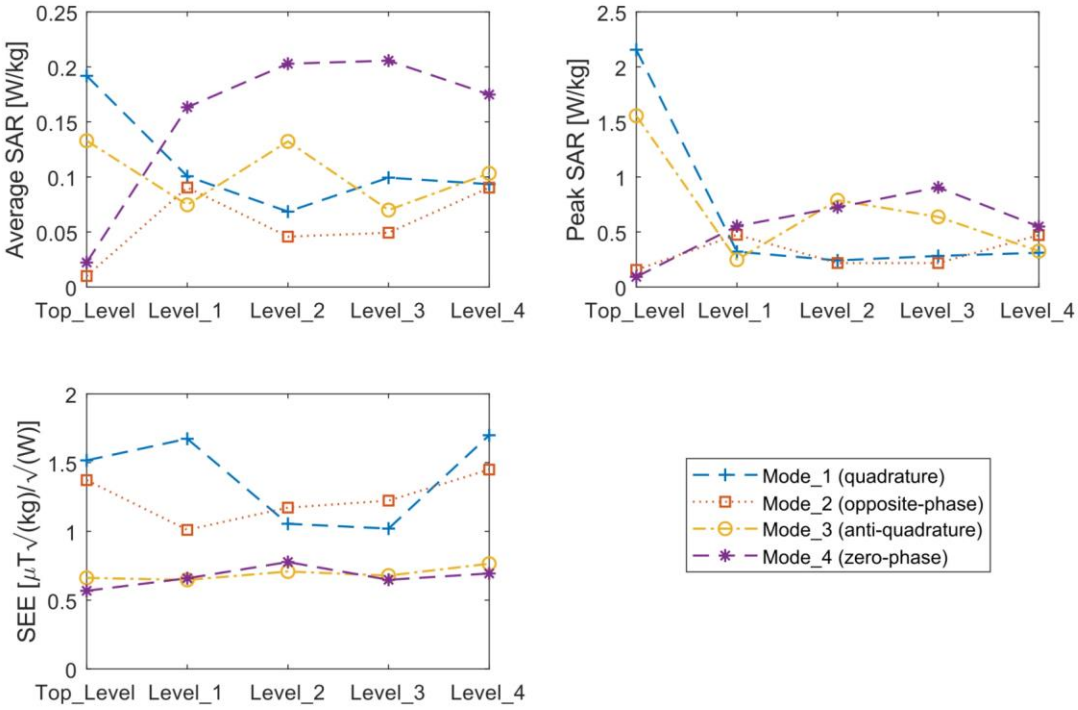

Figure 25: SAR evaluation of the Eigenmodes for each Z level of the RF array shown in Figure 21(d). In a) the average SAR per 1 W input power per channel (total 4 W). In b) the peak SAR per 1 W input power per channel (total 4 W). In c), the safety excitation efficiency (SEE) (the B_1^+ field is averaged over a volume that encapsulates all eight regions of interest.) The results are presented for the Duke Virtual Family Adult Head Model.

4.3.3 Experimental Verification

Figure 26 shows the simulated and measured B_1^+ maps for the four eigenmodes excited by each of the five Z levels of the 20-channel transmit array. Figs 6(a) and 6(c) show, respectively, the simulated and measured data in the homogeneous spherical phantom. Figure 26 (b) shows the simulated B_1^+ maps in the Duke head model. For a visualization resembling the in-vivo acquired

data, a limited number of tissues are shown: tissues distant from the brain (e.g., tongue muscle) or tissues which produce low MR signal (e.g., bone) was removed from the Figure 26 (b), although the simulations were conducted using the complete Duke head model. Figure 26 (d) shows the in-vivo acquired eigenmodes. The results show excellent agreement between the simulated and measured data.

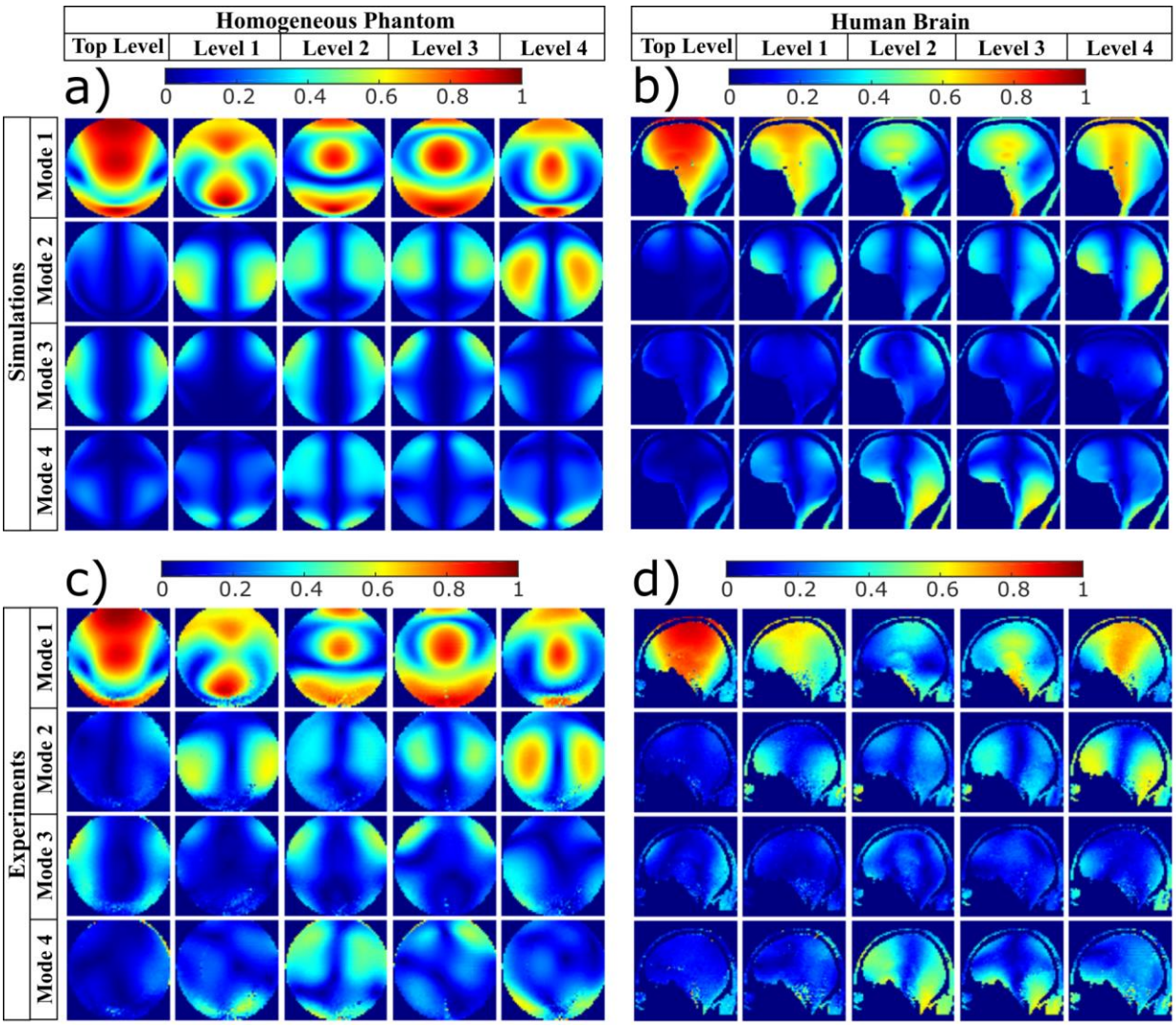

Figure 26: Experimental verification and simulated B_1^+ field distributions of the Eigenmodes for the homogenous spherical phantom and the human head, showing the central sagittal view. In (a), the simulated B_1^+ field distributions in the homogeneous spherical phantom with relative permittivity of 79 and conductivity 0.41 S/m. In (b), the simulations in the Duke Virtual Family Adult Head Model. In (c), B_1^+ maps acquired in the homogeneous phantom with relative permittivity of 79 and conductivity 0.41 S/m. In (d), in-vivo human B1 maps. All maps are scaled to the square root of the sum of the square of all connected transmitting channels.

4.3.4 Combination of the Eigenmodes

Figure 27 shows the combination of the modes by minimizing the CV of the B_1^+ fields in the ROI. The values in the ROI (composed by the whole head above and including the cerebellum and excluding the nasal cavities) are: $CV_{B_1^+}$ = 16.6%, $Max_{B_1^+}/Min_{B_1^+}$ = 3.51, SEE = 1.48 $\mu T/\sqrt{W/kg}$ (defined as mean B_1^+ in the ROI divided by the square root of the SAR for the whole head), mean B_1^+ = 0.23μT for 1W total input power.

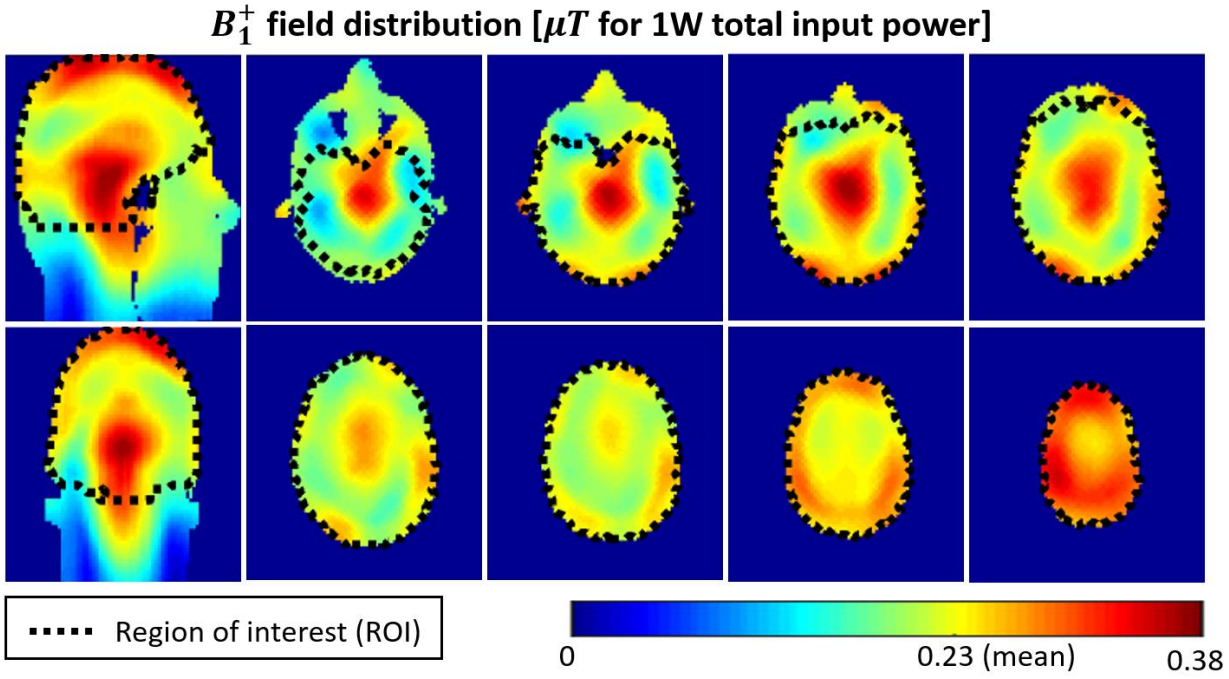

Figure 27: An example of the combination of the modes of the Tic-Tac-Toe coil (20 Tx channels). The ROI represents the entire head above and including the cerebellum and excluding the nasal cavities.

4.4 Discussion and Conclusion

In UHF MRI, as the wavelength of the electromagnetic waves inside the tissues gets closer, in size, to the body parts being scanned, inhomogeneities become a major issue, as it can affect the image quality, creating voids and low contrast regions (especially in high flip-angle sequences). In the case of brain imaging, this situation is usually accentuated in the lower brain regions such as cerebellum and temporal lobes [16]. There are several works suggesting the use of two modes to increase the homogeneity of the B_1^+ field distribution [77, 91, 92]. Another work suggested that the coefficient of variation of a 2D image can reach 10% by using four eigenmodes in a homogeneous spherical phantom using a birdcage RF coil [76]. At many instances, the application of these methods can come at a significant elevation of time of acquisition, elevated SAR, and difficulties in simultaneously exciting several distinct modes of a coil [89, 93, 94].

The freedom to manipulate the current distribution of different coil elements potentially contributes to the generation of a homogeneous B_1^+ fields distribution [95-97]. However, coil arrays typically show the capability to control current distributions only at XY plane, while current distribution are not very commonly controlled in the Z direction. It is worth noting that there are some coil designs that can potentially generate current control along the Z direction. Some examples are: the multi-rows/rings transmit arrays that allow parallel transmission approaches [98-100]; the rotating RF coil approach [101, 102]; and the spiral volume coil [103].

In this work, the eigenmodes of a 20-channel Tic-Tac-Toe RF array were studied. The RF array is composed of five excitation levels located at different positions along the static magnetic field. For each level (composed of four ports located in the same XY plane), there are four distinctive modes (with 90° phase-shift multiples) that can be generated, calculated using Equation 3-2. Using power splitters and phase shifters (1-to-N network), up to 5 different modes can be

excited simultaneously in a single image acquisition (since each Z level can present a different excitation mode), potentially improving B_1^+ homogeneity and reducing SAR levels. Thus, 1024 possible combinations can be implemented using the five Z levels of the RF array, if the amplitudes of the channels are fixed.

It is important to analyze the field distribution of the eigenmodes provided by an RF head array so that a target homogeneous/low SAR excitation can be achieved. In terms of B_1^+ distribution inside the human head, our results show that: Mode_1 (quadrature) is the most efficient, producing center brightness at different Z levels. However, voids are observed in some regions in the lower brain (such as the cerebellum and temporal lobe regions). Mode_2 (Opposite-phase) produces low signal in the center and excites mostly the periphery regions of the brain. Mode_3 excites regions in the head periphery (mostly skin and skull) and can have localized functions such as fat suppression (extracerebral lipids from skins and skull can be suppressed to reduce the influence from this region and leave the central brain regions unaffected). Mode_4 excites mostly the lower brain regions (cerebellum and temporal lobes). The analysis also shows that Mode_1 of Level_1 and Level_4 can excite relatively uniform B_1^+ distributions, with CV = 22% and 22% inside ROI8 (upper head) for Level_1 and Level_4 respectively.

While there can be many solutions for the RF excitation that achieve a satisfactory signal fidelity to the targeted excitation pattern (e.g., homogeneous B_1^+ field), minimizing the local SAR is also an important target for the coil design and operation. In this work, the average and peak SAR was compared for different Z levels and eigenmodes. It is important to note that the SAR distribution presented in this work is an outcome of the phases and amplitudes determined by the eigenmodes, which were calculated using only the B_1^+ fields. Therefore, lower levels of SAR can be achieved if SAR constraints are included. Mode_1 produces lower average (< 0.11 W/kg) and

peak SAR (except Top_Level), combined with efficient B_1^+ in the upper head, leading to a high SEE (>1.5$\mu T\sqrt{kg}/\sqrt{W}$) as seen in the Levels 1, 2 and 4. This is higher than the double row loop array (0.76 $\mu T\sqrt{kg}/\sqrt{W}$ [90, 104]) and the birdcage coil (0.89 $\mu T\sqrt{kg}/\sqrt{W}$ [105]) for instance. While Top_level produces a high peak SAR, it is B_1^+ efficient, resulting in SEE of ~1.5. Mode_2 (opposite-phase) produces a relatively high SEE for Levels 2 and 3, with relatively high brain peripheral excitation. Although Mode_4 (zero-phase) presents low levels of SEE, it has efficient B_1^+ in the low brain regions which are challenging at UHF MRI.

The simulations were experimentally verified by acquiring the individual channels B_1^+ maps in the homogeneous spherical phantom and in-vivo in human subjects. The field distributions of the eigenmodes were then calculated and compared with the simulated fields (Figure 26). The modes are highly consistent between simulations and experiments. Small differences may be due to differences in the head/phantom position in simulations and experiments, differences in the tuning of the RF coil elements, differences in the hardware of the transmitting channels, and differences in the human head model and the subject scanned. Discrepancies in the B_1^+ maps between the phantom and the head can be mostly attributed to dielectric effects – that commonly occur in homogeneous water phantoms [106] – and to the anatomical differences between the two models.

An example of the combination (RF shimming) of the modes demonstrates a high level of the homogeneity and coverage of the B_1^+ field over the ROI, as demonstrated by the values of $CV_{B_1^+}$ = 16.6%, and $Max_{B_1^+}/Min_{B_1^+}$ = 3.51. The low level of SAR is also demonstrated with a high level of SEE (1.48 $\mu T/\sqrt{W/kg}$) even though SAR constraints were not included as a part of the RF shimming. The strong coupling between opposite channels (-3 to -4dB) can improve the load insensitivity of the array (being able to scan subjects with different head volumes/shapes and

achieve similar RF characteristics), with the cost of lower transmit efficiency. Nevertheless, an example of the combination of the modes (Figure 27) shows that the transmit RF array produces enough B_1^+ intensity to perform inversion with a 1ms square RF pulse using 8kW power amplifier capability with ~35% loss to the coil port.

The eigenmode arrangement of the TTT 20-channel RF array potentially allows controlling RF excitation not only at XY plane but also along the Z direction. As five eigenmodes from different Z levels can be excited simultaneously (one per excitation level in Z), we believe that the combination of these modes can provide a full brain homogeneous B_1^+ excitation. Future work will include the combination/superposition [70, 107-110] of these eigenmodes in order to obtain a homogeneous and efficient B_1^+ field distribution with low levels of SAR.

4.5 Publications Related to this Chapter

Tales Santini, Yujuan Zhao, Sossena Wood, Narayanan Krishnamurthy, Junghwan Kim, Nadim Farhat, Tiago Martins, Tiejun Zhao, Howard Aizenstein, and Tamer S. Ibrahim. *"In-vivo and numerical analysis of the eigenmodes produced by a multi-level head transmit array for 7 Tesla MRI*" PlosOne, 2018.

Tales Santini, Yujuan Zhao, Sossena Wood, Junghwan Kim, Nadim Farhat, Narayanan Krishnamurthy, Tiejun Zhao, Tamer S. Ibrahim. *"Experimental and Numerical Evaluations of Simultaneously Excited Eigenmodes in a 20-channel Transmit RF Array for 7 Tesla human MRI".* In Proc. of the 26th International Society of Magnetic Resonance in Medicine Annual Meeting, Paris, France, 2018.

5.0 RF Developments for Achieving Homogeneous Transmit Field and Reduced SAR for 7 Tesla Neuro MRI

5.1 Introduction

It is well accepted that Ultra-high field (UHF, ≥7T) MR systems have the potential to improve the signal-to-noise ratio (SNR), enhance image contrast, and increase magnetic susceptibility and chemical shift when compared with lower field strengths [47, 111-113]. These characteristics can be potentially translated into increased image resolution, shortened scan times (with the use of higher acceleration factors), and/or improved contrast in functional studies. However, the spatial inhomogeneities in the radiofrequency (RF) fields caused by the shorter wavelengths and reduced skin depths can cause voids or regions of low contrast in the images, limiting its diagnosis capabilities. The higher operational frequencies and RF inhomogeneities can also lead to higher average and local specific absorption rate (SAR), which can cause temperature rise and potential tissue damage [114].

The methods developed for improving RF excitation homogeneity can be divided into two main categories. First, multiple pulse sequences and acquisition strategies have been developed to increase the insensitivity of the images to the circularly polarized component of the RF magnetic field responsible for excitation (B_1^+ field) inhomogeneities. These include adiabatic pulses [115, 116], transmit SENSE [117, 118], spoke pulses [119], and the acquisition of two interleaved modes with TIAMO [92, 120]. The second strategy – and the focus of this work – is related to RF coil design and methodology of operation. This strategy includes the development of multichannel transmit (Tx) RF array systems aiming at producing homogeneous B_1^+ field in conjunction with

lower SAR distribution with the superposition of the fields generated by the coil elements [121]. In multi-channel Tx arrays, the phase and amplitude of the RF field produced by each transmit channel can be manipulated towards a specific objective(s), usually aiming at increasing the global and/or local B_1^+ field homogeneity/intensity and reducing SAR. This technique is known as static RF shimming. Several research groups have also explored the pulse shape of each Tx channel independently in a technique called transmit SENSE [117, 118]. However, it requires complex hardware settings and cannot be implemented in the single transmit (sTx) mode: the only operational mode for UHF MRI cleared by the Food and Drug Administration [26].

Previous work evaluated the Tic-Tac-Toe (TTT) RF head array for 7T MRI. In [121], it was demonstrated that an 16-channel TTT multilevel coil can simultaneously drive up to 4 eigenmodes from 4 different levels of the coil, being different eigenmodes/levels exciting different regions on the brain; the optimal combination of these eigenmodes requires numerical optimizations. The reference [34] compared the TTT design with the transverse electromagnetic (TEM) resonator, demonstrating an improved transmit field homogeneity and load insensitiveness of the TTT design.

In this work, we described the implementation of the TTT RF system aiming for imaging studies. Firstly, constrained numerical optimizations of the 16-channel head TTT transmit array was performed based on Finite-difference time-domain (FDTD) simulations and taking into account the power losses in the hardware. Two homogeneous (in terms of B_1^+ field) RF shim cases for two different power and SAR efficiency levels were experimentally implemented on the single channel (sTx) mode of a MAGNETOM 7T system using power splitters and phase shifters (coaxial cables). In-vivo B_1^+ maps, as well as T2 SPACE and FLAIR sequences were acquired and analyzed for demonstration purposes. The results demonstrated homogeneous 7T imaging using the

described RF system, which has been utilized in more than 750 diseases-based 7T neuro scans in nine patient studies funded by the National Institutes of Health (EUA).

5.2 Methods

5.2.1 Finite-Difference Time-Domain Simulations and 16-channel Tic-Tac-Toe RF Array Design

The B_1^+ and electrical fields were simulated using an in-house developed full-wave FDTD software with an accurate transmission line algorithm for modeling the excitation and the coupling. This software has been utilized and verified in several publications [17, 25, 26, 28, 35, 68, 122-124]. The spatial resolution utilized for the coil/load was 1.59 mm isotropic, and the temporal resolution was ~3ps. The coil geometry (Figure 28a) was created using MATLAB (MathWorks, USA), totaling 257x257x276 or ~18 million Yee cells. Perfect matching layers were implemented to absorb the irradiating fields, being 8 layers added on the top of the model (towards the Z direction), 12 on the sides, and 32 on the bottom [125]. Each port/channel was excited individually with a differentiated Gaussian pulse, while all the other ports were terminated with a 50Ω load using the transmission line numerical model. The Virtual Family Duke model was used as the load, with its resolution reduced to 1.59 mm isotropic. The model includes the whole head, neck and the top of the shoulders, totaling 23 different tissues. To speed up the RF shimming numerical optimizations (described in the next sections), the resolution of the FDTD calculated B_1^+ fields was reduced by a factor of 2, while the resolution of the electric fields was not changed.

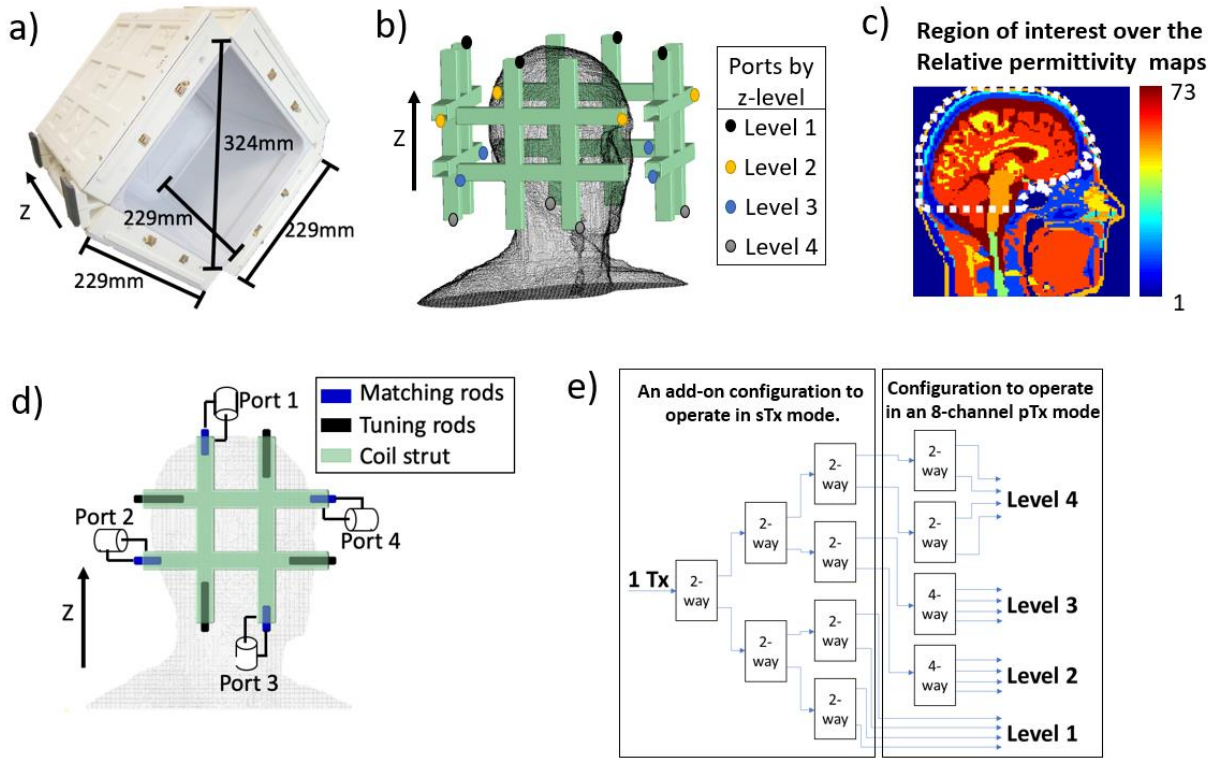

Figure 28: The 16-channel Tic-Tac-Toe (TTT) RF array FDTD model and experimental implementation. In a) the assembled 16-channel TTT array and its dimensions; In b), the location of the 16 channels of the transmit array; In c), the region of interest (white dashed line) plotted over the relative permittivity map of the Duke model at ~297.2 MHz (7T proton frequency). In d), the ports, matching rods, and tuning rods of a representative side of the array. In e), the configuration exclusively using 2-way and 4-way Wilkinson power splitters to drive the 16-channel transmit array in the single channel transmit (sTx) and parallel channel transmit (pTx) modes. The Tx channels of the excitation Z-levels 1, 2, 3, and 4 (shown in b)) experience normalized voltage amplitudes equal to 1, 0.5, 0.5, and 1/√2, respectively.

The Tx coil is based on the TTT design, previously described for foot/ankle [35], breast [25, 26], and head [20, 34, 121] imaging at 7T. Briefly, one TTT side is composed of 8 square-shape transmission lines elements connected to each other in a Tic-Tac-Toe fashion. Four of these elements are connected to excitation ports, and the other four elements are used for frequency

tuning. The coil is matched and tuned by varying the length of the copper rods inside the outer struts in these elements (Figure 28d and Figure 28e). The RF Tx array is composed of four TTT sides positioned around the head, resulting in a 16-channel transmit array (Figure 28c and Figure 28f). The RF shield is composed of double sided 4μm-thick copper sheets (Polyflon, Germany). Cuts were added on each side for reducing the eddy currents, as described in Zhao et al [28]. For optimal imaging purposes, the RF coil system also includes an in-house developed 32-channel receive (Rx)-only insert [73] (its design and implementation are outside the scope of this work).

5.2.2 B_1^+-shimming (without SAR Constraints) Computational Strategy

Numerical optimizations were used to manipulate the phases of the RF fields generated by the channels of the Tx array aiming to minimize the cost function. The coefficient of variation of the B_1^+ field ($CV_{B_1^+}$) is commonly used as the cost function when the goal is to increase B_1^+ homogeneity, but it may produce local regions of high or low flip angles, even if the $CV_{B_1^+}$ is in its global minimum [126]. Therefore, three cost functions were utilized in this work: 1) $CV_{B_1^+}$, in the region of interest (ROI); 2) $CV_{B_1^+}/min_{B_1^+}$, defined as the coefficient of variation over the minimum B_1^+ inside the ROI; and 3) $max_{B_1^+}/min_{B_1^+}$, defined as the maximum B_1^+ over the minimum B_1^+ in the ROI. The $CV_{B_1^+}$ is continuous and inherently smooth over the multi-dimensional space [127], therefore the superposition of B_1^+ among all channels presents small changes with small perturbations in the phases of the RF fields. Hence, there is a reduced number of local minima produced by this function, which improves the convergence rate for gradient descending algorithms. For this reason, we firstly conducted optimizations using the $CV_{B_1^+}$ as the cost function and using random phases as the initial conditions (the amplitude values were fixed, following the

strategy defined in the "RF excitation" subsection). The results of these optimizations were used as the initial conditions for the optimization using $CV_{B_1^+}/min_{B_1^+}$ and $max_{B_1^+}/min_{B_1^+}$ cost functions. The ROI used includes the whole head and the cerebellum and excludes the nasal cavities and ears. The lower ~1 cm of the cerebellum volume is excluded as it contains a minimal number of pixels with brain tissues in the Duke model. The contour of the ROI mask applied over the permittivity map is shown in Figure 28g.

The cost functions were minimized using the MATLAB function $fmincon$, including GPU acceleration for the objective and cost functions calculation. The algorithm used for the $CV_{B_1^+}$ optimizations were the Active-set, due to its capability in searching for an operational point with great efficiency and high convergence rate from random initial conditions [128] . For the $CV_{B_1^+}/min_{B_1^+}$ and $max_{B_1^+}/min_{B_1^+}$ optimizations, the Interior-point algorithm was used in combination with the initial phase conditions attained from the $CV_{B_1^+}$ optimizations, since the algorithm performs Newton steps around the initial conditions without the use of large steps which may dramatically affect the results.

In most RF Tx array/coil designs which utilize RF shimming optimizations, the $CV_{B_1^+}$ and B_1^+ efficiency are strongly related, since a highly homogeneous B_1^+ can be achieved with the expense of lower efficiency [129]. Consequently, a high input voltage would have to be used to achieve the desired flip angle, potentially reaching or exceeding the SAR limits and hardware capabilities. To guarantee an adequate efficiency for the Tx array, the optimizations in this work were performed constraining the mean B_1^+ field to $\geq 0.27\,\mu T/\sqrt{W}$ in the sTx mode. This guarantees enough B_1^+ intensity to produce 180 degrees flip angle with 1ms square pulses, 8kW power amplifiers, and considering the losses between the power amplifiers and the RF coil plug as well as the coil parts, cables, and power splitters.

The RF coil system was designed to work in either the sTx or parallel-transmit (pTx) modes with the use of Wilkinson power splitters (Figure 28b). Based on the eigenmodes of the Tx coil design [121], the 16-channel Tx array is composed of 4 excitation levels in Z direction; each level is composed of 4 Tx channels. Level 1 was chosen to be excited with the maximum RF power for this splitter configuration (half of the total supplied RF power) because of the higher power efficiency associated with this level and its capacity to produce center bright, as previously demonstrated in [121]. Levels 2 and 3 play an essential role in exciting the lower brain regions, including the hippocampus and the temporal lobes [121]. One-eighth of the total supplied RF power was used to excite each these two levels. Level 4, which presents a similar excitation pattern of Level 1 [121], was chosen to be excited with one-quarter of the total supplied RF power. In order to compare this arrangement with other possible configurations, B_1^+ shimming optimizations were performed by randomly permuting the Tx channels amplitudes with the four specified values described in Figure 28b and Figure 28c and then performing phase-only optimizations.

5.2.3 Computational Implementation of B_1^+ Shimming with SAR Constraints

The most homogeneous result from the B_1^+ optimizations was used as the initial condition for SAR constrained optimizations. SAR constraints were incorporated into the optimization software by sampling the electric fields (random points sampled for every 4x4x4 voxels) and calculating the average SAR in these points; a method inspired by the Virtual Observation Points method [71]. This method represents a good estimation of the global average SAR and was used to speed up the optimizations. It is worth noting that this method was only applied inside the iterations of the optimization software, the final SAR was calculated according with the 10g averaging guidelines, using the non-sampled Electric Fields. The SAR was constrained from the

initial case to a minimum value in steps of 0.01W/kg for a mean B_1^+ field = 1.97μT in the ROI. Each case was repeated three times (resampling the electric field) to ensure convergence, accuracy, and repeatability. Using the output of the SAR constrained optimizations, the global and local 10g SAR were calculated using the original electric fields (no sampling applied) and scaled per 1W input power. The SAR efficiency is also presented, defined as mean B_1^+ in the ROI (Figure 28g) divided by the square root of the average SAR in the whole head [$\mu T/\sqrt{W/Kg}$].

5.2.4 Numerical Validations of the Implemented RF Shimming Scheme

To demonstrate the efficacy of the method in searching for the global minimum for the cost functions, the RF shimming optimizations using Active-set and Interior-points algorithms were compared with approximately one million randomly generated RF shim cases. These randomized cases were generated by keeping the amplitudes constant while randomly varying the phases of the individual RF fields.

5.2.5 Experimental Implementation and Set-up

Two RF shimming cases were experimentally implemented using coaxial cables as fixed phase shifters and Wilkinson power splitters (Figure 28b). The imaging experiments were conducted in a whole body 7T scanner (MAGNETOM, SIEMENS, Germany) with 8kW power amplifier capabilities. In-vivo experimental data were acquired in healthy volunteers with informed consent as part of a study approved by the local Institutional Review Board.

Whole brain/cerebellum B_1^+ maps were acquired using the Turbo-FLASH sequence. The parameters used were: TR/TE = 2000/1.16 ms; flip angle from 0° to 90° in 18 degrees increments; acquisition time = 12 min, resolution 3.2mm isotropic. The output was fitted to a cosine function to produce the flip angle maps. Moreover, 2D FLAIR and 3D T2-SPACE sequences were used to acquire whole-brain T2-weighted images, for demonstration purposes. The sequences parameters were: 1) 2D FLAIR, TE/TI/TR = 103/2900/13500 ms, BW = 230 Hz/pixel, resolution 0.7x0.7x2 mm^3, 4 interleaved acquisitions, totaling 4:28 min (1:07 min each) and 64 slices (16 slices each); 2) 3D T2-SPACE sequence (WIP692), TE/TR = 369ms/3.4s, BW 488 Hz/pixel, T1/T2 = 1500ms/250ms, 224 slices in transversal acquisition, and acquisition time = 8:11min. These sequences have been routinely acquired on more than 200 subjects.

5.3 Results

Figure 29a and Figure 29b compares the measured and simulated scattering parameters of the 16-channel TTT array. The coupling pattern is highly comparable between the experimental measurements and the simulation data. The measured coupling between the opposite excitation ports of each TTT panel (highest coupling of the design) was -4.26dB on an average while the simulated value was -2.68dB on average. This is attributed to losses in the coil's copper, elements, ports, and cables that are not included as part of the FDTD modeling. The measured maximum coupling between any pair of panels was -17.0dB while the measured average coupling between channels of different panels was -24.4dB.

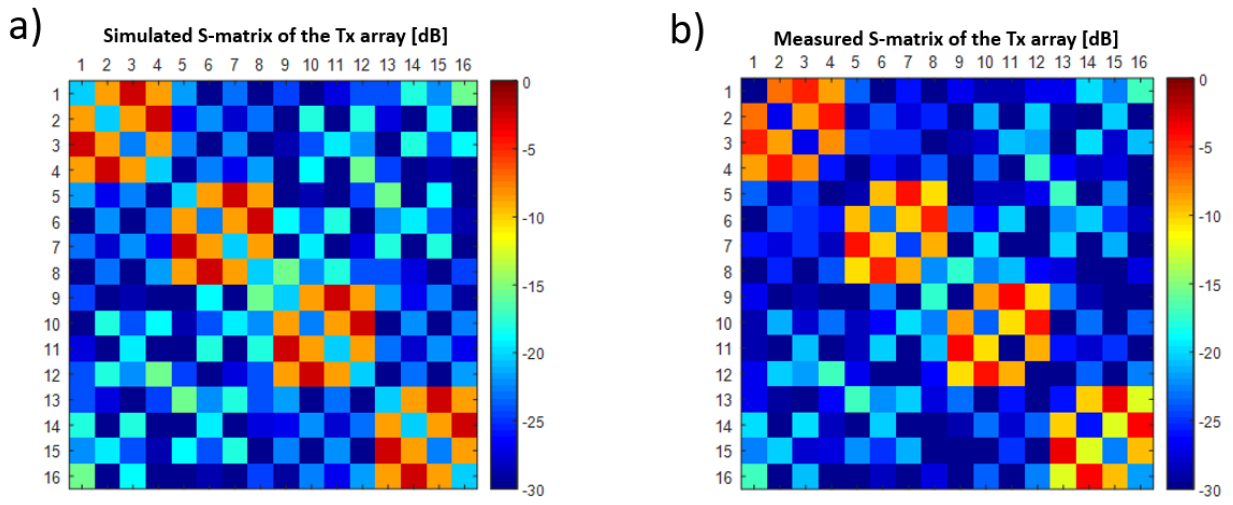

Figure 29: S-parameter comparison between simulations and experiments. In a), the FDTD simulated s-matrix using an accurate transmission line model mechanism; in b), the experimental measurements on a spherical water-based phantom.

Figure 30a and Figure 30b show the comparison between the phase-only B_1^+ shimming (without SAR constraints) based on the proposed power splitter configuration (Figure 28b) with 1) a voltage amplitude scheme for the 4 levels/16 Tx channels (described in Figure 28b) and 2) permuting output of the proposed power splitter configuration into the 16 Tx channels of the coil. Approximately 300,000 phase-only B_1^+ shimming numerical optimizations were performed to address the permutations. The results based on the proposed voltage amplitude scheme demonstrate superior performance in terms of $CV_{B_1^+}$, $max_{B_1^+}/\ min_{B_1^+}$, and $min_{B_1^+}$. A case (indicated by the black arrow in Figure 30a and Figure 30b with high homogeneity (i.e., low $CV_{B_1^+}$ and $max_{B_1^+}/\ min_{B_1^+}$) and high $min_{B_1^+}$ was chosen as the starting point for the SAR-constrained cases and potential experimental implementation. The statistics for this case are: $CV_{B_1^+}$ = 17.7%; $max_{B_1^+}/\ min_{B_1^+}$ = 3.18; $min_{B_1^+}$= 0.14μT for 1W input power.

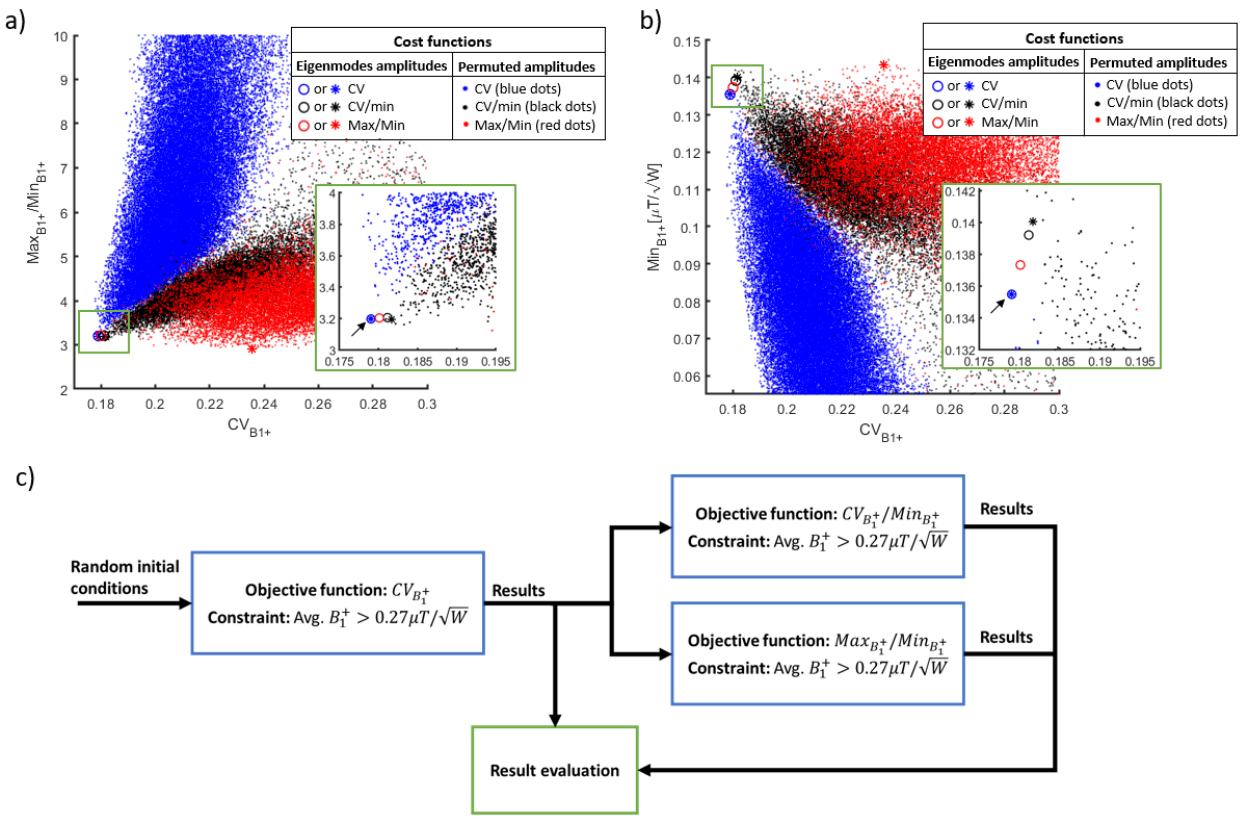

Figure 30: Phase-only RF shimming cases for the 16-channel Tic-Tac-Toe RF array (only considering parameters of the B_1^+ field). The goal of the analysis is to exclusively utilize 2-way and 4-way splitters for implementation on the sTx mode. In a) and b), phase-only RF-shimming cases, with the amplitude scheme derived from the eigenmodes of the RF array (described in Figure 28b) and in (26), were compared with RF shimming optimizations where the amplitudes of the Tx channels were randomly permutated but can only take on normalized values = 1, 1/√2, or 0.5. Approximately 300,000 optimizations were performed, presented as the colored dots. The cost functions for the RF shimming optimizations were the $\boldsymbol{CV_{B_1^+}}$, $\boldsymbol{CV_{B_1^+}/min_{B_1^+}}$, and $\boldsymbol{max_{B_1^+}/min_{B_1^+}}$. The region of interest for the B_1^+ field stats is the entire head from cerebellum excluding the nasal cavities and the ears (Figure 28g). The black arrows point to the case (B_1^+ homogenous shim) selected for experimental implementation in the sTx mode, which was chosen due to having a combination of low $\boldsymbol{CV_{B_1^+}}$, low $\boldsymbol{max_{B_1^+}/min_{B_1^+}}$, and high $\boldsymbol{min_{B_1^+}}$. The circles represent the RF shimming with the best $\boldsymbol{CV_{B_1^+}}$ for a determined cost function and the asterisks are the cases with the best $\boldsymbol{max_{B_1^+}/min_{B_1^+}}$ for each cost function. In c), the simplified flowchart of the optimization strategy used in a) and b).

Figure 31 shows the variations of the B_1^+ field characteristics with the inclusion of SAR constraints as part of the B_1^+ shimming. While higher SAR efficiency and lower average SAR can be achieved, it usually comes at the cost of lower levels of B_1^+ field homogeneity (higher $CV_{B_1^+}$ and/or $max_{B_1^+}/min_{B_1^+}$). The metrics $max_{B_1^+}/min_{B_1^+}$ (Figure 31a), $min_{B_1^+}$ (Figure 31b), and peak SAR (Figure 31c) are affected by the inclusion of SAR constraints.

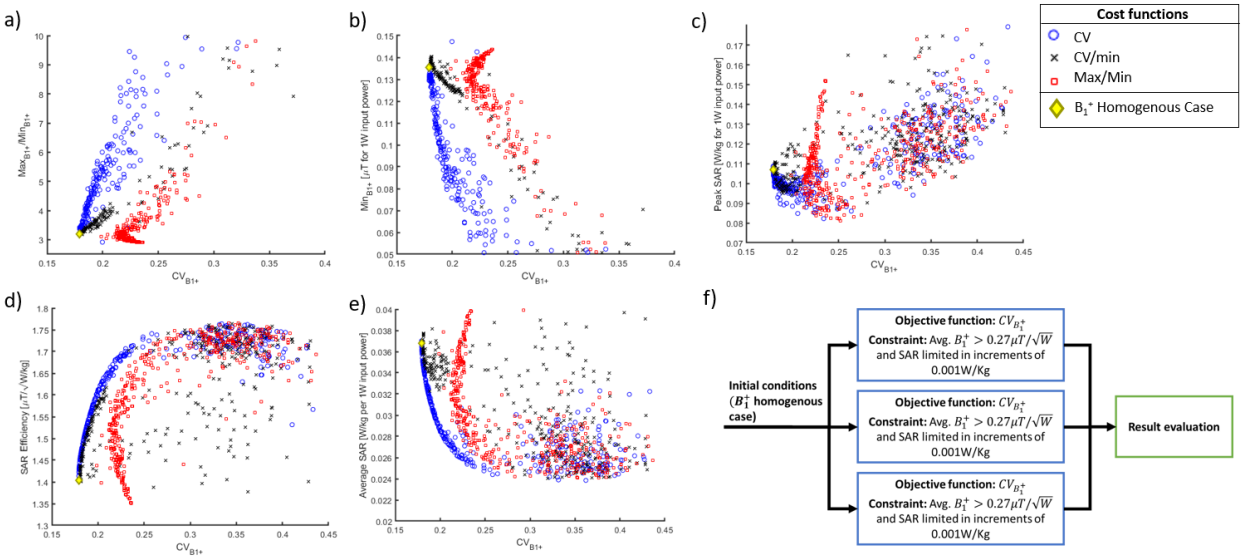

Figure 31: SAR-constrained phase-only RF shimming optimizations of the 16-channel Tic-Tac-Toe RF array (considering both the B_1^+ field and SAR parameters). In each iteration, the SAR was calculated from the electric fields randomly sampled in 4x4x4-pixels blocks that cover the whole head. The SAR was constrained in steps of 0.01W/kg over the whole head for a fixed mean B_1^+ field intensity in the region of interest (described in Figure 28g) for all optimizations. The accurate SAR (without sampling the electric fields) values were then calculated for the entire head and are shown in the graphs. In a) to e), multiple scattering plots showing the results from the SAR-constrained optimizations. In f), the simplified flowchart of the optimization strategy used.

Figure 32 show a comparison of two experimentally-implemented non-subject specific RF shim cases on the same volunteer. The first case (top row) is intended for higher SAR efficiency and RF power efficiency and the second case (bottom row) is intended for higher B_1^+ homogeneity. Figure 32a and Figure 32b show the simulated and experimental B_1^+ maps for the two RF shim cases as well as their associated statistics and FLAIR sequence acquisition. Figure 32c shows profiles central slices comparing the experimental and simulated B_1^+ field for the two RF shim cases. The impact of B_1^+ field inhomogeneities can be seen near the white arrows shown on the B_1^+ field distributions and the FLAIR images. The statistical data demonstrate 1) the intricate relationship between SAR and B_1^+ field, 2) the Tx array capability in exciting homogeneous B_1^+ field distribution with high SAR efficiency [34], and 3) the excellent agreement between simulation and experimental results.

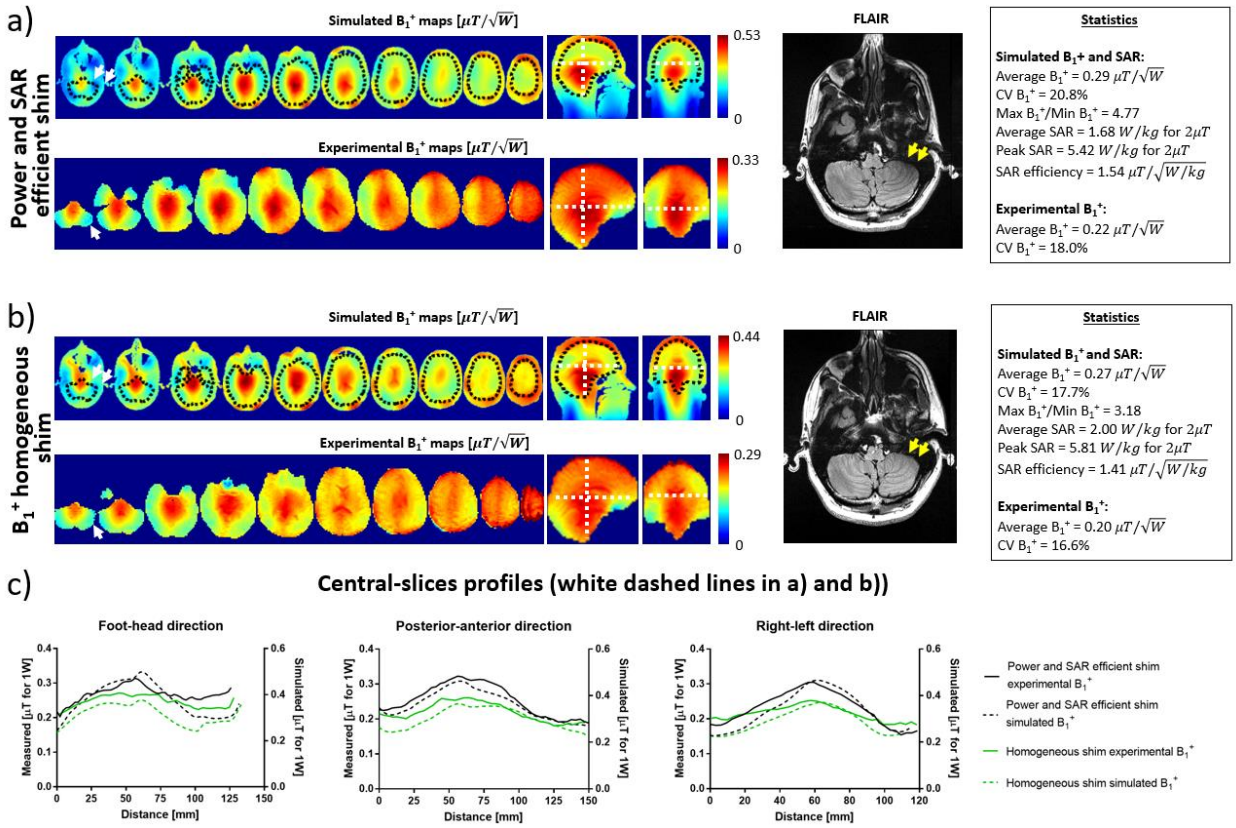

Figure 32: . B_1^+ maps comparison between simulations and experiments for 2 RF shimming cases and FLAIR images. In a), simulated and in-vivo B_1^+ maps, FLAIR acquisition, and major statistics of the shimming case optimized for power and SAR efficiency. The statistics from the simulations were calculated over the region of interest shown in Figure 1g. The black dashed lines are the location of the brain and the white dashed lines are the central slices chosen for the profile curves. In b), simulated and in-vivo B_1^+ maps (same subject as a)) and FLAIR acquisition (same subject as a)) for the shimming case optimized for B_1^+ homogeneity. In c), the central slice profiles from the simulated and experimental B_1^+ maps.

Figure 33 shows representative slices of the T2-weighted 3D SPACE sequence acquired in a volunteer with large head size (approximately 205 mm in the anterior-posterior direction from the forehead) using the B_1^+ homogeneous shim case described in Figure 32. The acquisition demonstrates full brain coverage, including the cerebellum and temporal lobes.

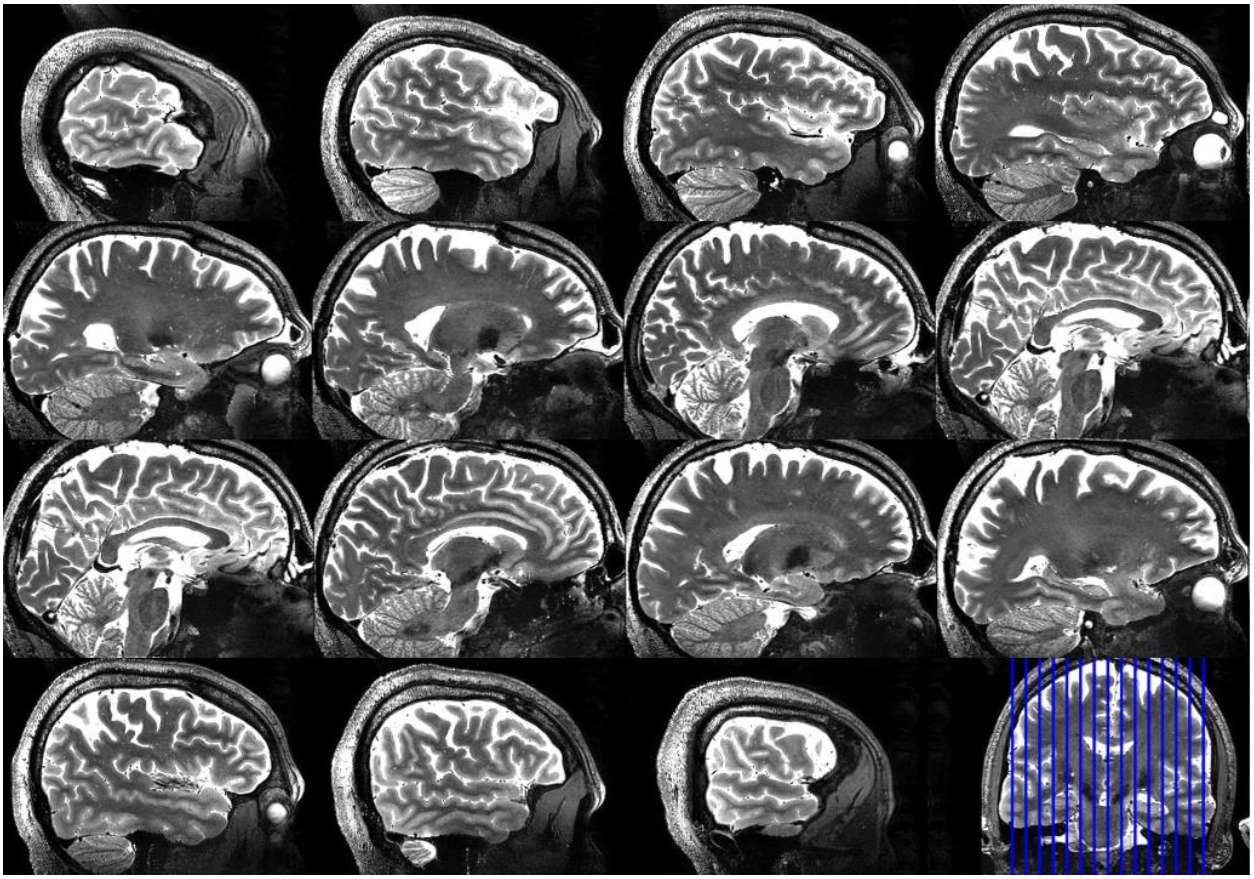

Figure 33: Sagittal slices of the 3D-SPACE acquired at 0.6mm isotropic resolution, showing full brain and cerebellum coverage in a volunteer with large head size (~205mm in AP direction from the forehead). The images are obtained using the Homogenous B_1^+ shim case on the sTx mode. The parameters of the acquisition were: TE/TR = 367/3400 ms, acceleration factor 3, BW = 434, transversal acquisition of 224 slices, field of view 192x165.6mm in axial plane, and acquisition time = 8:11 min. The receive profile was removed using the SPM software.

5.4 Discussion and Conclusion

In summary, a 16-channel transmit array based on the Tic-Tac-Toe design was optimized using non-subject specific phase-only RF shimming. The RF shimming approach combined with the array's 4 excitation levels in the Z direction can significantly impact the Tx array performance by introducing beneficial tradeoffs among RF power efficiency, B_1^+ field homogeneity, and SAR. These parameters can be controlled, depending on the imaging application and RF amplifier capacity, by changing the lengths of the coaxial cables feeding the array.

5.4.1 S-matrix Comparison

The RF transmit array was simulated with a transmission line algorithm for modeling the excitation and coupling as part of the FDTD package. Electromagnetic modeling of the coil's coupling is critical for determining the phases and amplitudes used in in-vivo RF shimming that is fully based on B_1^+ and electric fields calculated using electromagnetic simulations.

5.4.2 B_1^+ Shimming (without SAR Constraints)

The amplitudes for the Tx channels were chosen based on the eigenmodes of the RF array so that the most efficient coil levels (demonstrated in [121]) are excited with higher supplied RF power. This approach was demonstrated to produce superior homogeneity (Figure 30a) and fewer regions with low B_1^+ intensity (Figure 30a and Figure 30b) when compared with other possible

phase-only combinations and using the same power splitter configuration, which can be easily constructed using 2-way and 4-way RF power splitters.

The described B_1^+ shimming scheme also presented superior performance when compared with randomized phase-only B_1^+ shimming (Figure 30c and Figure 30d) as it potentially achieved operational points close to the global minimum of the cost functions. The ROI – which includes the whole head from the cerebellum and excludes the nasal cavities rather than a specific brain size (in the case of a brain-only ROI) – was chosen so that the RF fields become more consistent with different brain sizes.

5.4.3 B_1^+ Shimming with SAR Constraints

Figure 31 shows the flexibility of the phase-only RF shimming scheme in combination with the TTT array, with the tradeoffs between SAR and B_1^+ field performance. A homogeneity of 17.7% ($CV_{B_1^+}$) can be achieved within ROI without any SAR constraints, resulting in a SAR efficiency of ~1.4 $\mu T/\sqrt{W/kg}$. The use of SAR constraints can improve the SAR efficiency to the level of ~1.6 $\mu T/\sqrt{W/kg}$ while maintaining $CV_{B_1^+}$ under 20% and still achieving the same mean B_1^+ field. The values simultaneously attained for SAR efficiency and B_1^+ field homogeneity represent excellent performance for 7T RF head coils. For 7T neuro MRI, the double row loop coil achieves 0.76 $\mu T/\sqrt{W/kg}$ [90, 104]; the birdcage coil achieves 0.89 $\mu T/\sqrt{W/kg}$ [105]; and TEM coil achieves 1.07 $\mu T/\sqrt{W/kg}$ (SAR and B_1^+ field are considered in the whole head using the Visible Human Project model) [130] and 1.25 $\mu T/\sqrt{W/kg}$ (B_1^+ field is considered in the

whole head above and including cerebellum and excluding the nasal cavities and the SAR is calculated in the whole head using the Duke model) [34].

In general, the $CV_{B_1^+}$ as the cost function presented an excellent performance for this particular RF array design in terms of achieving trade-offs between minimizing $CV_{B_1^+}$ and $max_{B_1^+}/min_{B_1^+}$ (Figure 31a) as well as average and peak SAR (Figure 31c-e). It is important to note that the optimal cost function may vary depending on the RF array design, the constraints included in the simulation, and/or the ROI used.

5.4.4 Experimental Verification

Figure 32c shows a comparison between the simulated and measured profiles. The differences in the intensity can be explained by the losses in the splitters/cables/connectors (approximately 17% measured loss in voltage) and losses in the coil. The differences in the field distribution can be due to the model approximations and differences in the head model size and position when compared with in-vivo (the Duke head model brain is about 14cm long in foot-head direction, while the volunteer is about 12.5cm, for example).

Figure 32a and Figure 32b demonstrate the experimental implementation of the RF shimming scheme in conjunction with the TTT array. In Figure 32a, a power and SAR efficient RF shim case is shown where a SAR efficiency of 1.54 $\mu T/\sqrt{W/kg}$ (simulated), average B_1^+ of $0.22\mu T/\sqrt{W}$ (measured), $CV_{B_1^+}$ of 18% (measured), and $max_{B_1^+}/min_{B_1^+}$ of 4.77 (simulated) are achieved. With the B_1^+ homogeneous RF shim case (Figure 32b), SAR efficiency of 1.41 $\mu T/\sqrt{W/kg}$ (simulated), average B_1^+ of 0.20 $\mu T/\sqrt{W}$ (measured), $CV_{B_1^+}$ of 16.6%

(measured), and $max_{B_1^+} / min_{B_1^+}$ of 3.18 (simulated) are achieved. High flip angle (FLAIR sequence) images demonstrate the difference between the two RF shimming cases inside the cerebellum, which is a very challenging region for 7T MRI [131, 132].

3D 7T T2-SPACE whole-brain and cerebellum images are shown in Figure 33 using the B_1^+ homogeneous RF shim case implemented on the sTx mode. The results demonstrate whole-brain, including the temporal lobes and cerebellum, homogeneous imaging in a volunteer with large head size (approximately 205mm in anterior-posterior direction from the forehead) in a challenging sequence at 7T MRI [133-135]. The B_1^+ homogeneous RF shim case (Figure 32b) is currently being used with the sTx mode on several patient studies conducted in our facility due to its high B_1^+ homogeneity and extended coverage in challenging-to-image regions in the head at 7T without the use of dielectric pads or multiple acquisitions.

The TTT head transmit array has significantly lower power efficiency than most 7T RF head coils. This is attributed to the strong coupling between opposite elements of the TTT coil, which causes the transmitted power to be dissipated on the power splitters or in a circulator (located away from the scanner), rather than on the load. For instance, the two RF shim cases presented in this work have a mean B_1^+ of 0.27 and 0.29 $\mu T/\sqrt{W}$ in the simulations (not considering losses in the hardware). Using the same software environment, Narayanan et al. demonstrated that the 4-channel 16-element TEM resonator (with the same length as the TTT array) presents an power efficiency of 0.45 $\mu T/\sqrt{W}$ [34]. However, the TTT array still provides enough mean B_1^+ intensity to have inversion using 1ms square pulse with 8kW power amplifier (standard in older 7T scanners). This calculation also considers the RF losses between the RF power amplifier and coil plug, as well as the cables, power splitters, and coil shields/ports (totaling more than 4kW).

5.5 Publications Related to this Chapter

Tales Santini, et al. *"RF developments for achieving homogeneous transmit field and reduced SAR for 7 Tesla neuro MRI"* (under review).

Tales Santini, Sossena Wood, Narayanan Krishnamurthy, Tiago Martins, Nadim Farhat, Salem Alkhateeb, Howard J. Aizenstein, Tamer S. Ibrahim. *"Optimization of RF system for homogenous, consistent, and safe neuro imaging at 7T MRI"* ISMRM 2019

Tales Santini, Sossena Wood, Narayanan Krishnamurthy, Yutong Zhang, Howard Aizenstein, Tamer S. Ibrahim. *"New optimization strategies for RF shimming at UHF MRI*" In Proc. of the 26th International Society of Magnetic Resonance in Medicine Annual Meeting, Paris, France, 2018.

Tamer Ibrahim, **Tales Santini**, Shailesh Raval, Narayanan Krishnamurthy, Sossena Wood, Junghwan Kim, Yujuan Zhao, Xiaoping Wu, Essa Yacoub, Howard Aizenstein, Tiejun Zhao. *"Towards Homogenous 7T Neuro Imaging: Findings and Comparisons between 7T TTT and NOVA RF Coil Systems."* In Proc. of the 25th International Society of Magnetic Resonance in Medicine Annual Meeting, Honolulu, Hawaii, April 2017.

6.0 Highly Parallel Transmit Array for 7T MRI

6.1 Introduction

Magnetic Resonance Imaging (MRI) is excellent for soft tissue imaging and determination of its metabolites. This technology usually provides high-resolution images with several different contrasts and it is widely utilized in clinical settings. The signal from the MR acquisitions is proportional to the main magnetic field (B_0). Therefore, going from the regular clinical scanners – with the magnetic field of 1.5 Tesla (T) or 3T – to the recent FDA cleared 7T MRI gives a major advantage of increased signal-to-noise ratio. This can be used to increase the resolution of the images or decrease the scanning time (with the use of higher acceleration factors.) Other advantages are the higher sensitivity to blood-oxygen-level-dependent (BOLD) imaging and to venous vasculature, as well as improved angiography and MR spectroscopy acquisitions.

However, with the increased operational frequencies of the radiofrequency (RF) coils at 7T field intensities (or higher), traditional approaches (i.e. birdcage coil) fail to deliver a homogenous circularly polarized magnetic field (B_1^+) over large regions of interest, such as head or torso. Moreover, the shorter skin depth combined with the shorter wavelength can increase the local and global specific absorption rate (SAR) in the tissues. This becomes a safety issue as it can potentially cause temperature increase and tissue damage.

The 16-channel Tic-Tac-Toe (TTT) head coil design has been shown homogeneous B_1^+ over the whole brain, including the cerebellum, with low levels of peak and average SAR [20, 34, 121]. This design has been utilized in more than 750 subjects in patient studies funded by the National Institutes of Health.

This work demonstrates the potential of a new generation of the TTT head coil. The original 9-inch (229 mm) panels were reduced to 4.25 inches (108 mm), allowing the increased number of channels and, in turn, an increased number of degrees of freedom in the coil optimization. Two versions are presented in this work: the first version has 64-channels, in 16 panels located around the head; the second version has 56-channels, with an extension for a future receive insert and an opening for improved patient comfort and to facilitate the visualization of the projected tasks in functional MRI (fMRI). Electromagnetic simulations are presented, and a proof of concept is shown utilizing experimentally acquired B_1^+ maps on a spherical phantom and in-vivo.

6.2 Methods

6.2.1 RF Array Modeling and Electromagnetic Simulations

The Tic-Tac-Toe (TTT) transmit RF coil design has been utilized for several applications at 7T MRI, including foot/ankle [35], breast [26, 136], torso [87], and neuro [34, 121]. The TTT design is composed of eight square-shaped transmission lines interconnected in their termination. The inner rods are composed of square-shaped copper, the outer strut is composed of single layer 8 μm copper sheets (Polyflon, Germany), and the dielectric is made of Teflon machinated using CNC. The outer box was 3D printed in ABS. The plastic and Teflon parts were modeled using AutoCAD (Autodesk, California, USA).

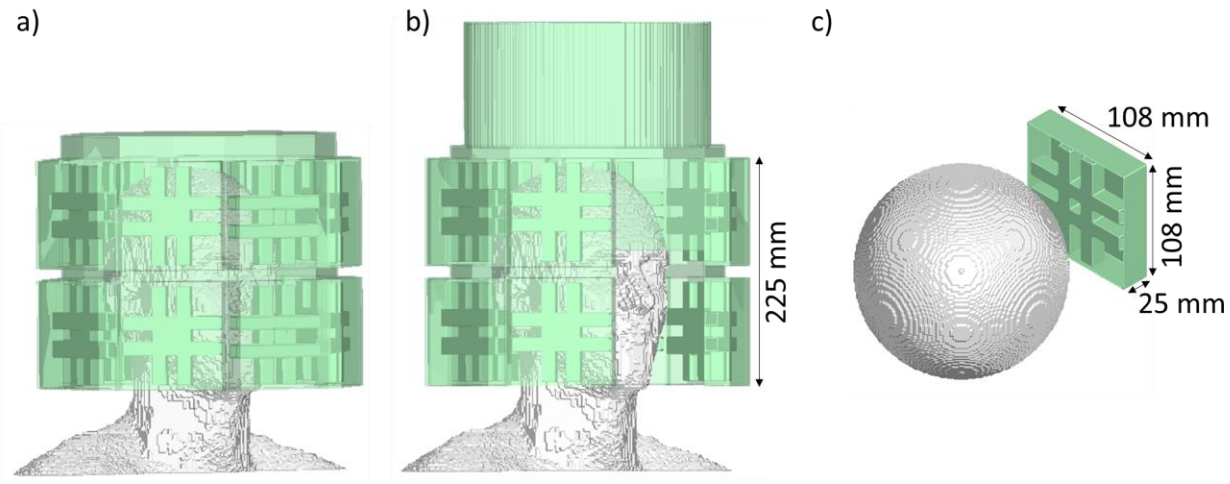

Figure 34: Next generation of the Tic-Tac-Toe RF coil design. In a), the 64 channels TTT transmit array; In b), the 56-channel TTT head array, with an opening in the frontal portion for improved patient comfort and improved field of view for the monitor/projector in fMRI scans; in c), the setup for experimental validation and the dimensions of one TTT side.

Two models are presented in this work: the first version has 16 TTT panels around the head, in two rows of 8 panels, totaling 64 transmit channels. In the second version, the panels close to the face of the subject were removed to improve comfort and provide easier visual access to the monitor/projector during fMRI tasks.

The models were voxelized and the Yee cells were created using Matlab (MathWorks, Massachusetts, USA). An in-house developed FDTD package with an accurate transmission line model was used for the simulation of the RF fields and scattering parameters. This software package has been verified and utilized in several publications of the group [26, 34, 35, 63, 121, 136-140]. The Duke model (from top of the head to shoulders) was used for the simulations, with its conductivity and permittivity adjusted for the 7T frequency (297.2MHz).

6.2.2 RF Excitation and RF Shimming Strategies

The RF array developed in this work is intended to be used in the single transmit channel mode of the MRI scanner, which is the mode cleared by the FDA. To accomplish that, several Wilkinson power splitters are used. The power splitters available commercially for the 7T operational frequency are 1x2, 1x3, 1x4, 1x8 (number of inputs x number of outputs). A Matlab code was developed to determine all possible combinations of splitters that can be implemented in the 64-channel RF array, constraining the number of splitter levels in 3 and each Z-level of the array should have the same power among the channels.

The channels of the RF array are simulated individually. Using the superposition principle, they can be combined into the resultant spatial field distribution. The RF field distribution changes drastically with changes in the phases of the individual channels since it modifies the constructive and destructive wave interactions inside the region of interest. In a technique known as static RF shimming, the amplitudes and phases of the RF pulses injected in the channels are modified towards a specific objective, usually to improve the B_1^+ efficiency and homogeneity and to reduce the global and local SAR.

In this work, the cost functions in Equation 6-1 were used to select the best splitter configuration, as it performs well from random initial conditions (the CV function is smooth over the multidimensional space, facilitating the convergence in gradient descending algorithms). The numerical optimizations used the Matlab function *GlobalSearch*, which utilizes several initial conditions and verifies their convergence. Equation 6-2 was used to further explore the cases found using Equation 6-1.

$$Cost\ function\ 1\ =\ CV_{B_1^+}, contraint\ Avg.B_1^+ >\ 13.5uT \quad (6\text{-}1)$$

$$Cost\ function\ 2\ = \frac{CV_{B_1^+}}{minimum_{B_1^+}}, contraint\ Avg.B_1^+ >\ 13.5uT \quad (6\text{-}2)$$

6.2.3 Experimental Validations of the RF Coil Design

One coil panel was built and used to experimentally verify the coil performance in terms of transmit B_1^+ and reflection coefficient. The TurboFlash sequence was used to estimate the B_1^+ field distribution. A saturation pulse followed by an excitation pulse varying from 0 to 90 degrees (6 steps in total) was utilized. The parameters of the sequence were: TE/TR 1.08/2000ms, 3.2 mm isotropic, bandwidth 1502 Hz/pixel. A transmit/receive box was used, and the 4-channel panel was used as a transceiver. The acquired images were fitted to a cosine function to estimate the B_1^+ [34, 35, 121, 141]. The images were acquired using 7T whole-body MRI (Magnetom, Siemens, Germany). The spherical phantom has a conductivity of 0.46 S/m and relative permittivity of 79; copper sulfite was added to reduce the T1 decay time.

6.3 Results

6.3.1 Determination of the Best Splitting Configuration

All possible power splitting configurations, using 1x2, 1x3, 1x4, or 1x8 splitters in a maximum of 3 layers of splitters, were explored. The total number of possible configurations is 13,819. For each possible configuration, the cost_function_1 (Equation 6-1) was utilized in conjunction with the average B_1^+ constraint and random initial conditions for the phases; for this step, the Matlab functions *GlobalSearch* and *MultiPoint* were utilized, which performs well for random initial conditions as it optimizes multiples initial conditions and checks for convergence. The result was then applied as the initial conditions for a second optimization using the cost_function_2 (Equation 6-2). For this second step, it was also utilized the average B_1^+ constraint, however, it was used the Matlab function *fmincon* and the interior-point algorithm, which searches locally for the best result. The results can be appreciated in Figure 35.

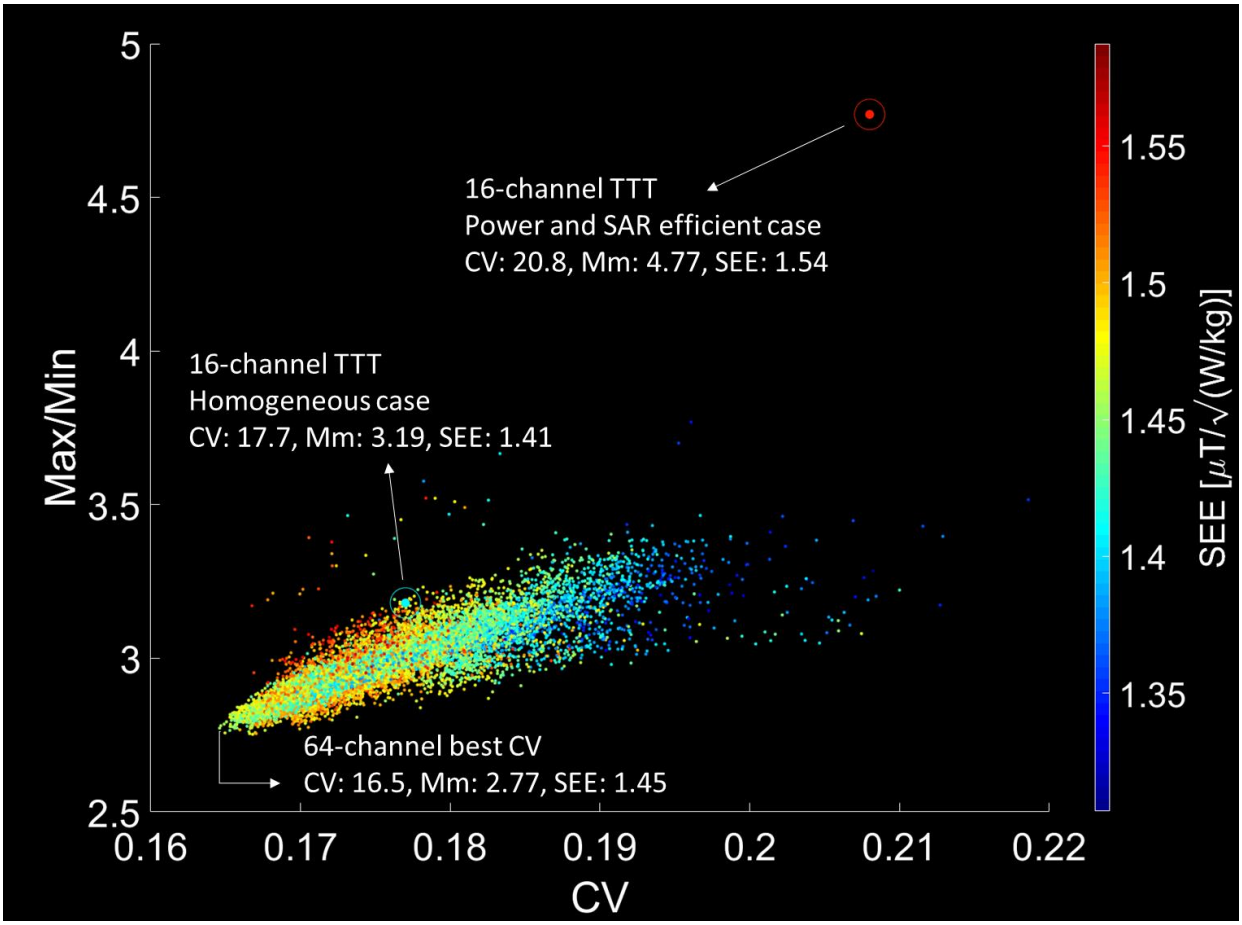

Figure 35: Numerical optimizations of the 64-channel TTT RF array using all possible power splitting configurations for 3 layers of splitters and with commercially available splitting values: 1x2, 1x3, 1x4, and 1x8. The results were then compared with the 16-channel TTT coil. The 64-channel version presented improved homogeneity performance in terms of B_1^+ coefficient of variation (CV) and B_1^+ maximum over minimum (Mm) and improved SAR efficiency (SEE) for the homogenous cases.

The selected splitting configuration shown in Figure 36 was chosen because it demonstrates the highest homogeneity level (i.e., lowest CV) among all tested cases (Figure 35). The amplitudes and phases from this case were used as initial conditions for phase-only optimizations presented in subsection 6.3.2 .

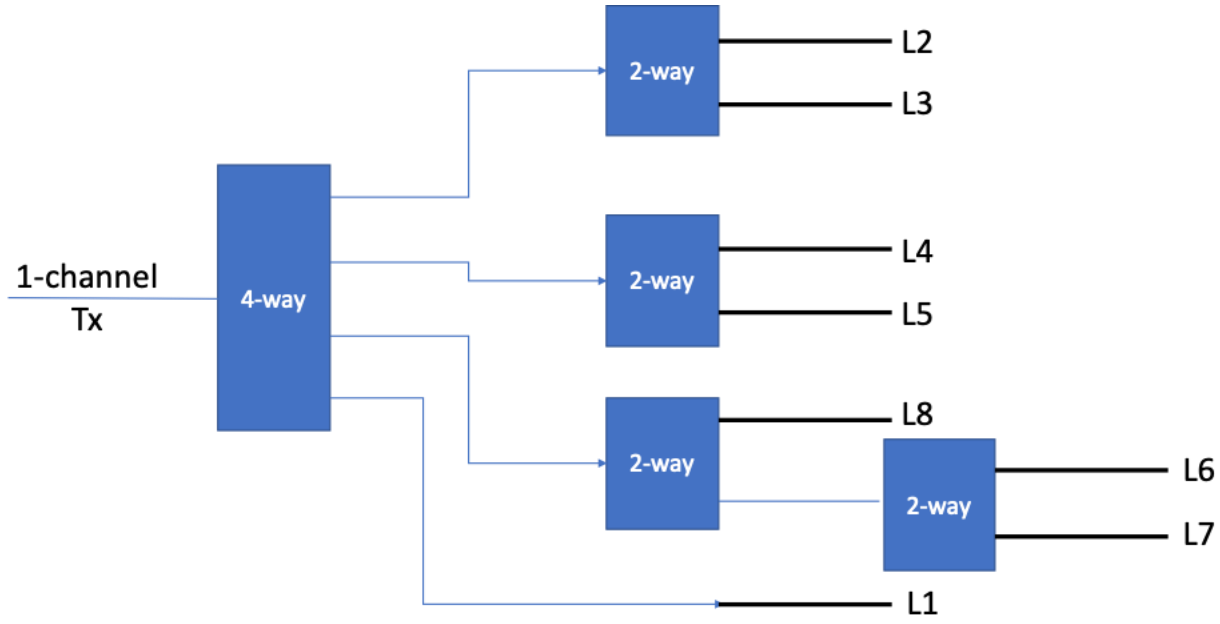

Figure 36: Selected configuration of splitters based on the homogeneity performance. L1 to L8 represents the z-levels of the RF array.

6.3.2 B_1^+ Field Distribution and SAR Maps

Using the power splitting configuration that provided the most homogenous B_1^+ fields (indicated as the best CV case in Figure 35), the two cost functions (Equations 6-1 and 6-2) were utilized combined with different regions of interest in Z direction to produce the two cases of interest (Figure 37). The first case is the "homogenous case", obtained using the cost_function_1, and the region of interest as the whole head, from the lower cerebellum and excluding the nasal cavities and the ears. The second case is called "extended coverage and efficient case", obtained using the cost_function_2, and the region of interest defined as the whole head, extended to below

the cerebellum and excluding the nasal cavities and ears. The B_1^+ field distributions, SAR maps, and major statistics of these two cases are shown in Figure 37.

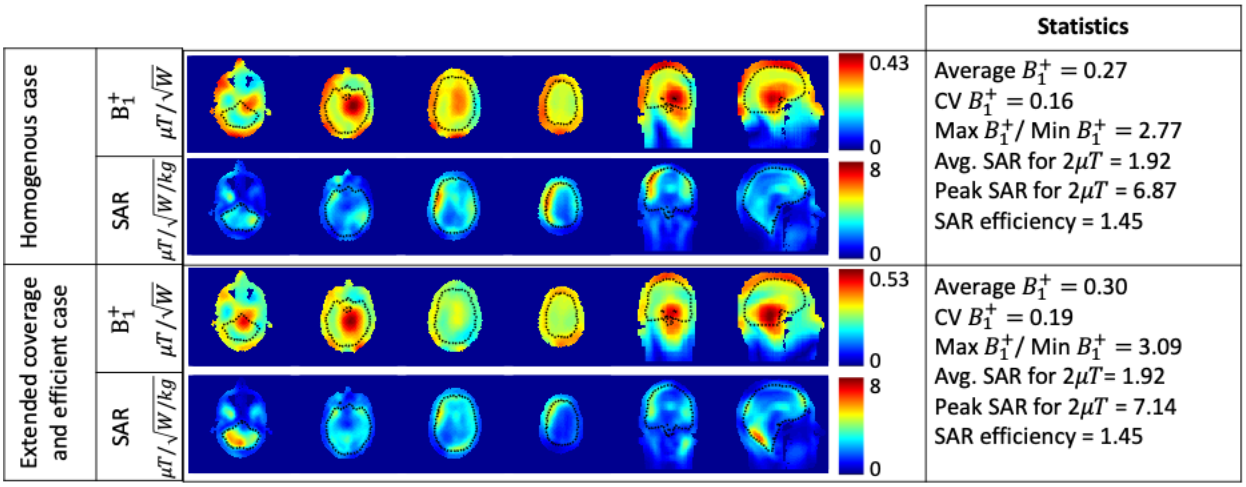

Figure 37: two sample cases of RF shimming of the 64-channel transmit TTT array. Both a homogeneous case and an extended coverage/power efficient case are shown. These cases were generated without SAR constraints.

6.3.3 Experimental Validation

One TTT panel was manufactured as proof of concept as shown in Figure 38a. The simulations of the reflection coefficient were performed using an accurate transmission line model integrated into the FDTD package. The magnitude and Smith chart simulated behavior is shown in Figure 38b. The bench measurements using a network analyzer is shown in Figure 38c.

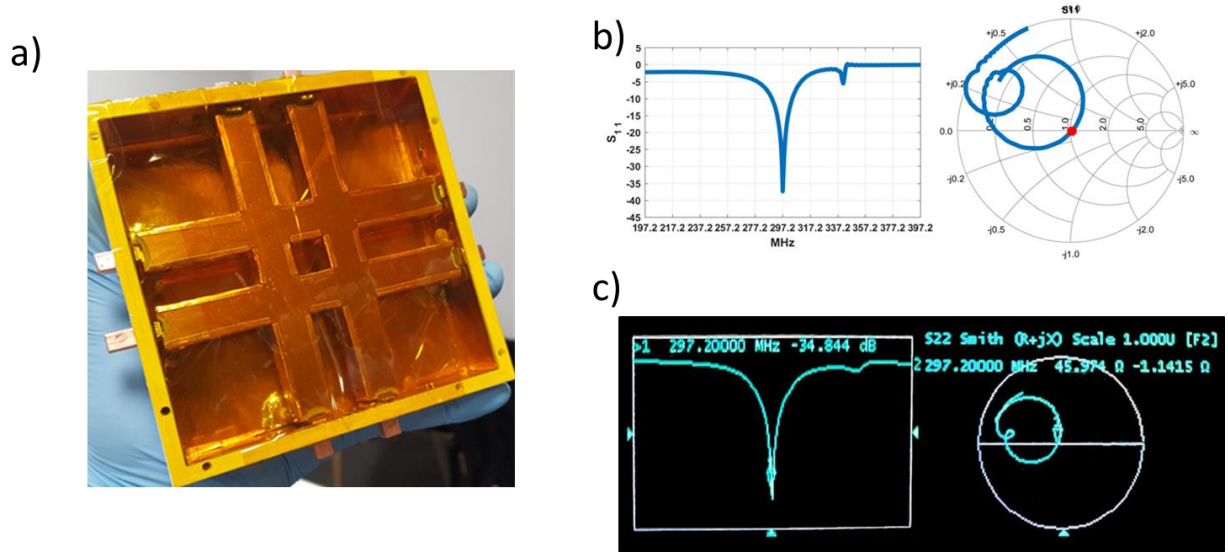

Figure 38: construction of the TTT panel and bench evaluation. In a), the constructed TTT panel, which has 4 channels. In b), the numerical simulations of the reflection coefficient variation with frequency. The coil is tuned for the 7T resonance frequency (297MHz). The simulations were performed using a virtual transmission line model integrated to the FDTD simulations; in c), the experimentally acquired data using a network analyzer on the assembled coil.

The tuned coil was experimentally verified using the 7T scanner. The B_1^+ maps extracted from the turbo flash sequence and the comparison with the simulated are shown in Figure 39. Both simulations and experimental data use a spherical phantom as the load (as shown in Figure 34c.) A transmit-receive box was used to drive the coil, which was positioned in the XY plane in the scanner. The channels were driven in quadrature mode (adjacent channels were driven 90 degrees apart using coaxial cables as phase shifters.)

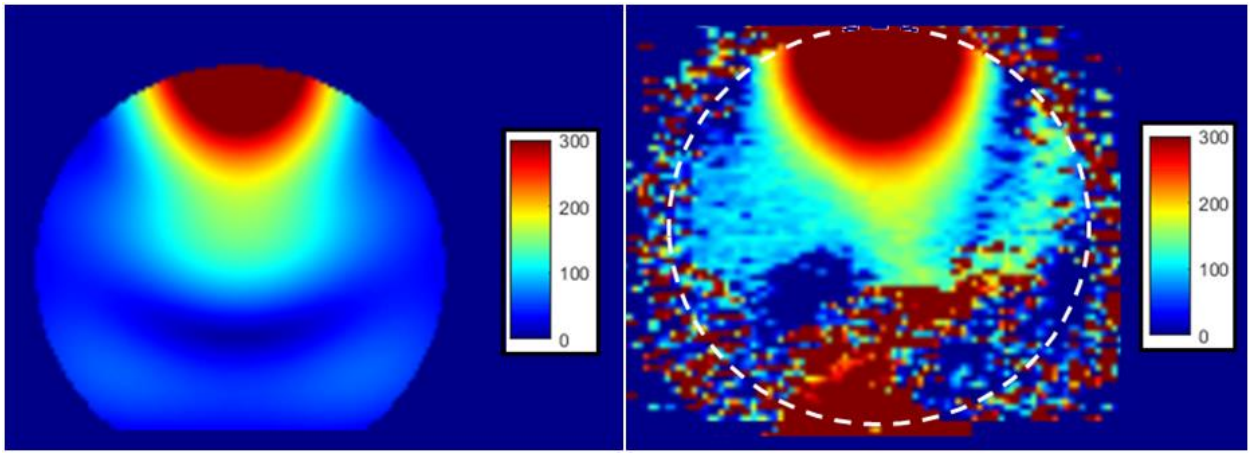

Figure 39: B_1^+ field distribution comparison between simulations (left) and experimental acquired data on spherical water based phantom. The scale is in flip-angle per 500V on the coil plug.

Based on the splitting combination showed at Figure 36 and the cost functions with randomized weights for SAR, CV_B_1^+, and max_B_1^+/min_B_1^+, the scattering plots of Figure 40 and Figure 41 could be generated. Each point shows the results of a numerical optimization. The scaterring plots demonstrate the flexibility of the array, with a trade-off between SAR, CV_B_1^+, and max_B_1^+/min_B_1^+, that can be explored depending on the application.

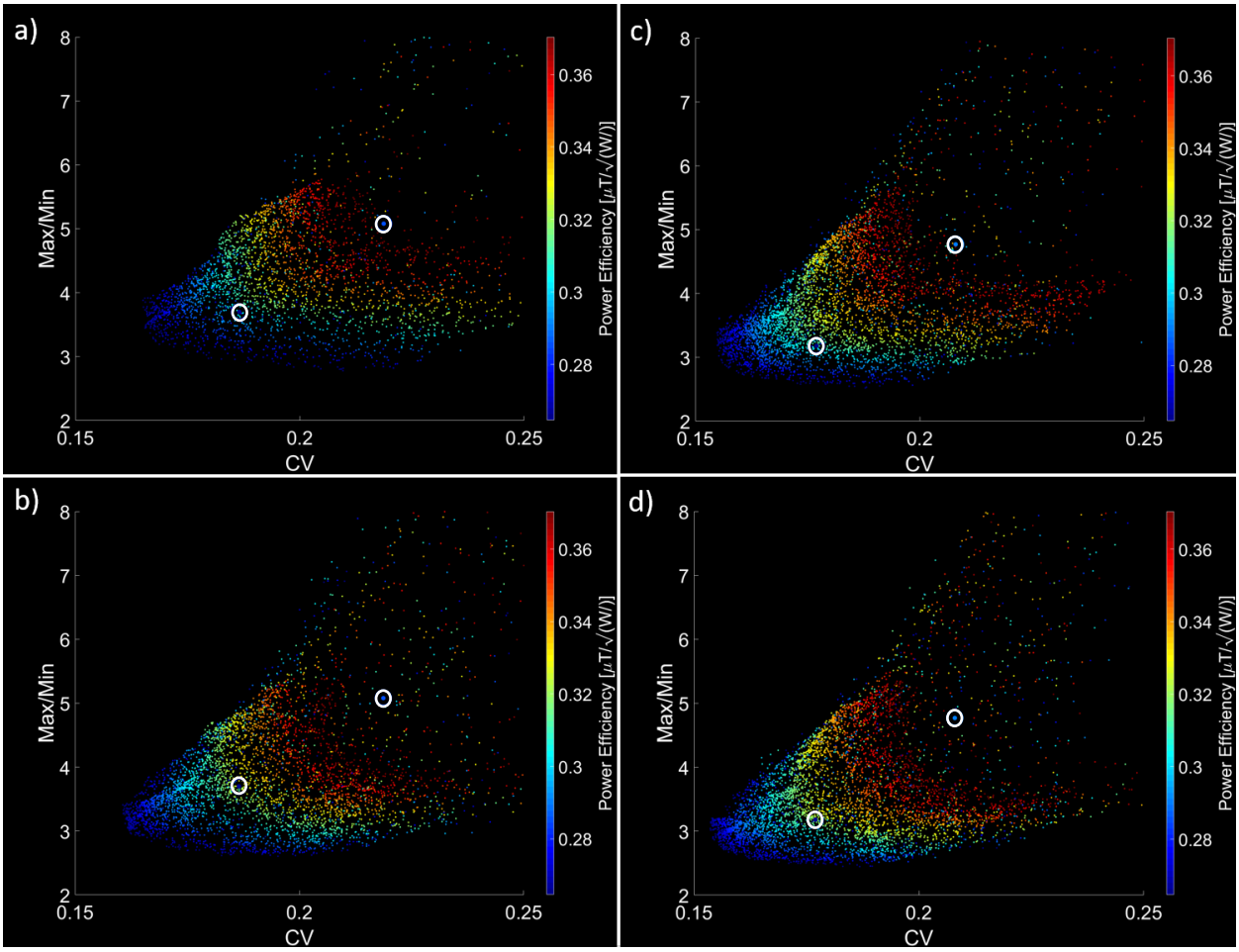

Figure 40: scattering plots of the power efficiency of the 64-channel TTT array for 2 head positions and 2 regions of interest. In a), the head model is in position 1 and the region of interest is calculated from the base of the cerebellum. In b), the head model in position 2 (shifted up 7.7 mm in Z direction) and the region of interest is calculated from the base of the cerebellum. In c), the head model is in position 1 and the region of interest is calculated starting from the middle of the cerebellum. In d), the model is in position 2 (shifted up 7.7 mm in Z direction) and the region of interest was calculated from the middle of the cerebellum. The dot with a white circle represents the homogeneous and the power-efficient cases for the 16-channel TTT array.

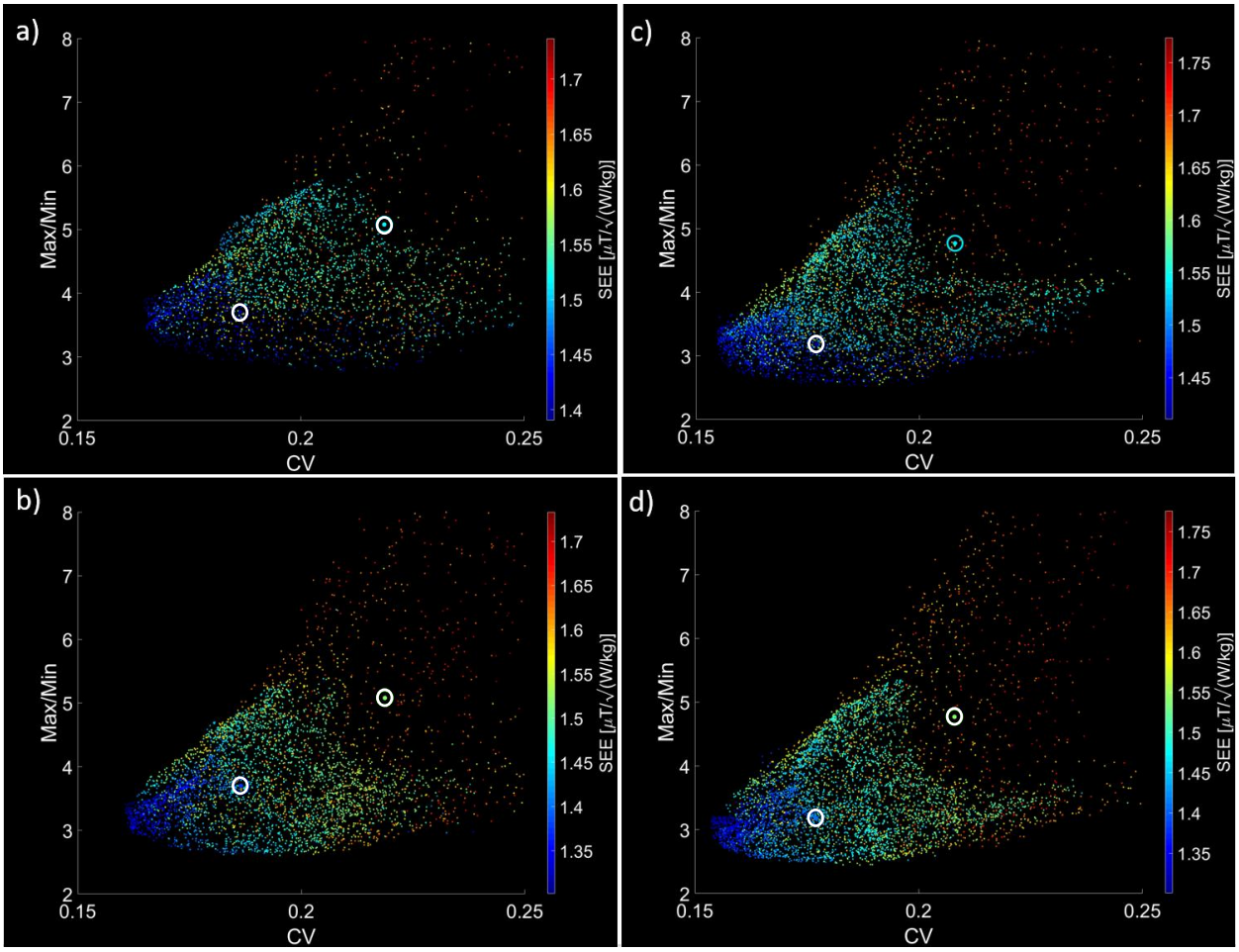

Figure 41: scattering plots of the SAR efficiency (SEE) of the 64-channel TTT array for 2 head positions and 2 regions of interest. In a), the head model is in position 1 and the region of interest is calculated from the base of the cerebellum. In b), the head model is in position 2 (shifted up 7.7 mm in Z direction) and the region of interest is calculated from the base of the cerebellum. In c), the head model is in position 1 and the region of interest is calculated starting from the middle of the cerebellum. In d), the model is in position 2 (shifted up 7.7 mm in Z direction) and the region of interest was calculated from the middle of the cerebellum. The dot with a white circle represents the homogeneous and the power-efficient cases for the 16-channel TTT array.

6.4 Discussions and Conclusion

This work presented the new generation of Tic-Tac-Toe head coil design. The design mimics the original TTT design but reduces the size of each element to half of the original length (1/4 of the area), enabling the increase of the channel number from 16 to 64 channels. Consequently, the increased number of channels improves the degrees of freedom for RF shimming of the array, adding flexibility to the design for optimizations aiming specific objectives, such as efficiency, homogeneity, average or peak SAR minimization, or a combination of these objectives.

All the combinations of power splitting were evaluated for commercially available Wilkinson power splitters (1-way, 2-way, 3-way, 4-way, and 8-way) and 3 layers of splitters, resulting in 13819 possible combinations. Figure 35 showed that the splitting configuration highly affects the B_1^+ field and SAR performance. The most homogenous splitting configuration was chosen as the amplitudes and initial conditions for the phase-only RF shimming.

While this is still a work in progress, these results presented in this chapter motivates the full construction of the RF array. In terms of B_1^+, this array presents a CV of 16.5% and a maximum/minimum of 2.77. This represents an improvement of 7%/20% in the CV and 13%/42% in the maximum over minimum in the homogenous/efficient case for the 16-channel TTT.

Two phase-only RF shimming cases using the amplitudes defined in Figure 36 are presented: a homogenous case and an efficient/extended coverage case. These cases showed the flexibility of the design. Several other cases can be generated using phase-only shimming of the 64 channels, creating a trade-off between homogeneity, B_1^+ efficiency, and SAR efficiency.

The two RF shimming cases presented in this work were obtained without the use of SAR constraints. The inclusion of SAR constraints is expected to improve the average and peak SAR levels of the RF array without affecting substantially the B_1^+ performance.

Another version of the RF array is being considered for construction. Shown in Figure 34b, the front panels of the array were removed for patient comfort and to increase the visual field of view of the patients in functional MRI studies. Preliminary results (not shown) indicates similar performance when compared with the 64-channel RF array.

6.5 Publications Related to this Chapter

Tales Santini, Sossena Wood, Howard J. Aizenstein, Tamer S. Ibrahim. *"Homogenous 64-channel RF transmit array for brain imaging at 7T, 9.4T, and 10.5T."* ISMRM 2019

Tales Santini, Narayanan Krishnamurthy, Sossena Wood, Shailesh Raval, Yujuan Zhao, Anthony Fischetti, Minseok Koo, Howard Aizenstein, Tamer Ibrahim. *"64-channel Double-Octagon Tx Head Coil for 7T Imaging."* ISMRM 2017.

Minseok Koo, **Tales Santini**, Neilesh Vinjamuri, Sossena Wood, Nadim Farhat, Tiago Martins, Salem Alkhateeb, Tamer S. Ibrahim. *"Building and Testing of the 64-channel Radio Frequency (RF) Head Coil for Ultra-High Field MRI Applications"* BMES 2018

Neilesh Vinjamuri, **Tales Santini**, Sossena Wood, Tamer S. Ibrahim. "*Optimizing geometry of a 64-channel RF head coil*". BMES 2017

7.0 Conclusions and Future Direction

7.1 Summary and Findings

7.1.1 Foot and Ankle RF Coil

A four-channel Tic-Tac-Toe (TTT) transmit RF coil was designed and constructed for foot and ankle imaging at 7T MRI. Numerical simulations using an in-house developed FDTD package and experimental analyses using a homogenous phantom showed an excellent agreement in terms of B_1^+ field distribution and s-parameters. Simulations performed on an anatomically detailed human lower leg model demonstrated a B_1^+ field distribution with a coefficient of variation (CV) of 23.9%/15.6%/28.8% and average B_1^+ of 0.33μT/0.56μT/0.43μT for 1W input power (i.e., 0.25W per channel) in the ankle/calcaneus/midfoot respectively. In-vivo B_1^+ mapping shows an average B_1^+ of 0.29 μT over the entire foot/ankle. This newly developed RF coil also presents acceptable levels of average SAR (0.07W/Kg for 10g per 1W of input power) and peak SAR (0.34W/Kg for 10g per 1W of input power) over the entire lower leg. Preliminary in-vivo images in the foot/ankle were acquired using the T2-DESS MRI sequence.

7.1.2 Eigenmodes of a Multilevel Array

In this work, an in-depth analysis of the eigenmodes of a 20-channel transmit Tic-Tac-Toe (TTT) RF array for 7T neuro MRI is presented. The eigenmodes were calculated for five different Z levels (along the static magnetic field direction) of the coil. Four eigenmodes were obtained for

each Z level (composed of 4 excitation ports), and they were named based upon the characteristics of their field distributions: quadrature, opposite-phase, anti-quadrature, and zero-phase. Corresponding finite-difference-time-domain (FDTD) simulations were performed and experimental B_1^+ field maps were acquired using a homogeneous spherical phantom and human head (in-vivo). The quadrature mode is the most efficient and it excites the central brain regions; the opposite-phase mode excites the brain peripheral regions; anti-quadrature mode excites the head periphery; and the zero-phase mode excites cerebellum and temporal lobes. Using this RF array, up to five eigenmodes (from five different Z levels) can be simultaneously excited. The superposition of these modes has the potential to produce homogeneous excitation with full brain coverage and low levels of SAR at 7T MRI.

7.1.3 Homogenous $\mathbf{B_1^+}$ and Reduced SAR RF Array

This work aimed to develop a methodology of operation for achieving homogeneous B_1^+ field distribution with low levels of specific absorption rate and evaluate the performance of the methodology in conjunction with a 16-channel 7T Tic-Tac-Toe transmit array for neuro MR applications. RF shimming was performed using finite-difference time-domain simulations. The amplitudes for driving the Tx array were chosen according to the eigenmodes of the array and compared with other possible configurations. Two phase-only RF shims, based on RF simulations (not subject-specific), were experimentally implemented. In-vivo B_1^+ maps and experimentally measured scattering parameters were compared with the simulations. To evaluate the imaging performance, 2D FLAIR and 3D T2-SPACE 7T images were acquired in-vivo. The fixed amplitudes derived from the eigenmodes of the RF array showed superior performance in relation to other implementable (on the system's single transmit channel mode) configurations. For the two

implemented shim cases: 1) the power and SAR efficient RF shim provided SAR efficiency = 1.54 μT/$\sqrt{}$(W/kg) and 2) the B_1^+ homogeneous RF shim provided coefficient of variation = 16% (measured) and maximum over minimum = 3.2 (simulated) for the B_1^+ field. The 2D FLAIR and 3D T2-SPACE images demonstrate full brain coverage, including the cerebellum and temporal lobes. The Tic-Tac-Toe array combined with phase-only RF shimming was able to deliver a homogeneous B_1^+ field distribution with low levels of SAR and full brain coverage (without utilizing dielectric pads) at 7T. This RF coil system has been utilized in more than 750 patient/volunteer 7T neuro scans.

7.1.4 Highly Parallel Transmit Array for 7T MRI

In this work, a new generation of the Tic-Tac-Toe (TTT) head coil is proposed. The original 9x9-inch panel was reduced to 4.25x4.25-inch, allowing the placement of 16 panels around the head, totaling 64 transmit channel in this new array. Another version is considered, which has 56 channels and improved patient comfort. A total of 13,819 power splitting configurations were evaluated for the coil to be used in the single-channel mode of the scanner: the only mode cleared by the FDA agency to be used in clinical 7T scanners. The splitting configuration that produces the highest homogeneity level was chosen as the initial conditions for phase-only RF shimming. The results showed an improvement in the homogeneity of 7%/20% in the CV and 13%/42% in the maximum over minimum when compared with the homogenous/efficient case for the 16-channel TTT. Besides the homogenous case, an efficient and extended coverage case is shown, demonstrating the flexibility of the design. One coil panel (4 channels) was simulated with a spherical phantom. The reflection coefficient and B_1^+ field distribution were then experimentally

verified using the network analyzer and 7T scanner respectively. This work in progress demonstrated the potential of the new generation of Tic-Tac-Toe head coil.

7.2 Future Directions

The first RF coil presented in this dissertation was the foot and ankle coil for 7T MRI. This work was important due to the lack of a commercial coil for scanning this region of the body at 7T. The next step in this project would be an extended comparison between this 7T foot/ankle coil and a commercial coil at 3T. The homogenous spin excitation presented by 3T scanners would be compared with the 7T advances of higher signal, higher resolution, and improved contrast. Moreover, the search for a clinical application would be beneficial for the project. New coil designs using the TTT can also be investigated. For example, instead of one TTT panel positioned close to the foot sole, two TTT panels could be configured on both sides of the calcaneus. In addition, the RF system currently has a 4-channel receive insert; a higher number of receive loops would be beneficial to the SNR and for fast acquisition with higher acceleration factors.

The second RF coil design presented in this dissertation was the 20/16-channel Tic-Tac-Toe head RF coil. This design was evaluated and optimized, intended to be used in patient studies at 7T. This RF system presents an unprecedented image homogeneity and is able to acquire virtually any clinical sequence used at 7T with high quality (i.e., high resolution, contrast, and full brain coverage.) As of current, there have been more than 750 subjects from patient studies scanned at 7T using this RF system. As a future direction, part of this data could be used to simulate the coil performance (B_1^+ and SAR) in a larger population, using the data acquired in the subjects to generate new head models. The same optimization techniques can be used for a new RF

shimming of the RF coil that can improve performance for a large population, with different head sizes and positions inside the RF coil.

Lastly, this dissertation presented the next generation of TTT head coil design with the 64/56-channel TTT head transmit array. This work in progress has shown promising results, with generally improved RF performance when compared with the 16-channel version. The next steps in this project are: 1) identify a proper RF shimming for the array, with a good compromise among B_1^+ homogeneity, B_1^+ efficiency, and acceptable levels of SAR; 2) implementation of the RF array, likely to be similar to the 56-channel version of the array, since it improves the patient comfort and visual accessibility in functional MRI acquisitions while maintaining the RF performance; 3) implementation of the power splitting to distribute the RF pulse among the channels of the array; 4) construction of a receive RF array, ideally with 32-channels, for improved SNR and the possibility of using high acceleration factors in the image acquisitions.

Appendix A Computational and Experimental Evaluation of the Tic-Tac-Toe RF Coil for 7 Tesla MRI

A.1 Introduction

Evaluating Ultra-high field (UHF) MR/MRSI at 7 tesla (T) and higher as a translational clinical tool has been the focus of several research groups [113, 142-148]. The main advantages of UHF strengths are higher signal-to-noise ratio (SNR), higher spatial resolution, increased sensitivity to T1 & T2 contrast mechanisms and to magnetic susceptibility or blood oxygenation (BOLD) [149-152] . However, the main challenges with UHF strengths remain to be radiofrequency (RF) inhomogeneity and safety restrictions due to subject specific variation and increased power deposition or specific absorption rate (SAR) [153, 154].

At UHF frequencies, the human head size becomes comparable to the RF wavelength (at 7T, the wavelength is approximately 13cm in the brain tissues). As a result, the electromagnetic interactions between the human body/head and the RF coil become increasingly sensitive to variations in the size/shape of the sample [154]. Such interactions can lead to significant variations in the distribution/intensity of the circularly polarized component responsible for excitation (B_1^+) field as well as specific absorption rate (SAR) across different subjects. This issue in addition to the inherent electromagnetic field inhomogeneity and elevated RF power deposition associated with UHF human imaging can have detrimental effects on the quality and safety in high field MRI. Moreover, it is important to assure that the RF excitation does not result in localized SAR across different subjects [155]. While many electromagnetic simulation tools are currently used to

calculate estimates of SAR for RF shimming purposes [156, 157], B_1^+ fields are typically experimentally measured/mapped in an experimental setting.

The adoption of multichannel RF coil designs for UHF MRI allows for multiple degrees of freedom in manipulating the RF fields [158]. As a result, several designs of RF transmit arrays have been proposed to improve RF coil performance, mainly evaluated in its capability to produce homogenous B_1^+ field distributions at acceptable levels of RF tissue absorption [159-161]. It is worth noting however, that several MR sequences and pulse designs can also improve the homogeneity of the spin excitation (as opposed to B_1^+ field distribution), such as adiabatic pulses [115, 116], tailored pulses [162, 163], and transmit SENSE [117, 118] or interleaved excitation of the modes with TIAMO [92, 120].

In this work, we study RF characteristics due to different human heads and compare different coils that are used at 7T. Specifically, the transverse electromagnetic resonator (TEM) coil [23] and 5-sided Tic-Tac-Toe (TTT) coil [121, 164] are evaluated via RF simulations using different anatomically detailed human head models and measurements utilizing a network analyzer and in-vivo 7T B_1^+ mapping on different human heads. We chose the 16-element TEM and TTT designs due to the availability of both coils as well as FDTD coil models in our facility and because they are based on the distributed-circuit approach and have shown to produce the homogenous B_1^+ field distributions at 7T [165, 166]. The detailed analysis is performed by comparing finite-difference time-domain (FDTD) calculated and measured coil impedance, B_1^+ field (homogeneity and intensity) and SAR (average and local) across different heads for both coils.

A.2 Methods

A.2.1 The TTT and TEM RF Coils Design and Construction

Figure 42(A) shows the prototyped cuboid coil. The coil is made out of five sides of a TTT square-shaped array as described in [26, 136, 167, 168]. The 7T TTT head coil is a bigger version (228x228 mm^2) of the breast coil; detailed description of the coil design and construction can be found in [26]. One side of a tic tac toe shaped array has four transmit (Tx) channels/elements Figure 42(D)). The assembly of 5 tic tac toe shaped arrays (surrounding the human head except for the neck side) allows for up to 20 Tx channels/elements. Only 16 Tx channels are used since the top tic tac toe side is not utilized. Each channel of the coil is tuned to 297.2 MHz by adjusting the inner rod length pushed inside the outer strut for all the coil elements.

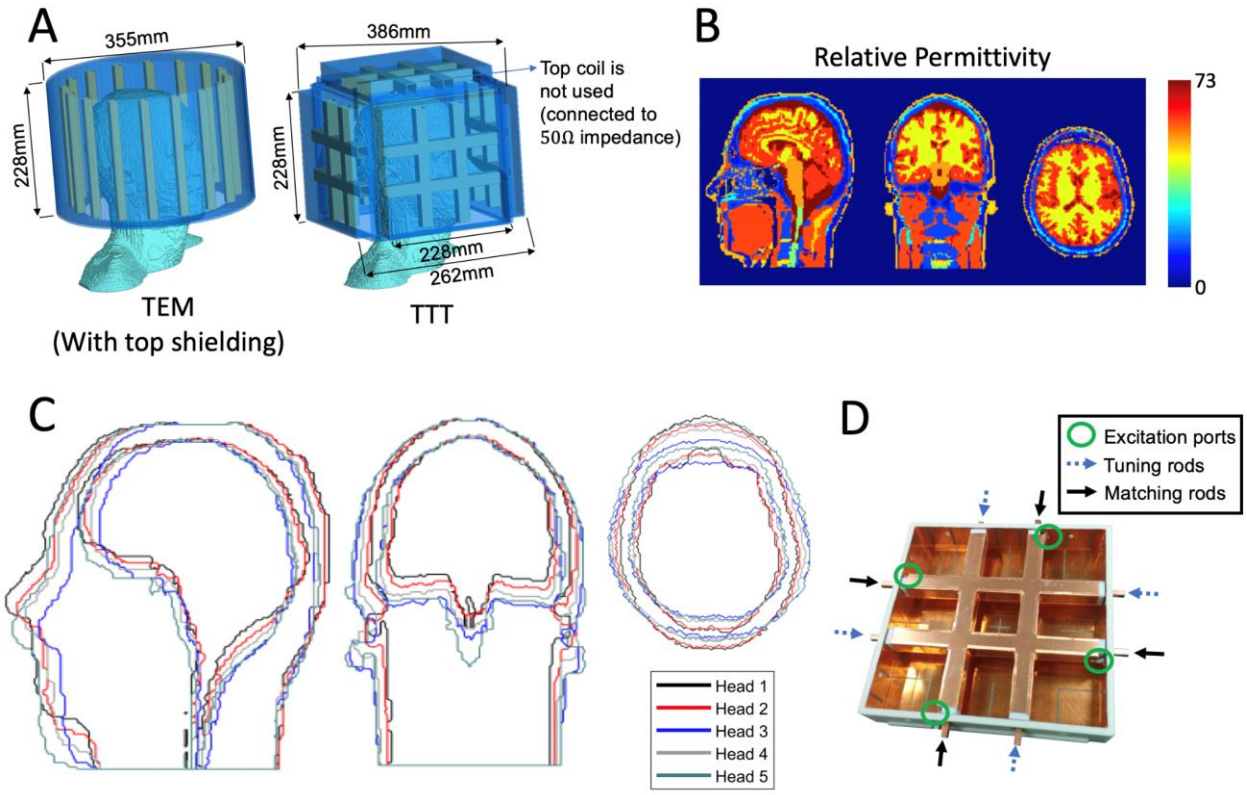

Figure 42: Coil designs and head models. In A, the TEM and TTT coil designs with anatomically detailed head model as the load; in B, the relative permittivity maps of one of the head models; In C, the superimposed outlines of all the head models; In D, a constructed TTT coil side.

The TEM coil [23] consists of an array of transmission line elements (coaxial) with a cylindrical and end cap RF shielding. While, birdcage coils are popular with body imaging with larger ROI at 1.5T and 3T field intensities, TEM coils with 8, 16, and 24 transmission line elements have been built and tested for imaging the head at 7T [169]. It is worth noting that the commercial birdcage head coil (Nova Medical, Wilmington, MA, USA) is currently the most used RF coil for head imaging at 7T. Detailed analysis of a 16-element TEM design have shown good homogeneity in neuroimaging and its ability to tune over a broader frequency range, make it suitable for high

field applications such as 7T. The four coaxial Tx ports of the 16-element TEM coil are tuned to 297.2 MHz by adjusting the inner rod length pushed inside the outer strut for all the coil elements. This coil, like 7T TTT design described earlier, is 228 mm long, it has an outer diameter of 355 mm and an inner diameter of 279 mm.

Both the TTT and the TEM Tx coils use double-layered copper sheets (each layer is 4um 38.1 gram/m^2 Cu thickness with 0.254 mm dielectric between the layers.) For the TTT coil, the tic tac toe square-shaped array is made from (19.05 mm)^2 Polycarbonate dielectric with (6.35 mm)^2 inner opening for the inner rods. For the TEM coil, the elements are made of cylindrical-shaped (diameter = 12.7 mm) Teflon dielectric with inner opening (diameter = 6.35 mm) for the inner rods. The TEM elements are concentric with 279 mm diameter.

The excitation channels of each coil are combined using Wilkinson power dividers (2-, 4-, and 8- ways), with phase cables to implement particular RF shim phases (more on that in the "Excitation Strategy" section.)

A.2.2 RF Modeling and Simulations

Five anatomically detailed head models varying in shape/volume and weight were used to analyze the transmit coil characteristics of the TEM and TTT transmit coils at 7T using FDTD simulations. The anatomically detailed head models H1-5 were created from Duke male model of the Virtual family head models [170] (age: 34, height: 1.74 m, weight: 70 kg, body mass index (BMI): 23.1 kg/m^2). The 22 tissue volumes, identified by its constitutive properties - conductivity and dielectric constant (σ, ε_r) - of the different head models. The head models were created by morphing the base model (H2) to produce models (H1-5) that varied in shape/eccentricity and volume and weights.

The maximum variation in the mass was 14% and changes in shape was quantified by eccentricity of the head. The eccentricity measure is defined as the ratio of major to minor axis at the eyebrow level and was obtained from the cross-sectional area and perimeter estimate at the same location. This was achieved using the DIP library [171] where the method1 by Proffitt et.al. [172] used different weights for inclined boundary lines, and the method2 by Vossepoel et.al. [173] used corner correction to obtain the perimeter of odd shapes. Eccentricity of heads varied from circular (eccentricity ~ 1) to elliptical (eccentricity ~ 1.4). Figure 42(C) shows the contours of the different head models (axial, coronal and sagittal boundary of brains and heads) used in the FDTD simulations. The relative permittivity map is also shown in Figure 42(B).

The perimeter of the models and their eccentricity when compared with those measured on the 4 volunteers indicate the shape and volume of heads used in the RF simulations represent a comprehensive sample of an adult population who might undergo an MRI [174].

FDTD models of the TTT and TEM head coils i.e. the coil geometry: including the coaxial transmission lines, RF shielding, anatomically detailed head models and the terminating (perfectly matched layers) PML [175] are shown in Fig. 1(A). The 3-dimensional computational domains with isotropic resolution of ~1.6mm was constructed by setting the constitutive properties to that of the RF coil (comprising of Rexolite or, Teflon, or Copper) or to the different tissues of the anatomically detailed head models. The coil model has a true transmission line model for the excitation elements with accurate modeling capability of the coil's input impedance and coupling [61, 63, 167, 176].

The numerical models of the coils were tuned to Larmor frequency of 7T (297 MHz) using head model (H2) by adjusting the gap between the inner coaxial elements of the TTT and TEM elements and the modeling of the excitation source(s) while observing the scattering (S) matrix of

the true transmission line model. The same tuning configuration applied on H2 is utilized for all other head models without re-tuning/matching for each individual head model.

Note that the full wave 3D FDTD models of the TTT and the TEM coils and the generic framework of validating experiment with simulation studies of the transmit field, input impedance and coupling between coil elements have been performed and validated in earlier studies [61, 167, 176].

A.2.3 Excitation Strategy

The fields (electric and B_1^+) associated with the individual ports of each coil are combined using: 1) quadrature (TEM) and pseudo-quadrature (TTT) excitation, and 2) RF shimming (optimized excitation using phase-only or amplitude-and-phase excitation) for both the TEM and TTT coils. The RF shimming aims at achieving the lowest combination of the coefficient of variation (CV) and maximum to minimum (max/min) inside the region of interest (ROI) for all 5 head models. The ROI is the volume encapsulating the whole head above and including the temporal lobes and cerebellum while excluding the ears and the nasal cavity. The minimization of the CV and max/min inside the ROI is achieved by constraining the mean transmit B_1^+ field intensity to 11.74 μT, which results in 180^o flip angle with 1 ms square pulse, using a ~ 4.4 kW RF amplifier capacity (45% power loss from a standard 8 kW RF amplifier to the coil ports). Note that the phase-only shim cases (quadrature and phase-only arrangements) can be readily implemented in the combined mode of the MRI system without the need for parallel transmission mode.

RF absorption in the whole head quantified by SAR (W/Kg) averaged over any 10g of tissue was obtained for a continuous wave with mean transmit B_1^+ field intensity of 2μT in the ROI.

A.2.4 Experimental Measurements

This study was approved by the University of Pittsburgh's Institutional Review Board (IRB PRO17030036) and involved four volunteers with approved written consent. The individuals have given a written informed consent to publish the details in this manuscript. Bench measurements were performed using a calibrated network analyzer (E5062A and 87050E multiport test set; Agilent Technologies Inc., CA, USA) together with an 85032B S-parameter test set. The Smith Chart measurements of different excitation ports of the TTT and TEM coils were recorded for the four volunteers (without re-tuning/re-matching of the excitation ports between different heads). Thus, both measurements in-vivo on the four volunteers, and with the five head models (H1-5) in FDTD simulations, were obtained without re-tuning/re-matching of the excitation ports.

To achieve the desired phase shifts, the quadrature (for TEM) and pseudo-quadrature (for TTT) cases were implemented by adjusting the lengths of the coaxial cables feeding the coils. Imaging was performed on two volunteers using a 7T scanner (Siemens Medical Solutions, Germany). B_1^+ maps were acquired with a turbo FLASH sequence with the following parameters: number of flip angles = 6, TR = 2.2 sec, TE = 1.4 msec, FOV =220 mm, Matrix = 64x64, slice thickness = 3.2 mm and bandwidth = 510 Hz/pixel. The images from the six measurements of the B_1^+ map sequence was summed and used to create a brain mask. FSL's brain extraction tool (BET) [177] was used to create a brain mask (bet -m -f 0.4 options were used). The created brain masks

were visually inspected and corrected manually using ITK SNAP tool [178] in the regions where automatic segmentation of the brain failed.

A.3 Results

A.3.1 Input Impedance of Loaded Coils

Figure 43(A) and Figure 43(B) show the FDTD calculated reflection coefficients (Sxx) and input impedances of different excitation ports in the TEM and TTT coils and the input impedances (real $\pm$ imaginary Ω) with the five head models (H1-H5). The displayed two (for the TEM coil) and four (for the TTT coil) reflection spectrums are representative of all the excitation channels of the TEM and TTT coils. Figure 43(C) also shows the bench measurements (using network analyzer) of the input impedances (Smith Chart) associated with two representative channels of the TEM and TTT coils on four different volunteers.

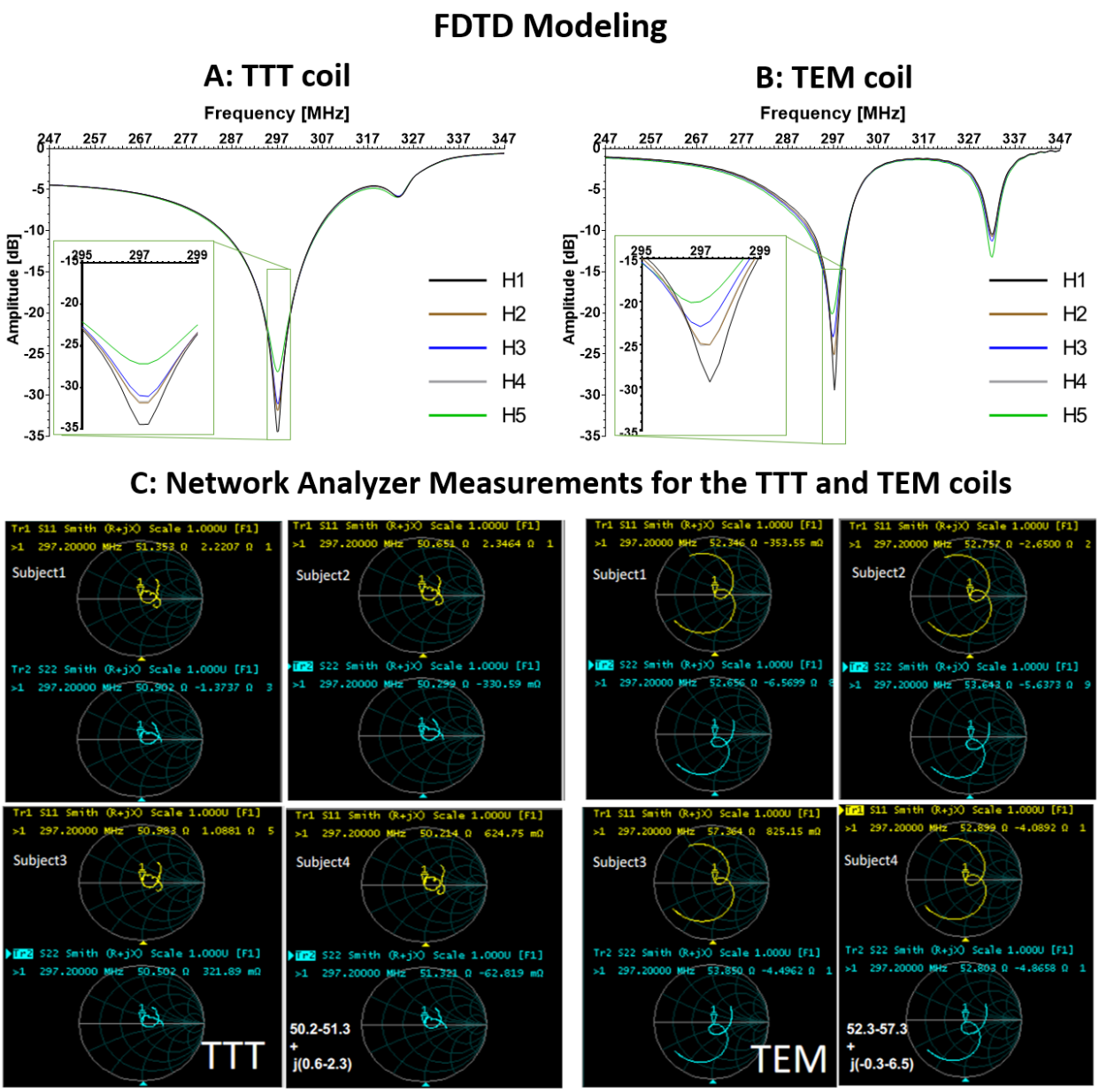

Figure 43: Simulations and Network Analyzer Measurements. In A), reflection (Sxx) of a representative port of the TTT coil with the 5 different head models (H1-5) using full wave FDTD simulations. The maximum variation (between different head models) in input impedance amongst all the ports using the five different head models (80 cases) was 2.3%; In B), reflection of a representative port of the TEM coil with the 5 different head models using FDTD simulations. The maximum variation (between different head models) in input impedance amongst all the ports using the five different head models (20 cases) is 3.5%. There was no re-tuning or re-matching for any of the ports in both coils; the coils were tuned/matched to H2 and used in

the same configuration for the other head models; In C), experimental impedance measurements (Smith Chart) for 2 representative ports for the TTT & TEM coils. Both coils showed consistent (< 5% variation) input impedance among all four volunteers.

The numerical (across five different head models) and experimental (across four volunteers) results show that the reflection coefficient (Sxx) and input impedance values of both the TTT and TEM coils did not change appreciably. In terms of the input impedance, the maximum variation (between the five different head models) was 3.5% for the TEM coil (twenty cases represented by four excitation channels and five different head models) and 2.3% for TTT coil (eighty cases represented by sixteen excitation channels and five different head models.) The maximum variation measured with the network analyzer was 5%.

A.3.2 Numerical and In-vivo B_1^+ Field Distributions

Transmit B_1^+ field distributions across the five head models are shown for different excitation strategies (Figs 3-6 and Table 2). We compared three different excitation sets including quadrature, and variable amplitude-and-phase, and phase-only cases for the two coils. Due to the consistent tuning, and matching for both coils across different subjects, the coils were not re-tuned/matched in the simulations (five head models).

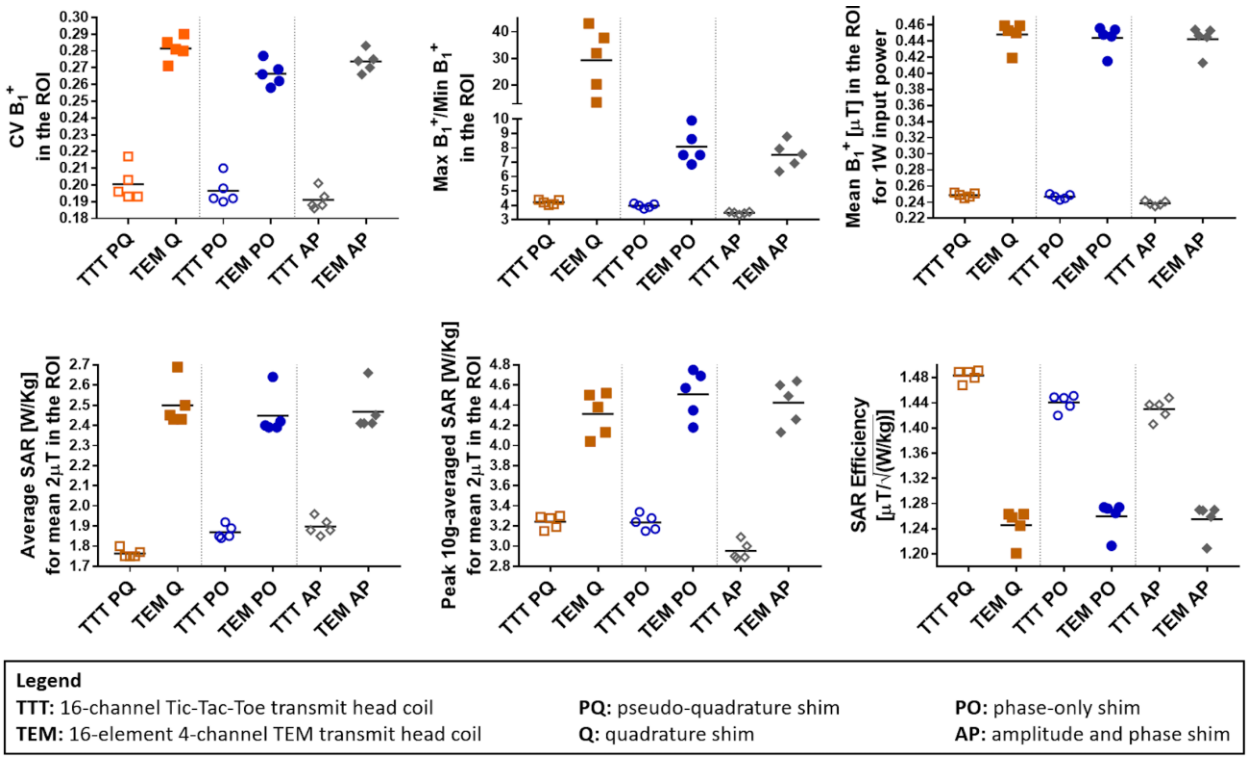

Figure 44: Performance comparison of the TTT and TEM coils with three different RF shimming techniques: quadrature/pseudo-quadrature excitation, phase-only RF shimming (per coil, one RF shim set is applied to all 5 head models), and amplitude-and-phase RF shimming (per coil, one RF shim set is applied to all 5 head models). FDTD Calculated stats for the B_1^+ field and SAR for the five head models described in Fig. 1 and Table 2 are shown. B_1^+ field homogeneity is quantified in terms of max/min, and CV in the region of interest (ROI). The ROI is defined as the whole head above and including the cerebellum and excluding the nasal cavities for all head models. The SAR performance is presented in terms of relationships between peak local SAR, average SAR, and B_1^+ field. Each line in each subfigure represents the mean value.

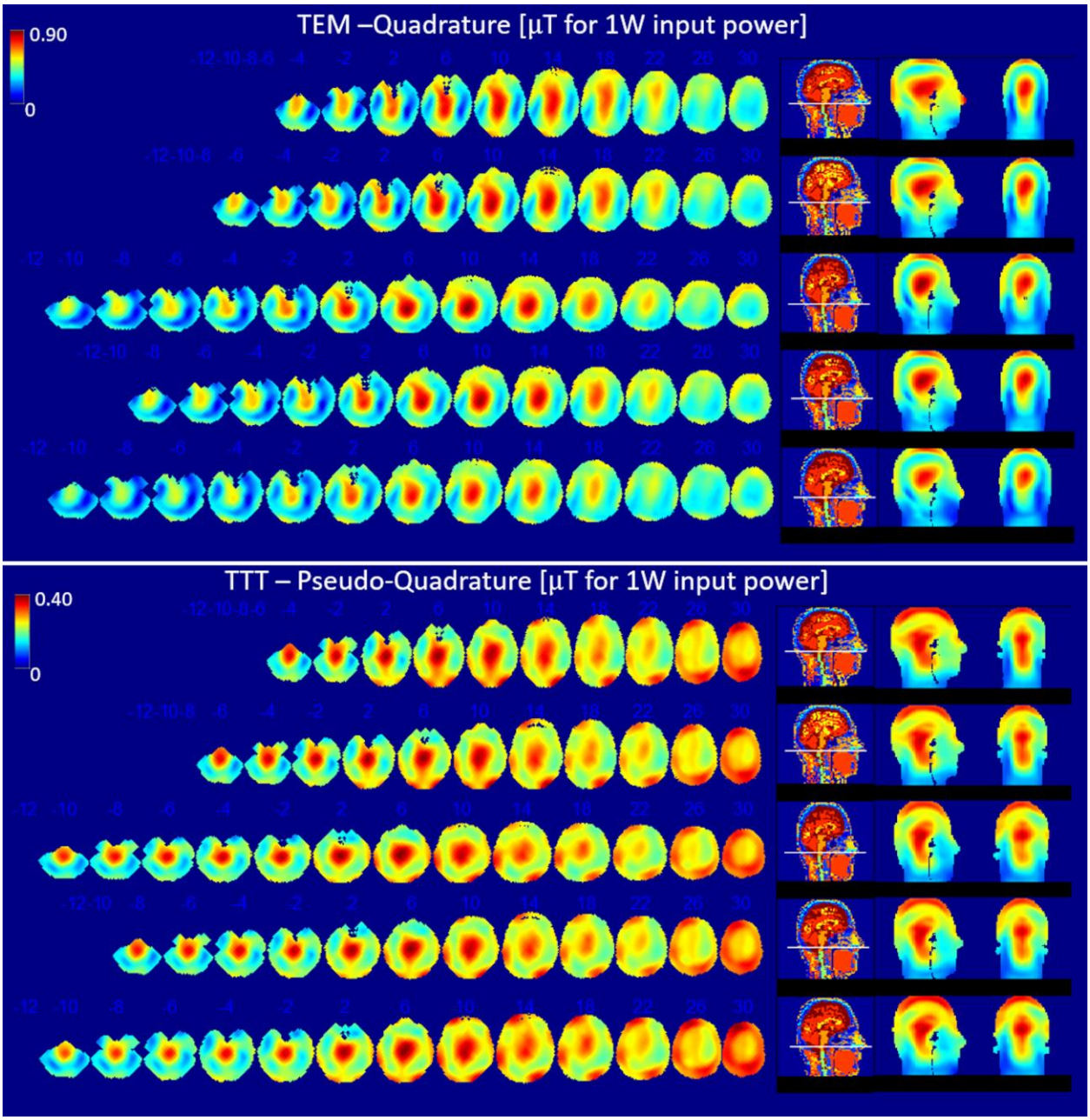

Figure 45: B_1^+ distribution for quadrature (TEM) and pseudo-quadrature (TTT) excitation: FDTD simulation data matching stats and conditions described in Table 2 and Fig. 3. Axial slices were plotted with steps of 6.35 or 12.7 mm, slice numbers are indicated on top of each slice for instance (30, 26, ... 2, -2, -4, …-10 etc.). Slices are plotted every 6.35 mm from (slice -10) through (slice 2) to capture the end of the cerebellum in the head model, and every 12.7 mm subsequently to visualize the B_1^+ field distribution for the five head models.

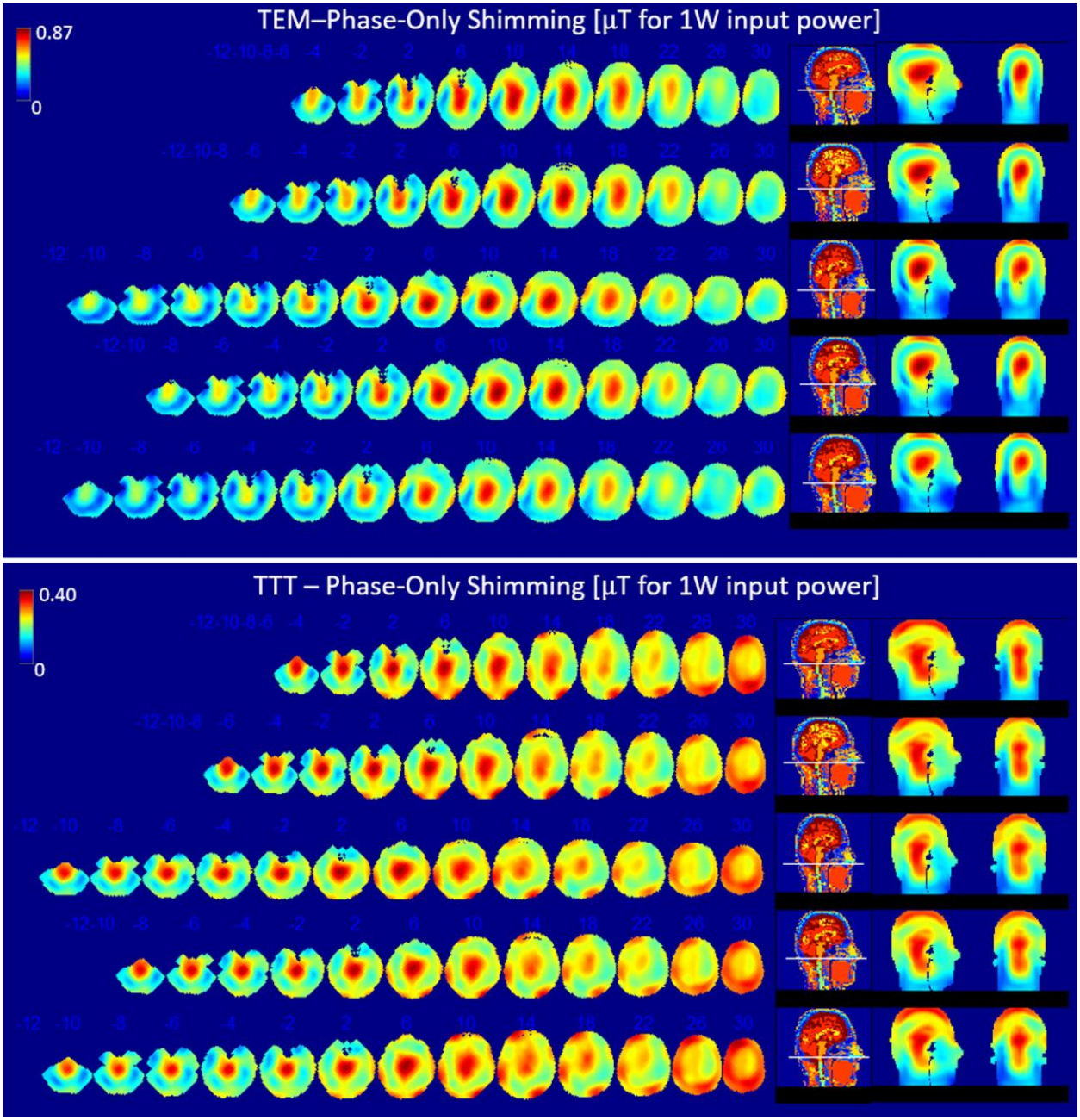

Figure 46: B_1^+ distribution for phase-only RF shimming: FDTD simulation data matching stats and conditions described in Table 2 and Fig. 3. Description is provided in Figure 45 caption.

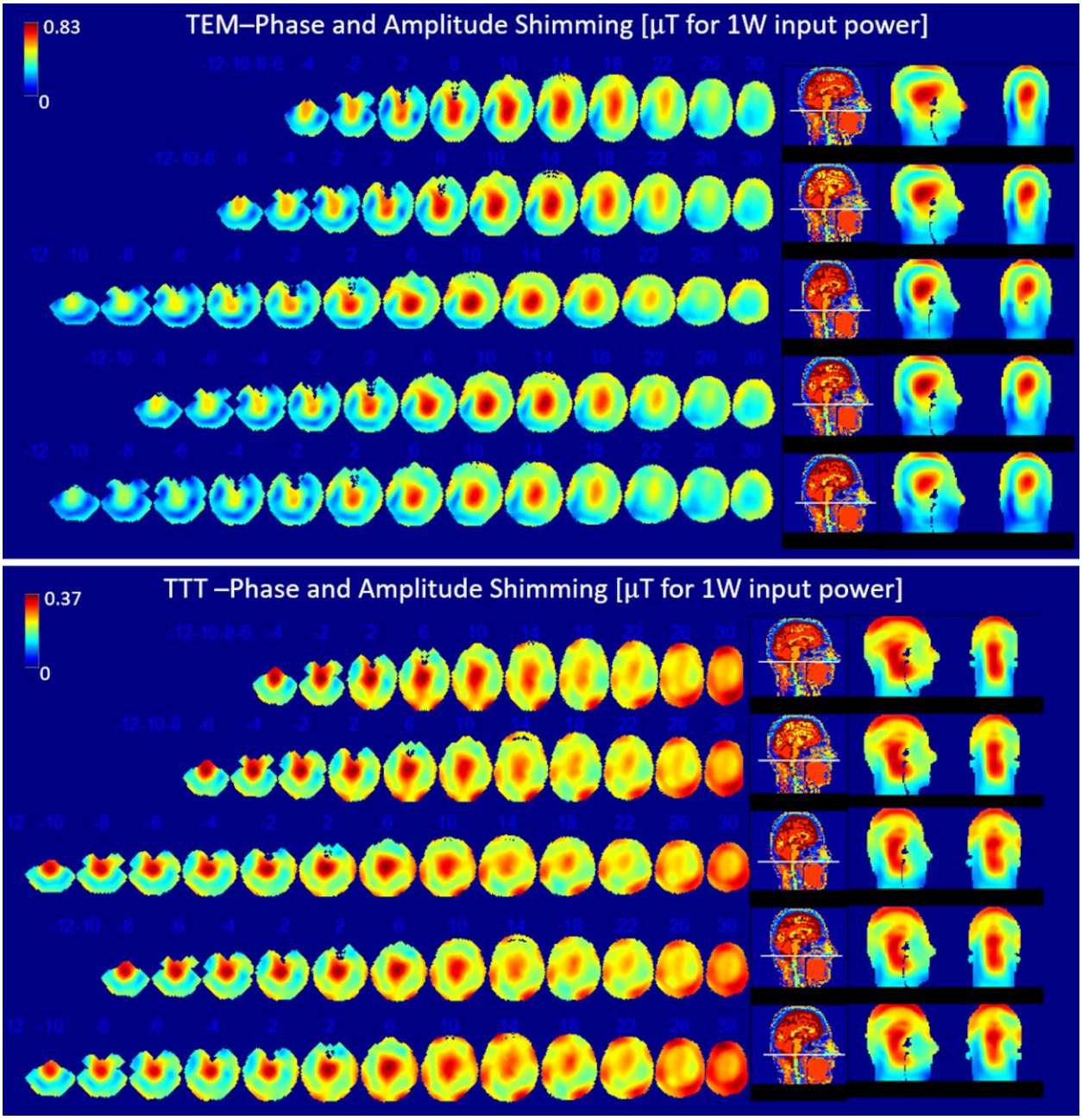

Figure 47: B_1^+ distribution for amplitude-and-phase RF shimming: FDTD simulation data matching stats and conditions described in Table 2 and Fig. 3. Description is provided in Figure 45 caption.

A.3.3 B_1^+ Field Homogeneity

Homogeneity of the B_1^+ field distribution was calculated in terms of maximum over minimum B_1^+ (max/min) and coefficient of variation (CV) which is defined as the standard deviation over mean ($\boldsymbol{\sigma}/\boldsymbol{\mu}$) in the ROI. Figs 4-6 show multiple axial, one coronal, and one sagittal slice of B_1^+ field distribution. Sagittal conductivity maps of the different head models are also plotted with a line indicating the end of cerebellum in each of the five head models. The ROI, where stats were obtained in the five head models (Figure 44 and Table 2), includes the whole head above and including the cerebellum and excluding the nasal cavities and ears. The ROI volume of the different head models are different as indicated by the different axial slice number # which determines the end of cerebellum for each head model.

Figure 44 and Table 2 provides details of the following stats. In terms of quadrature (TEM) and pseudo-quadrature (TTT) excitation, the average (across H1-5) CV and max/min values for the B_1^+ field distribution are 20/28 % and 4.21/29.32 respectively for the TTT/TEM Coils. In terms of phase-only RF shimming, the average (across H1-5) CV and max/min values for the B_1^+ field distribution are 20/27 % and 3.97/7.94 respectively for the TTT/TEM Coils. In terms of amplitude-and-phase RF shimming, the average (across H1-5) CV and max/min values for the B_1^+ field distribution are 19/27% and 3.47/7.51 respectively for the TTT/TEM coils.

Table 3: Statistics for TEM and TTT Coils for Quadrature and Pseudo-quadrature Excitation, Phase-only RF Shimming, and Phase-and-amplitude RF Shimming. The Average Head Model Mass is 4.56kg (with 14% Maximum Variation Among the Models), the Average Brain Volume is 1.51 L (with 15% Maximum Variation), and the Average Eccentricity (Major/Minor Axes) is 1.25 (with 37% Maximum Variation)

		B_1^+ Uniformity				Mean B_1^+ in the Same Volume (μT) for 1 W Input Power		Peak SAR over Average SAR		Average SAR (W/Kg) for Mean $B_1^+ = 2\mu$T in the Same Volume		Mean B_1^+ in the Same Volume over Sqrt(SAR) ($\mu T\sqrt{Kg}/\sqrt{W}$)	
		Maximum Intensity over Minimum Intensity in Whole Head above & Including Cerebellum and Excluding Nasal Cavity (Max B_1^+/Min B_1^+)		Standard Deviation over Mean in the Same Volume (CV)									
		TTT	TEM	TTT	TEM	TTT	TEM	TTT	TEM	TTT	TEM	TTT	TEM
Quadrature (TEM) and Pseudo-Quadrature (TTT)	Avg.	4.21	29.32	0.201	0.281	0.249	0.448	3.24	4.31	1.76	2.50	0.483	1.246
	Max Variation (%)	9.28	216.99	12.44	6.98	3.01	9.40	4.94	12.05	3.15	10.54	1.56	5.14
Phase-only RF Shimming	Avg.	3.97	7.94	0.197	0.266	0.247	0.451	3.24	4.58	1.87	2.40	1.441	1.271
	Max Variation (%)	10.29	44.54	10.47	7.46	2.99	9.83	6.26	13.60	4.48	10.37	2.21	5.06
Phase-and-Amplitude RF Shimming	Avg.	3.47	7.51	0.193	0.273	0.240	0.443	2.95	4.42	1.90	2.47	1.430	1.267
	Max Variation (%)	6.13	38.2	8.22	6.26	2.90	9.89	7.5	12.5	6.06	10.37	2.98	5.06

In terms of CV, the TTT design provides 40%/35%/41% average (across H1-H5) percentage improvement over the TEM design for quadrature/phase-only/amplitude-and-phase-excitation strategies. In terms of max/min, the TTT design provides 597%/99%/116% average (across H1-H5) percentage improvement over the TEM design for quadrature/phase-only/amplitude-and-phase excitation strategies.

A.3.4 B_1^+ Field vs. Input Power and B_1^+ Field vs. SAR

We evaluated B_1^+ field efficiency based on SAR as well as input power. Table 2 provides relevant statistical details. In terms of quadrature (TEM) and pseudo-quadrature (TTT) excitation, the average (across H1-5) mean B_1^+ field intensity for 1 W input power and mean B_1^+ field intensity (in ROI) for 1 W average SAR ($\mu T\sqrt{Kg}/\sqrt{W}$)) (in whole head volume) are 0.25/0.45 [$\mu T/\sqrt{W}$] and 1.48/1.25 [$\mu T\sqrt{Kg}/\sqrt{W}$], respectively for the TTT/TEM Coils. Therefore, the TTT design has ~44% lower average B_1^+ intensity for 1W input power and ~18% higher average B_1^+ for 1 W/kg average SAR for this case. In terms of phase-only RF shimming, the average (across H1-5) mean B_1^+ field intensity for 1 W input power and mean B_1^+ field intensity for 1 W average SAR are 0.25/0.45 [$\mu T/\sqrt{W}$] and 1.44/1.27 [$\mu T\sqrt{Kg}/\sqrt{W}$], respectively for the TTT/TEM coils. Thus, the TTT design presents ~44% lower B_1^+ for 1W input power and ~13% higher B_1^+ for 1 W/kg average SAR for the phase-only cases. In terms of amplitude and phase RF shimming, the average (across H1-5) mean B_1^+ field intensity for 1 W input power and mean B_1^+ field intensity for 1 W average SAR are 0.24/0.44 [$\mu T/\sqrt{W}$] and 1.43/1.27 [$\mu T\sqrt{Kg}/\sqrt{W}$] respectively for the TTT/TEM coils.

Therefore, the TTT presents ~45% lower B_1^+ for 1W input power and ~13% higher B_1^+ for 1 W/kg average SAR for the phase-and-amplitude RF shimming.

A.3.5 In-vivo B_1^+ Field Measurements and Simulated SAR

Consistent with the RF simulations, in-vivo measurements of transmit B_1^+ field distribution are shown in Figure 48 for the quadrature (TEM) and high flip angle pseudo-quadrature (TTT) excitation cases. The calculated CV for the TTT/TEM coils are ~21%/26% and ~20%/25% respectively for the two subjects (note that the utilized phases/cable lengths were the same for both subjects). Lack of sufficient B_1^+ field intensity in parts of the temporal lobe and cerebellum by the TEM coil makes measurement and use of max/min criterion inaccurate, and therefore it was not measured.

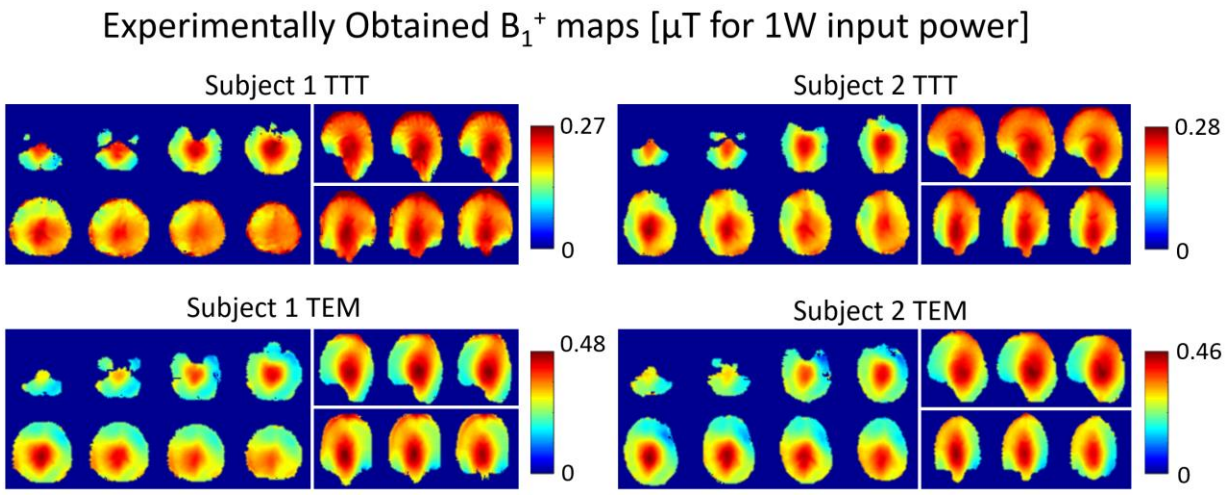

Figure 48: Experimentally obtained B_1^+ maps in two volunteers using the TEM and TTT coils. The color scale ranges from 0 to the maximum B_1^+ for each subject.

SAR distributions across the five head models are shown for the three different excitation strategies (Figure 49). We evaluated SAR efficiency based on calculating average SAR (across the whole head volume) for 2 T mean B_1^+ field intensity in ROI. Table 2 and Figure 44 provide details of the following stats. In terms of quadrature (TEM) and pseudo-quadrature (TTT) excitation, the mean (across H1-5) average-SAR values for 2 T mean B_1^+ field intensity in ROI are 1.76/2.5 W/Kg for the TTT/TEM coils. In terms of phase-only RF shimming, the mean (across H1-5) average-SAR values for 2 T mean B_1^+ field intensity in ROI are 1.87/2.4 W/Kg respectively for the TTT/TEM coils. In terms of amplitude-and-phase RF shimming, the mean (across H1-5) average-SAR values for 2 T mean B_1^+ field intensity in ROI are 1.9/2.47 W/Kg respectively for the TTT/TEM coils.

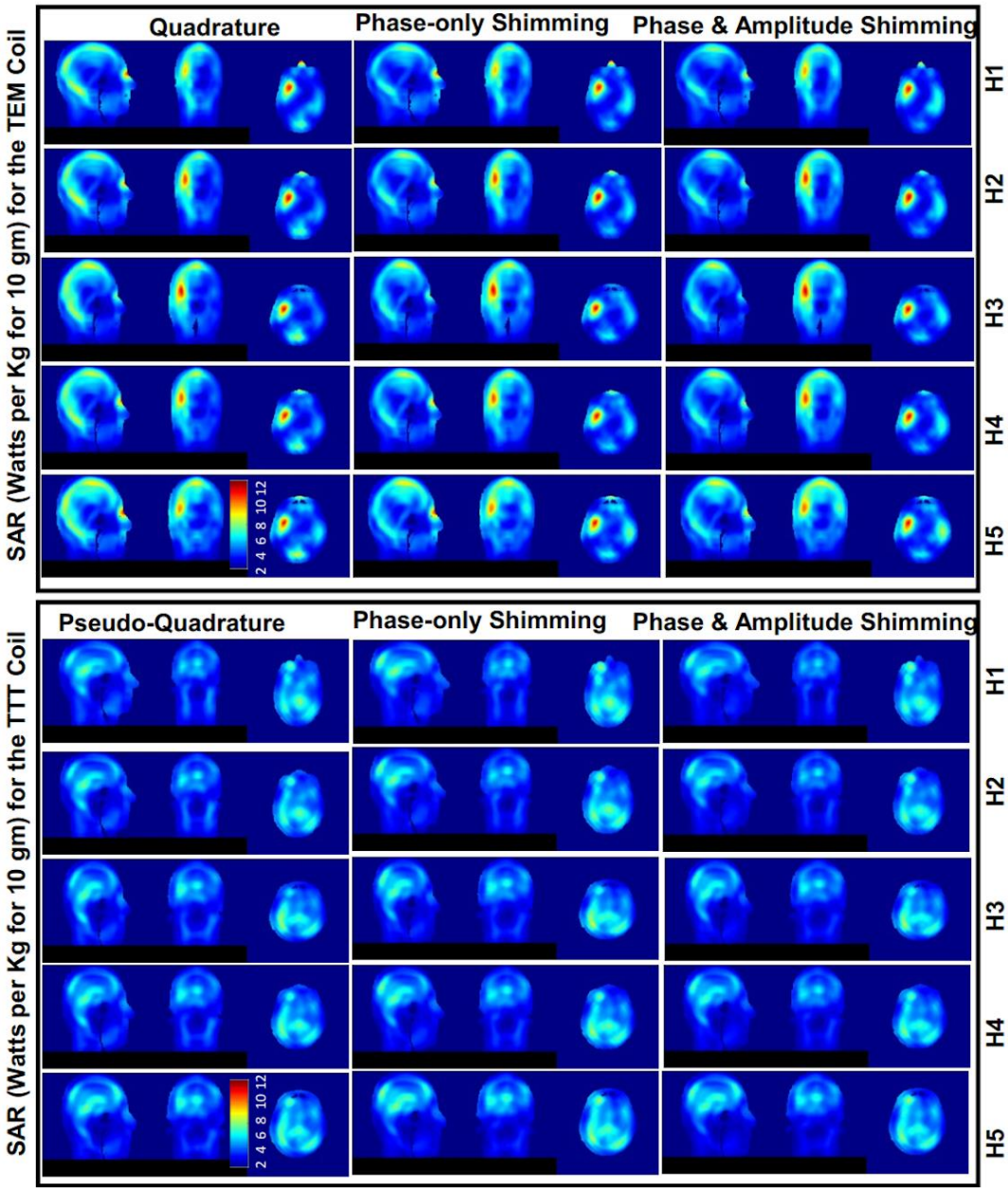

Figure 49: SAR (W/Kg for 10 g) distribution for 2μT mean B_1^+ in the ROI in all head models H1-5 in the TEM and TTT coils. Exemplar axial, sagittal, coronal slices of SAR are shown. The distributions are plotted to the same maximum of 12 W/Kg for 10 g. The SAR is plotted for pseudo-quadrature arrangement, phase-only RF shimming (one RF shim set for coil applied on all 5 head models), and amplitude-and-phase RF shimming (one RF shim set for coil applied on all 5 head models). Please see Figs 2-6 and Table 2 for the conditions under which the SAR distributions are plotted.

In terms of average-SAR values for continuous 2 T mean B_1^+ field intensity in ROI, the TTT design provides 30%/22%/23% lower average (across H1-H5) values when compared to the TEM design for quadrature/phase-only/amplitude-and-phase excitation strategies.

We evaluated SAR distribution based on calculating local SAR (W/Kg for 10 g) to average SAR (W/Kg for 10 g) ratio. Table 2 and Fig. 3 provide details of the following stats. In terms of quadrature (TEM) and pseudo-quadrature (TTT) excitation, the mean (across H1-5) local to average SAR ratio are 3.2/4.3 respectively for the TTT/TEM coils. In terms of phase-only RF shimming, the mean (across H1-5) local to average SAR ratio are 3.2/4.6 respectively for the TTT/TEM Coils. In terms of amplitude-and-phase RF shimming, the mean (across H1-5 local to average SAR ratio are 2.9/4.4 respectively for the TTT/TEM Coils. In terms of local SAR to average SAR ratio, the TTT design provides 25%/30%/34% lower average (across H1-H5) values when compared to the TEM design for quadrature/phase-only/amplitude-and-phase excitation strategies.

A.4 Discussion

A.4.1 B_1^+ Field Distribution

The overall results show that transmit B_1^+ field homogeneity measured by CV as well as max/min (maximum B_1^+ over minimum B_1^+ in the ROI) are substantially improved with the TTT coil when compared to the TEM coil. The TTT coil is well suited for exciting cerebellum and brain stem [121] at 7T. That being said, the TEM coil design with its arrangement of multiple

transmission lines aims at providing increased excitation in the middle of the brain [23] as opposed to extended coverage in the peripheries.

Based on our simulations, the central positioning in conjunction with the same back-of-head positioning in XY plane for different head models within the coils is optimal for in-vivo MRI acquisitions for the TEM coil. Prior simulations [179] showed that a slightly shifted position in the XY plane provides moderate better coil performance for the TTT coil. To keep consistency between both coils, this shifted case (with the TTT coil) was not considered in this study.

The load insensitive nature of the TTT coil comes from having strongly coupled elements [19], which decreases the load to coil interactions. Although this comes at a price as its transmit efficiency evaluated as $B_1^+/\sqrt{}$forward power is substantially lower when compared to the TEM coil. That being said, the implementation of the TTT coil has been shown to provide adequate B_1^+ for inversion (180^o flip angle at 1 ms pulse width), and turbo spin echo and other clinical scans requiring inversion with a standard 8 kW RF amplifier [179-182].

A.4.2 SAR

Despite lower ratio of B_1^+ field vs. input power for the TTT design, it provides ~22%-30% lower average (across H1-H5) SAR values (for 2 T mean B_1^+ field intensity in ROI) when compared to the TEM design for quadrature and RF shimming excitation strategies. In terms of local SAR to average SAR ratio which can be the limiting factor in determining the allowed amount of tissue absorption, the TTT design also provides ~25%-34% lower average (across H1-H5) ratios when compared to the TEM for quadrature and RF shimming excitation strategies.

Strategies to overcome patient specific electromagnetic interactions at UHF include; building systems/sequences that are invariant across subjects and using a safety factor in SAR

monitoring [183]. B_1^+ inhomogeneity can potentially be alleviated using a combination of multi-port transmission and/or by adiabatic/hyperbolic or composite pulse sequences that produce constant flip angle independent of transmit field [184]. However, to achieve optimal performance (image quality as well as safe RF levels), one must know how the RF fields produced by coils/arrays behave in every imaged subject prior to an MR experiment. The process of measuring and/or simulating the RF fields and implementing a targeted excitation profile is time consuming and often cannot be performed in real-time with the subject in the scanner. Additionally, the measurements may be inaccurate when signal voids exist in the images and cannot be generalized across subjects when the RF field produced by coil/array is widely varying across different subjects. Therefore, the coil performance across different subjects presented in this study becomes relevant for effective and safe coil use at UHF MRI.

This work shows that both the TEM and TTT coils showed consistent tuning and matching across different subjects/head models. Across 5 head models with brain volumes changing between 1330 and 1740 cc and eccentricity changing between 1.04 and 1.48. That being said, the variation in transmit B_1^+ field and SAR distributions/intensities (across different head models) for the TTT coil was substantially lower than the TEM coil.

Hot-spot changes are predicted to changes in boundary conditions due to significant changes in constitutive properties (σ, ε) and varying resistance to induced currents, in the different heads. These should result in different local SAR for the different heads. Thus, SAR accumulation or hot-spots at eye/nose sinuses, bone-CSF interface, among other regions, are anticipated for different head/(model)s as the boundary regions differ for each of them. For local to average SAR ratio, the maximum variation change is ~5.7%/13% respectively for the TTT/TEM coils.

We studied the B_1^+ field produced in the ROI that encapsulates the whole head above and including the temporal lobes and cerebellum and excludes the nasal cavity, and SAR in the whole head volume. Statistics of the simulated B_1^+ field (efficiency, homogeneity, and consistency), and SAR (intensity and consistency of average and local values) across the 5 head models are tabulated in Table 2, shown in Figure 44, and further elaborated in the Results Section.

A direct comparison between the TTT and TEM coils for the phase-only shim case (directly implementable in the single transmit mode of the 7T scanner) shows the following observations.

1) Both coils present negligible variance of input impedance among different head models/subjects (<5%) in the simulated/measured data.

2) The TTT design shows substantial improvement in the B_1^+ homogeneity and consistency demonstrated in the max/min values of the TTT design (mean max/min = 3.97, maximum variation = 10% between different heads) when compared with that achieved with the TEM design (mean max/min = 7.94, maximum variation = 44%), which represents a significant a) excitation drop in the cerebellum and temporal lobes and b) variation between subjects.

3) The TTT design presents substantial improvement in the B_1^+ homogeneity, as demonstrated in the values of the CV (TTT = 0.20 mean, 10% maximum variation between different heads; TEM = 0.27 mean, 7.5% maximum variation). This is critical for achieving fidelity of the B_1^+ field distribution across the human head. The TTT design has a significant lower B_1^+/power efficiency, with mean B_1^+ = 0.25μT for 1W input power (with 3.0% maximum variation) against 0.45μT (with 10% maximum variation) for the TEM design; however, both coils present enough B_1^+ intensity to have spin inversion with 1ms square pulse and 8kW RF power amplifier including power losses. This could be critical when high peak B_1^+ intensity is needed with limited RF power amplifier capacity.

4) The TTT design has better SAR efficiency, with 1.44 μT/√(W/kg) (maximum variation = 2.2% between different heads) against 1.27 μT/√(W/kg) (maximum variation = 5.1%) for the TEM design. This is critical for high SAR acquisitions (turbo spin echo, FLAIR, DTI, etc...)

5) The TTT design has a lower peak over average SAR ratio (3.24) with maximum variation = ~6.3% between different heads against 4.58 (which is ~41% higher than the TTT value) and maximum variation = ~14% for the TEM design. This is critical for high SAR acquisitions as well as meeting the regulatory limits for local and average SAR. Note that with the FDA-approved single transmit mode 7T systems, the scanner's online SAR calculations do not significantly change between different human heads.

For the TTT coil, the lack of significant variation in terms of B_1^+ distribution/intensity and local/average SAR in different subjects translates to ease in set up (no B_1^+ maps and RF shimming for every subject are necessary). This is very important in a clinical environment when the time to scan a subject is very limited and any retuning or extra acquisition is costly. Moreover, the subject-insensitivity RF performance associated with the TTT design provides greater RF safety assurance measured by consistency in the local and average SAR with different subjects. With narrow tolerance parameters associated with TTT coil, the results also show that numerical simulations can be potentially performed on a representative head model without the need for 1) subject-specific transmit B_1^+ maps measured in-vivo or 2) subject-specific SAR calculations. Finally, the TTT and TEM RF coils can be used in either parallel transmit or in single transmit systems.

A.5 Publications Related to this Appendix

Narayanan Krishnamurthy*, **Tales Santini***, Junghwan Kim, Sossena Wood, Howard Aizenstein, and Tamer S. Ibrahim. *"Computational and Experimental Evaluations of transmission line Based RF Coils at 7T"*. PlosOne, 2019. *equal contribution.

Narayanan Krishnamurthy, Yujuan Zhao, **Tales Santini**, Sossena Wood, Tiejun Zhao, and Tamer Ibrahim. *"Case Studies of 7T RF Shimming using Parallel Tx & Rx System."* International Society for Magnetic Resonance in Medicine, 2015.

Appendix B Imaging with the Tic-Tac-Toe head RF Coil System

This appendix presents a collection of images acquired using the Tic-Tac-Toe RF coil systems. Up to date, the 16-channel Tic-Tac-Toe head coil has been used in more than 750 subjects in patient studies. This appendix also compares the imaging performance of the Tic-Tac-Toe head coil with commercial solutions for 7T MRI and 3T MRI.

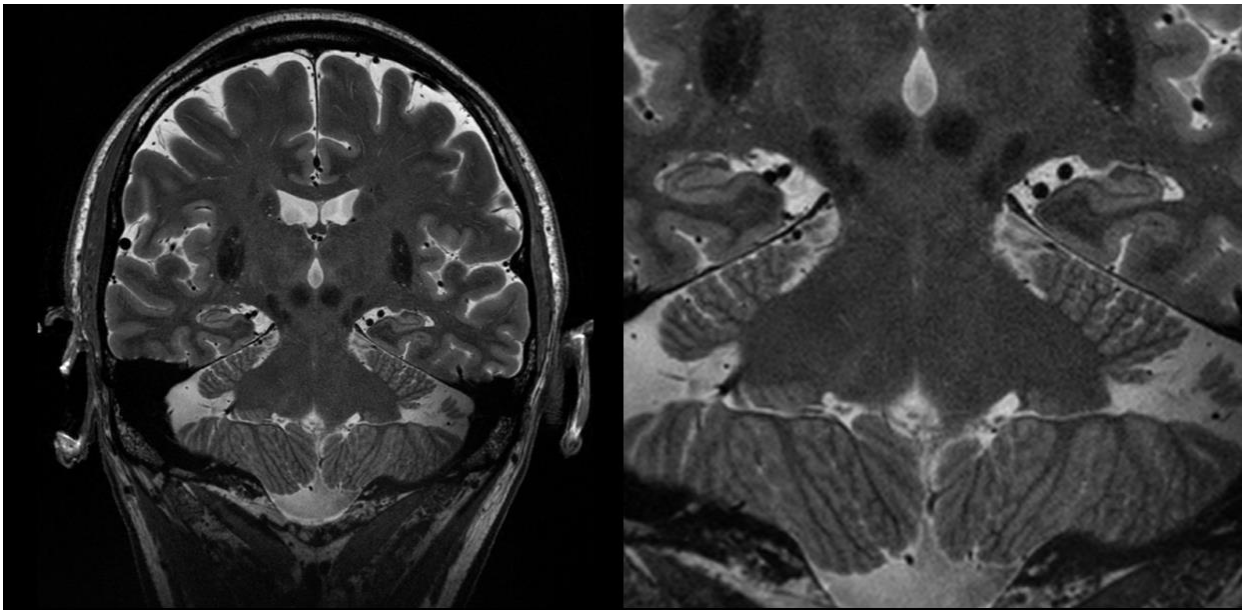

Figure 50: Turbo Spin Echo (TSE) image acquired at 7T, showing the details of the hippocampal structure. The parameters of the image acquisition are: TE/TR = 61/10060ms, resolution 0.375x0.375x1.5, 36 slices acquired perpendicular to the hippocampus, total scan time of 3:53 min

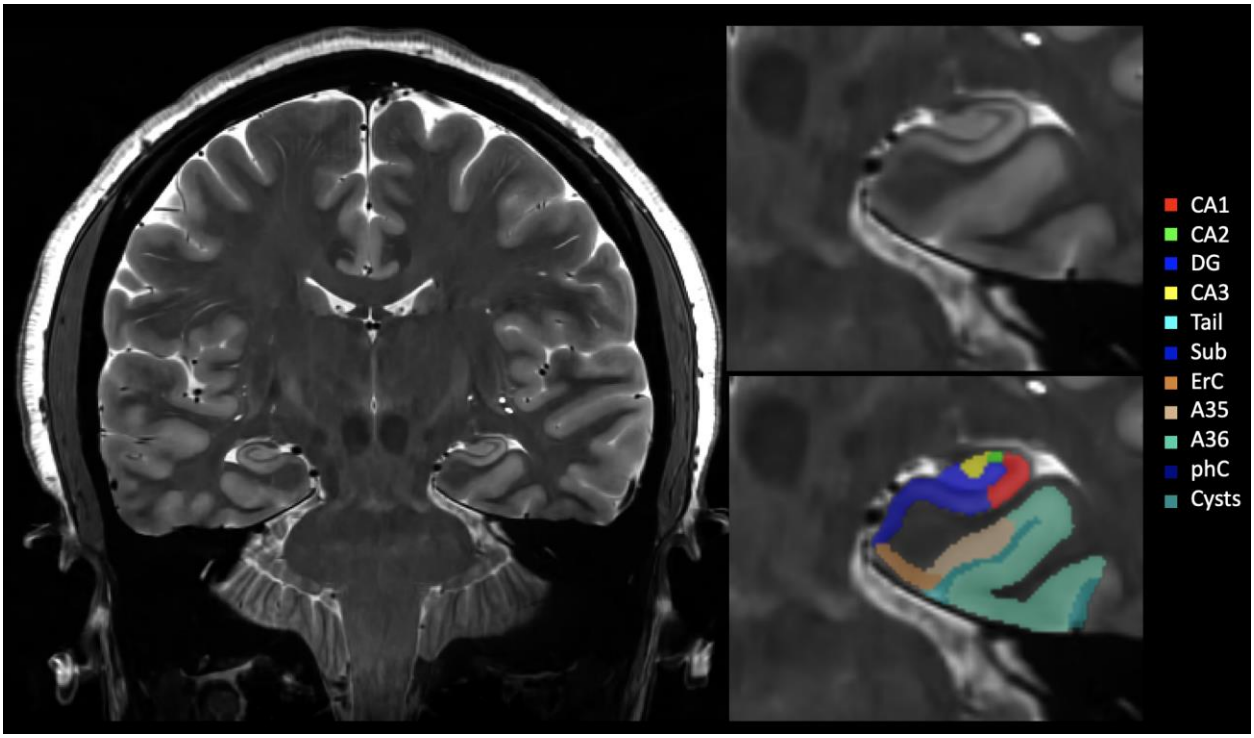

Figure 51: Automatic segmentation of the hippocampal subfields. The TSE image was bias-corrected (using SPM package) and denoised (using variance stabilizing transformation and BM4D algorithm [185]). The segmentation was performed using the ASHS package and a denoised version of the atlas segmented from young adults [186].

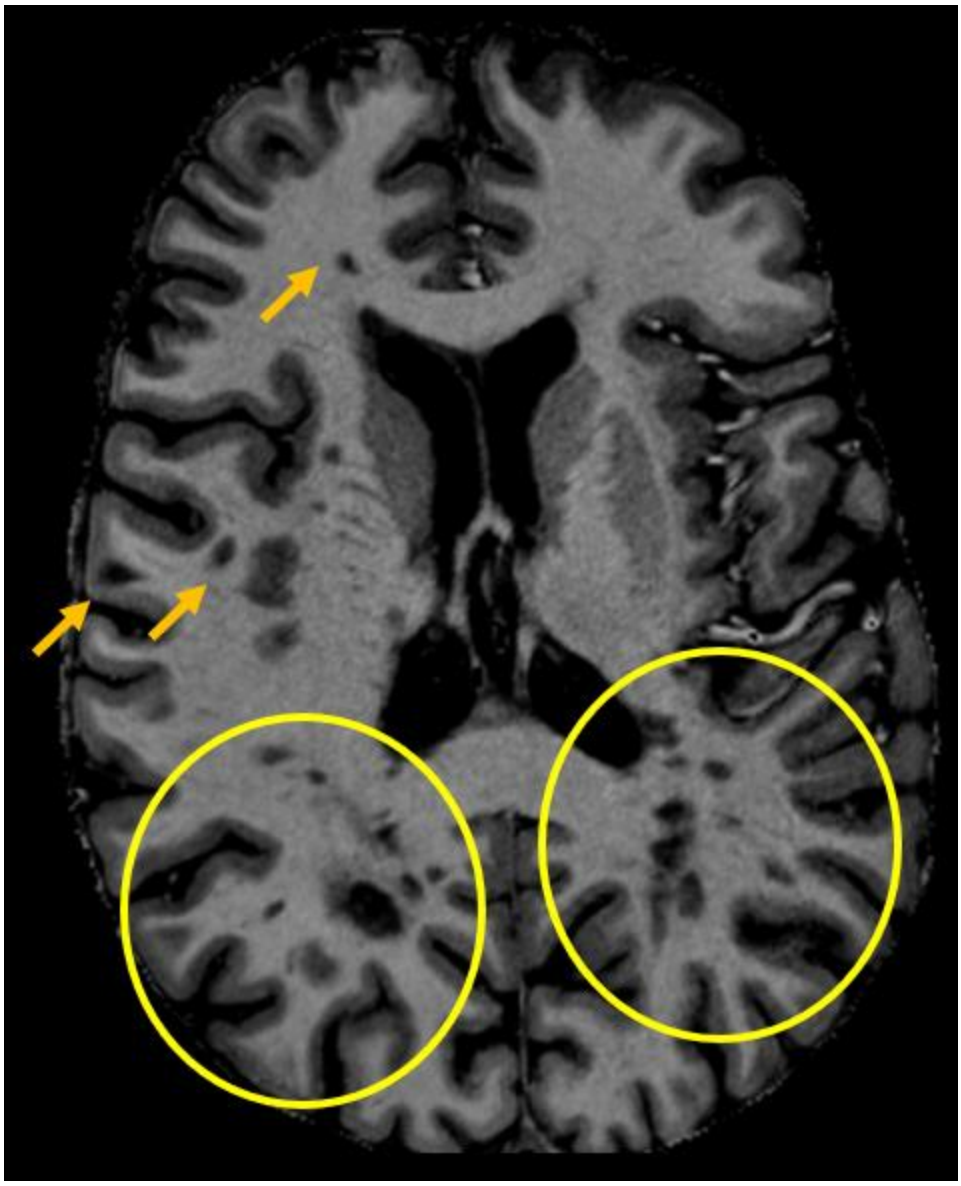

Figure 52: MP2RAGE sequence acquisition showing several lesions in the brain (circles and arrows). The parameters of the sequences are: TE/TI1/TI2/TR = 2.54/800/2500/6000, resolution 0.6mm isotropic, 348 slices, acquisition time of 12:44min

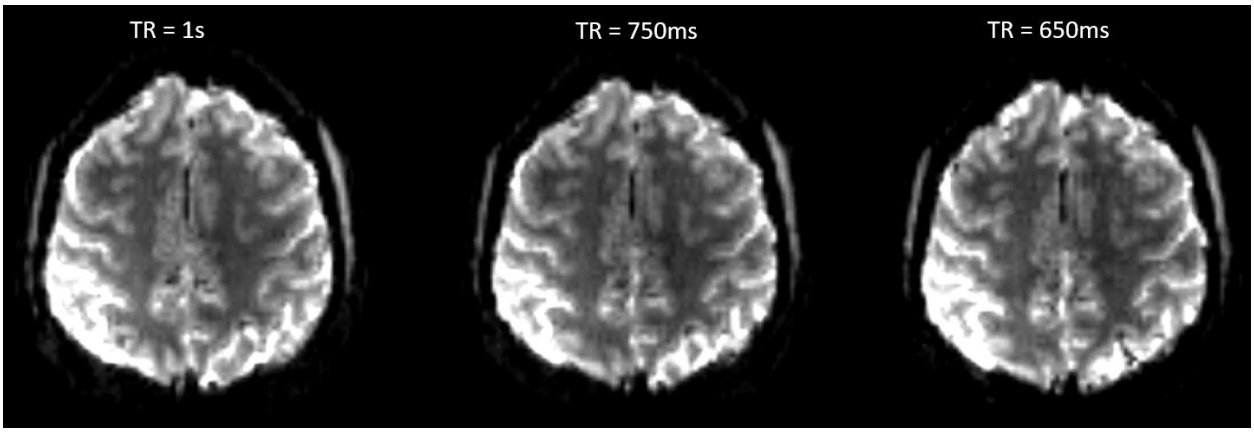

Figure 53: multiband Echo Planar Imaging (EPI) at 7T MRI, showing a sample slice from whole brain acquisition, acquired as fast as 650ms. Minimal differences are observed from the slower acquisitions. The parameters of the MRI sequences are: TE 20ms, resolution 2mm isotropic, 60 slices.

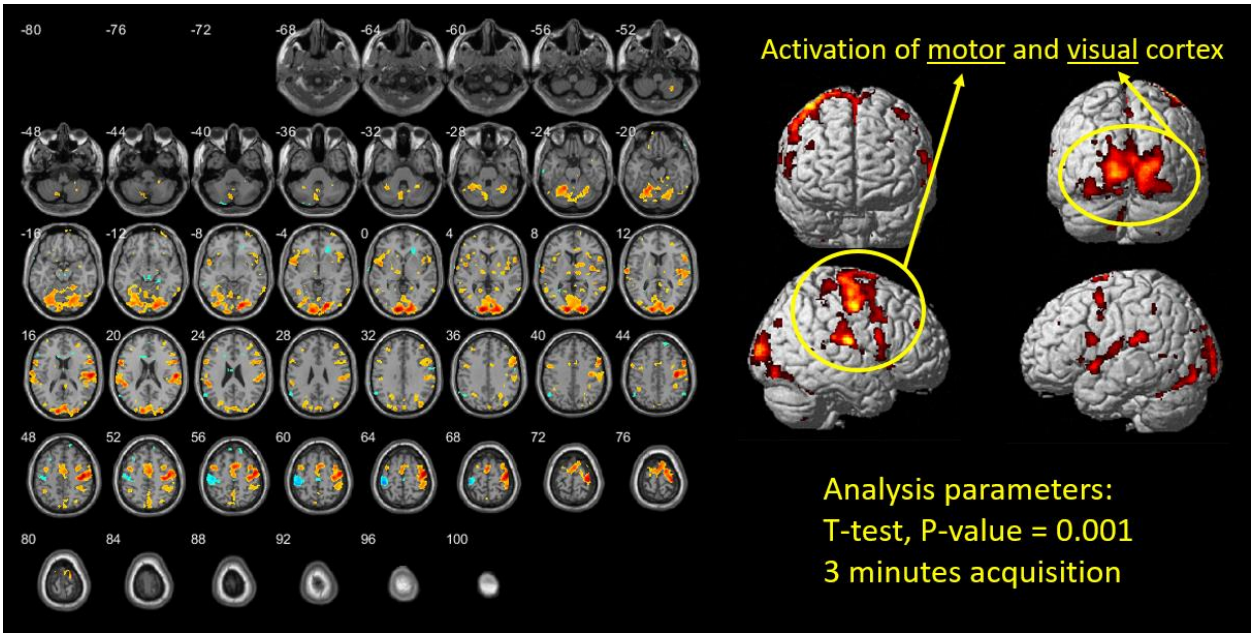

Figure 54: post-processed functional MRI from finger tapping task. The parameters are: TE/TR = 20/2500ms, total acquisition time of 3 minutes (onsets of 20 seconds). There was a strong activation on the motor and visual cortex.

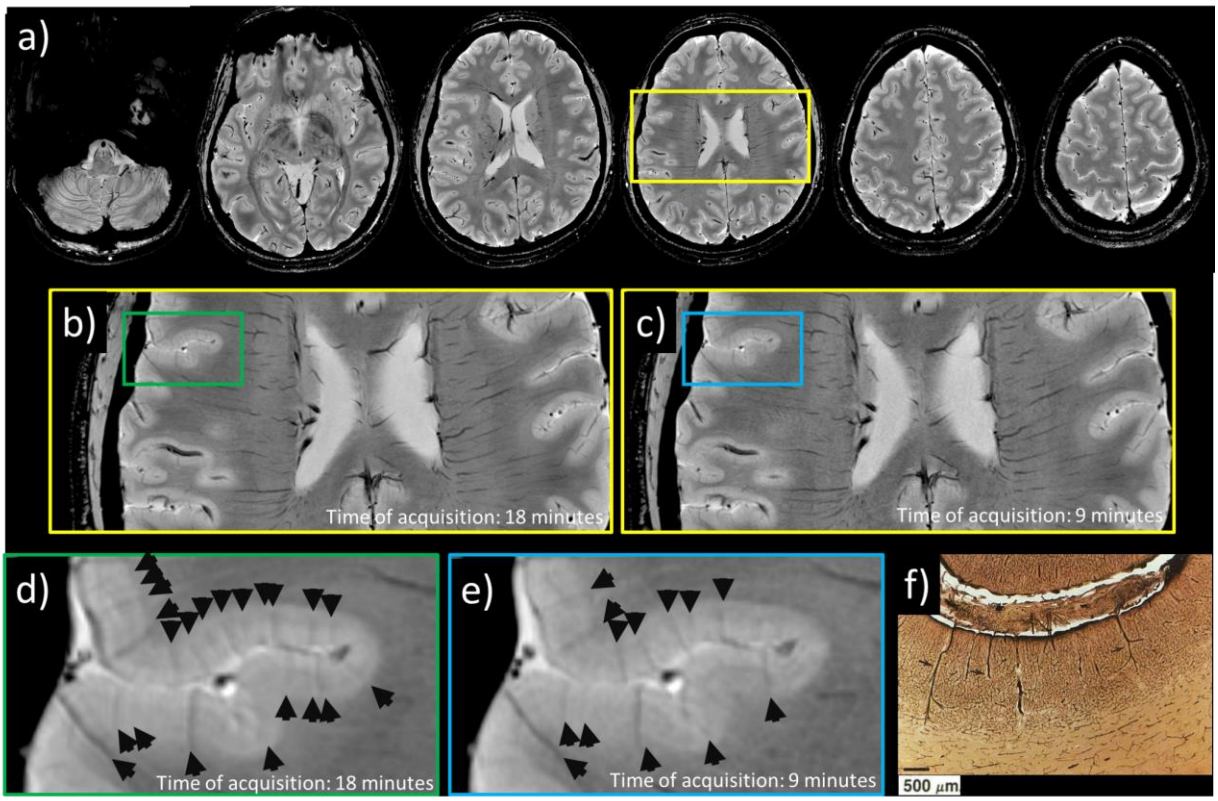

Figure 55: susceptibility weighted imaging (SWI) acquired on a volunteer. The sequence parameters are: TE/TR = 14/1960, Bandwidth = 40Hz/Px. In a), slices from the whole brain acquisition; in b), data showing a sample slice with full acquisition of the k-space (without acceleration); in c) a similar slice acquisition with acceleration factor (GRAPPA) 2; in d) a zoomed version showing cortical microvessels; in e), the zoomed version in similar slice but with acceleration factor 2, which is acquired in half of the scanning time (9 minutes); in f), an histology from the cortical region (Moody et al 1989) showing similar structure as seen in-vivo using high resolution MRI

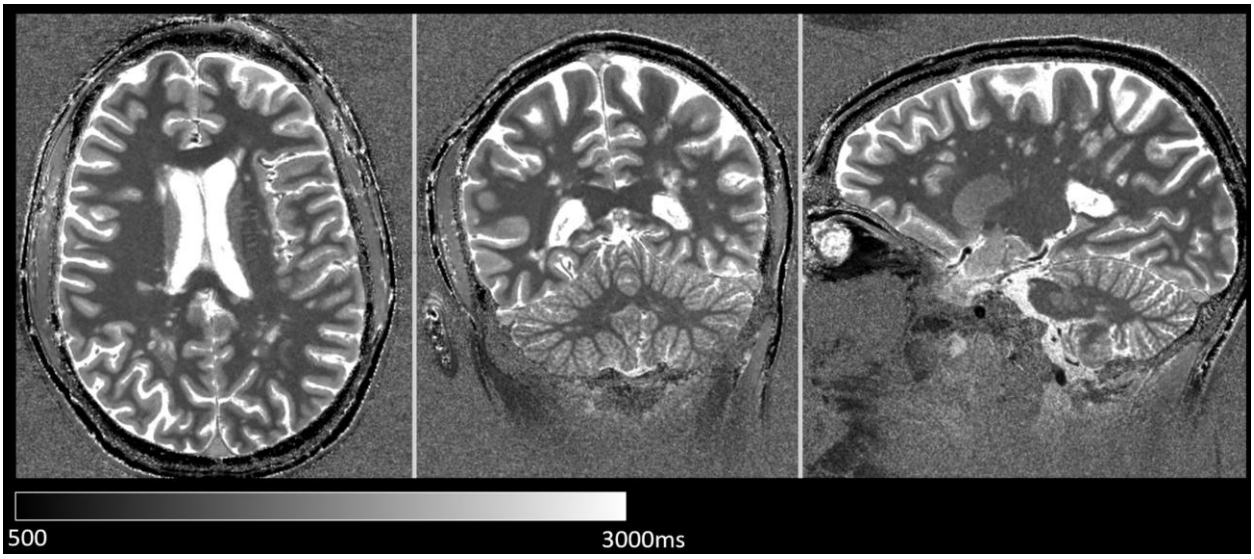

Figure 56: in-vivo T1 maps calculated from the MP2RAGE sequence. From left to right, the axial, coronal, and sagital sample slices of the full brain acquisition. The sequece parameters are: TE/TI1/TI2/TR = 2.54/800/2500/6000ms, resolution 0.55mm isotropic, acquisition time 12:44min.

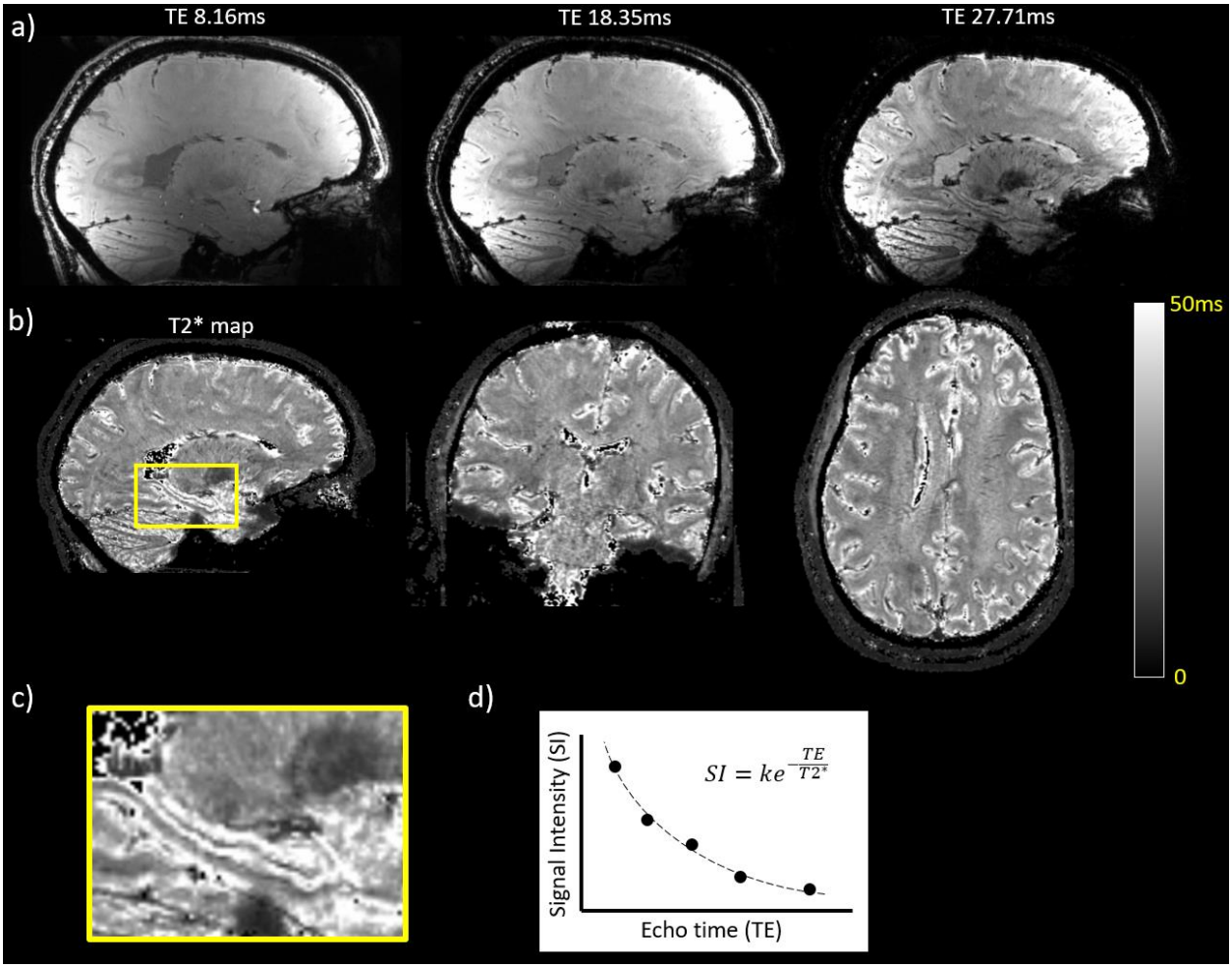

Figure 57: T2* maps calculated from the gradient echo (GRE) image acquisition. In a), 3 different times of echo (TE) of the GRE acquisition; in b), the calculated T2* maps, showing from left to right the sagittal, coronal, and axial sample slices from the whole brain acquisition; in c), an zoomed saggital view showing the details of the hippocampus; in d), an illustration of the signal decay and the equation for calculating of the T2*

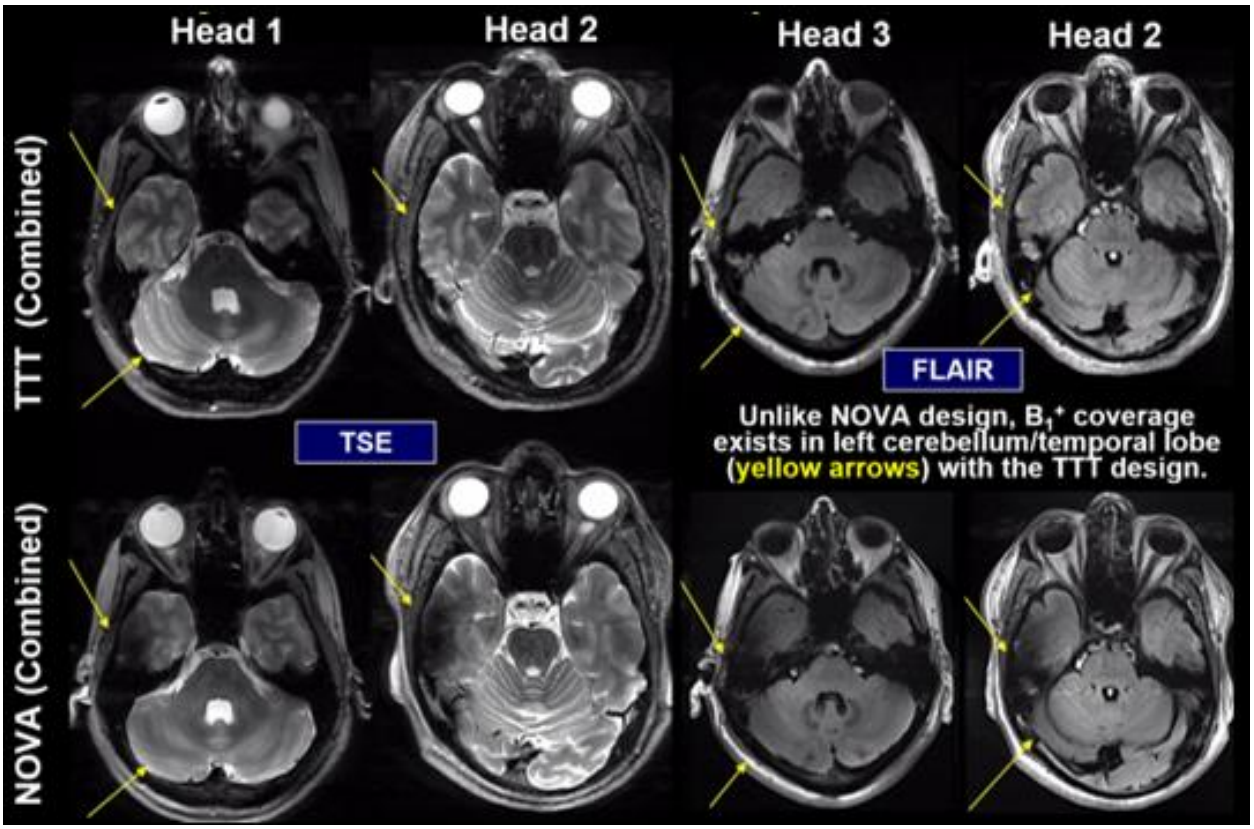

Figure 58: Comparison between the Tic-Tac-Toe heead coil and the 32-channel NOVA coil (available commercially). The Turbo Spin Echo (TSE) and Fluid-attenuated inversion recovery (FLAIR) were used to evaluate the performance of the two coils for high flip-angle sequences. The yellow arrows points at regions of void or low contrast presented by the commercial coil that has been improved with the Tic-Tac-Toe design.

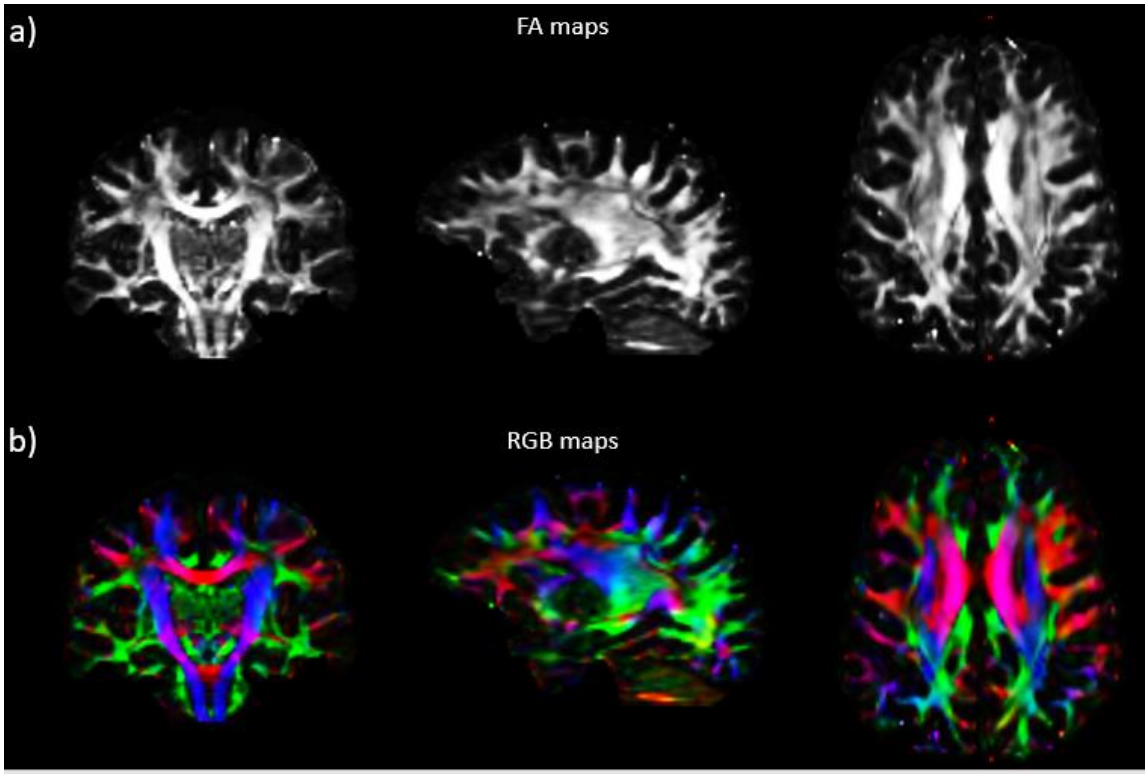

Figure 59: Post processed DTI images acquired in two shells: 750 S/mm^2 and 1500S/ mm^2 at 7T. The other parameters are: TE/TR = 88.2/7750, 100 acquisitions, resolution 1.5mm isotropic. The images were post-processed using the MRtrix Package [187]. In a), the Fractional anisotropy (FA) maps; in b), the colored FA maps.

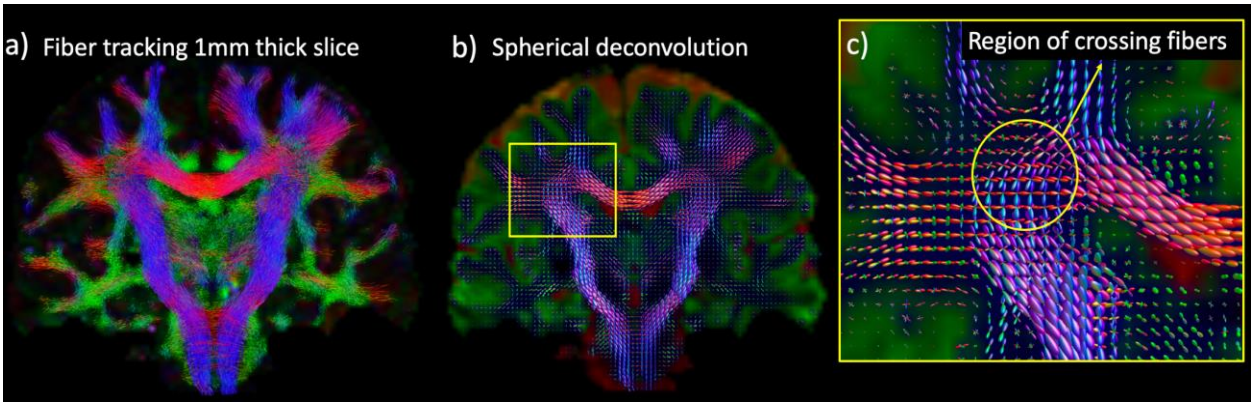

Figure 60: Post-processing techiniques applied to the multishell DTI data (same parameters as Figure 59) and MRtrix packege [187]. In a), the fiber tracking in a 1mm thick coronal slice; in b), the spherical deconvolution in the same slice; in c), a zoomed area of the spherical deconvolution showing a region with cossing fibers.

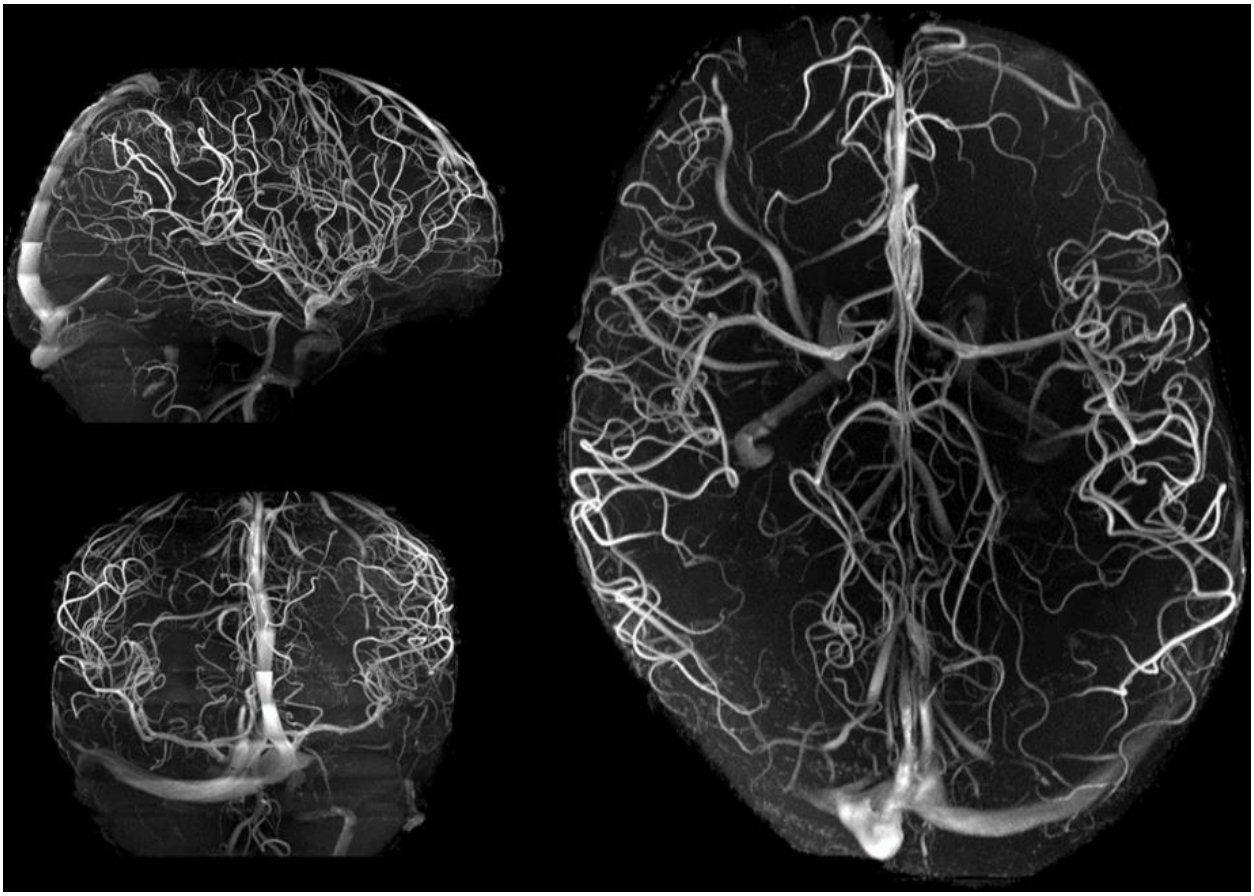

Figure 61: MR angiography, showing the maximum intensity projetion over the time of flight (TOF) sequence without contrast agent at 7T. The paramerters of the sequence are: TE/TR = 4.72/13 ms, resulution 0.32 mm isotropic

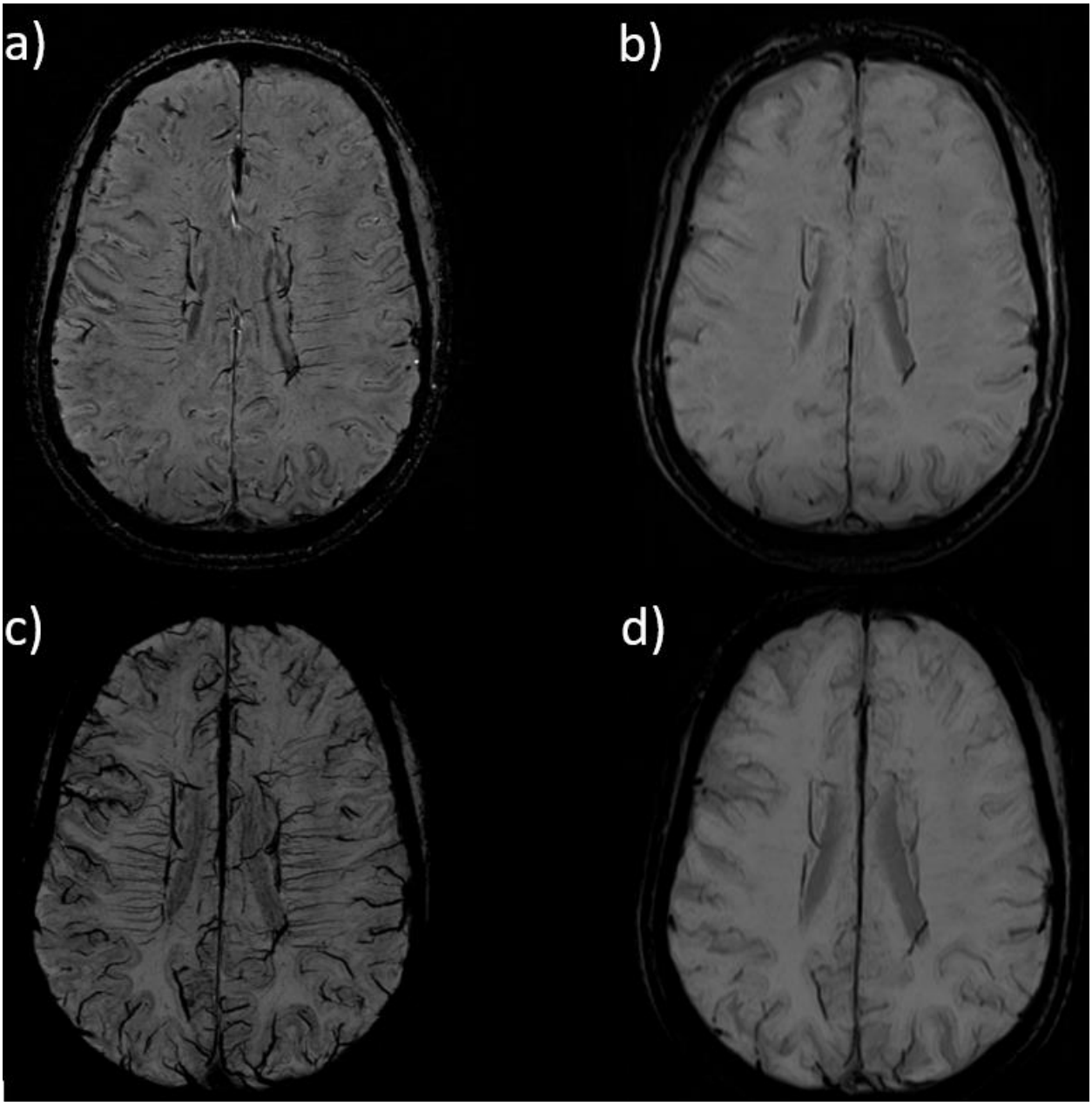

Figure 62: Susceptibility weighted imaging (SWI) comparison between 7T (using the Tic-Tac-Toe head RF system) and 3T MRI in the same subject and similar slice position. In a), the SWI at 7T; in b), the SWI at 3T; in c), minimal intensity projection on the 7T SWI image; in d), minimal intensity projection on the 3T SWI image. The images acquired at 7T showed higher conspicuicy of the vassels. The paramters of the sequences are: 7T 3D SWI, resolution 0.375x0.375x0.75, TE/TR = 8.16/23ms, time of acquisition 8min; 3T 3D SWI, 0.8x0.8x1.6mm, TE/TR = 20/28; time of acquisition 3min.

Bibliography

1. Brown, R.W., et al., *Magnetic Resonance Imaging: Physical Principles and Sequence Design*. 2nd ed. 2014: Wiley-Blackwell.

2. Juras, V., et al., *Comparison of 3T and 7T MRI clinical sequences for ankle imaging.* Eur J Radiol, 2012. **81**(8): p. 1846-50.

3. Boutet, C., et al., *Detection of volume loss in hippocampal layers in Alzheimer's disease using 7 T MRI: a feasibility study.* Neuroimage Clin, 2014. **5**: p. 341-8.

4. Eapen, M., et al., *Using high-resolution MR imaging at 7T to evaluate the anatomy of the midbrain dopaminergic system.* AJNR Am J Neuroradiol, 2011. **32**(4): p. 688-94.

5. van Veluw, S.J., et al., *In vivo detection of cerebral cortical microinfarcts with high-resolution 7T MRI.* J Cereb Blood Flow Metab, 2013. **33**(3): p. 322-9.

6. Pierre-Marie Robitaille, L.B., *Ultra High Field Magnetic Resonance Imaging*. 2006: Springer US.

7. Vaughan, J.T., et al., *7T vs. 4T: RF power, homogeneity, and signal-to-noise comparison in head images.* Magn Reson Med, 2001. **46**(1): p. 24-30.

8. Ibrahim, T.S. and L. Tang, *Insight into RF power requirements and B1 field homogeneity for human MRI via rigorous FDTD approach.* Journal of magnetic resonance imaging, 2007. **25**(6): p. 1235-47.

9. Trattnig, S., et al., *Clinical applications at ultrahigh field (7 T). Where does it make the difference?* NMR Biomed, 2015.

10. Kraff, O., et al., *MRI at 7 Tesla and above: demonstrated and potential capabilities.* J Magn Reson Imaging, 2015. **41**(1): p. 13-33.

11. Ibrahim, T. and L. Tang, *A Whole-Body 7 Tesla RF Excitation Scheme with Much Improved 1 B+ Field Homogeneity and Local/Global SARs over Quadrature Excitation.* Proceedings of the 15th Annual Meeting of ISMRM, 2007: p. 1013.

12. Ibrahim, T.S., *A Numerical Analysis of Radio-Frequency Power Requirements in Magnetic Resonance Imaging Experiment.* IEEE Transactions on Microwave Theory and Techniques, 2004. **52**(8): p. 1999-2003.

13. Moser, E., et al., *7-T MR--from research to clinical applications?* NMR Biomed, 2012. **25**(5): p. 695-716.

14. Marques, J.P. and D.G. Norris, *How to choose the right MR sequence for your research question at 7 T and above?* Neuroimage, 2017.

15. van der Zwaag, W., et al., *Recent applications of UHF-MRI in the study of human brain function and structure: a review.* NMR Biomed, 2015.

16. Kraff, O. and H.H. Quick, *7T: Physics, safety, and potential clinical applications.* J Magn Reson Imaging, 2017.

17. Abraham, R. and T.S. Ibrahim, *Proposed radiofrequency phased-array excitation scheme for homogenous and localized 7-Tesla whole-body imaging based on full-wave numerical simulations.* Magnetic resonance in Medicine, 2007. **57**(2): p. 235-242.

18. Adriany, G., et al., *Transmit and receive transmission line arrays for 7 Tesla parallel imaging.* Magnetic resonance in medicine, 2005. **53**(2): p. 434-45.

19. Ibrahim, T.S., et al., *Tic Tac Toe: Highly-Coupled, Load Insensitive Tx/Rx Array and a Quadrature Coil Without Lumped Capacitors.* ISMRM, 0438, 2008.

20. Ibrahim T, S.T., Raval S, Krishnamurthy N, Wood S, Kim J, Zhao Y, Wu X, Yacoub E, Aizenstein H, Zhao T. *Towards Homogenous 7T Neuro Imaging: Findings and Comparisons between 7T TTT and NOVA RF Coil Systems*. in *In Proc. of the 25th International Society of Magnetic Resonance in Medicine Annual Meeting*. 2017. Honolulu, Hawaii, USA.

21. Blamire, A.M., *The technology of MRI--the next 10 years?* Br J Radiol, 2008. **81**(968): p. 601-17.

22. Balchandani, P. and T.P. Naidich, *Ultra-High-Field MR Neuroimaging.* AJNR Am J Neuroradiol, 2015. **36**(7): p. 1204-15.

23. Vaughan, J.T., et al., *High frequency volume coils for clinical NMR imaging and spectroscopy.* Magnetic Resonance in Medicine, 1994. **32**(2): p. 206-218.

24. Rietsch, S.H., et al., *Parallel transmit capability of various RF transmit elements and arrays at 7T MRI.* Magn Reson Med, 2017.

25. Kim, J., et al., *Development of a 7 T RF coil system for breast imaging.* NMR Biomed, 2016.

26. Kim, J., et al., *Experimental and numerical analysis of B1+ field and SAR with a new transmit array design for 7T breast MRI.* J Magn Reson, 2016. **269**: p. 55-64.

27. Y. Zhao, N.K., S. Wood, T. Zhao, S. B. Raval, and T. S. Ibrahim. *3D Eigenmodes Optimizations for 3D Imaging at 7T*. in *The 23nd International Society of Magnetic Resonance in Medicine Annual Meeting*. 2015. Toronto, Canada.

28. Zhao, Y., et al., *Dual optimization method of radiofrequency and quasistatic field simulations for reduction of eddy currents generated on 7T radiofrequency coil shielding.* Magnetic Resonance in Medicine, 2014.

29. Y, Z., et al. *Simultaneous Excitation of Distinct Electromagnetic Modes Using a Tx Array.* in *ISMRM*. 2013. Salt Lake City, US.

30. TS, I., et al. *20-To-8 Channel Tx Array with 32-Channel Adjustable Receive-Only Insert for 7T Head Imaging.* in *International Society of Magnetic Resonance in Medicine*. 2013. Salt Lake City, Utah.

31. Ibrahim, T.S., et al. *Tic Tac Toe: Highly-Coupled, Load Insensitive Tx/Rx Array and a Quadrature Coil Without Lumped Capacitors*. in *Intl. Soc. Mag. Reson. Med.* 2008.

32. Santini, T., et al. *64-channel Double-Octagon Tx Head Coil for 7T Imaging*. in *In Proc. of the 25th International Society of Magnetic Resonance in Medicine Annual Meeting*. 2017. Honolulu, Hawaii, USA.

33. Raval, S., et al. *In-vivo (8x4) 32-ch Tx-only Body Array for UHF MR*. in *In Proc. of the 25th International Society of Magnetic Resonance in Medicine Annual Meeting*. 2017. Honolulu, Hawaii, USA.

34. Krishnamurthy, N., et al., *Computational and experimental evaluation of the Tic-Tac-Toe RF coil for 7 Tesla MRI.* PLoS One, 2019. **14**(1): p. e0209663.

35. Santini, T., et al., *A new RF transmit coil for foot and ankle imaging at 7T MRI.* Magn Reson Imaging, 2018. **45**: p. 1-6.

36. Santini, T.K., Junghwan; Wood, Sossena; Krishnamurthy, Naraynan; Raval, Shailesh; Ibrahim, Tamer. *A new RF coil for foot and ankle imaging at 7T MRI*. in *In Proc. of the 25th International Society of Magnetic Resonance in Medicine Annual Meeting*. 2017. Honolulu, Hawaii, USA.

37. Bright, A., *Planning and Positioning in MRI*. 2011: Elsevier Australia.

38. Bangerter, N.K., et al., *Quantitative sodium magnetic resonance imaging of cartilage, muscle, and tendon.* Quant Imaging Med Surg, 2016. **6**(6): p. 699-714.

39. Krug, R., et al., *Imaging of the musculoskeletal system in vivo using ultra-high field magnetic resonance at 7 T.* Invest Radiol, 2009. **44**(9): p. 613-8.

40. Kogan, F., A.P. Fan, and G.E. Gold, *Potential of PET-MRI for imaging of non-oncologic musculoskeletal disease.* Quant Imaging Med Surg, 2016. **6**(6): p. 756-771.

41. Alizai, H., G. Chang, and R.R. Regatte, *MRI of the Musculoskeletal System: Advanced Applications using High and Ultrahigh Field MRI.* Semin Musculoskelet Radiol, 2015. **19**(4): p. 363-74.

42. Teodoro, J.S., et al., *The bile acid chenodeoxycholic acid directly modulates metabolic pathways in white adipose tissue in vitro: insight into how bile acids decrease obesity.* NMR in Biomedicine, 2016. **29**(10): p. 1391-1402.

43. Juras, V., et al., *Histological correlation of 7 T multi-parametric MRI performed in ex-vivo Achilles tendon.* Eur J Radiol, 2013. **82**(5): p. 740-4.

44. Bangerter, N.K., et al., *Quantitative techniques for musculoskeletal MRI at 7 Tesla.* Quant Imaging Med Surg, 2016. **6**(6): p. 715-730.

45. Welsch, G.H., et al., *Magnetic resonance imaging of the knee at 3 and 7 tesla: a comparison using dedicated multi-channel coils and optimised 2D and 3D protocols.* Eur Radiol, 2012. **22**(9): p. 1852-9.

46. Robitaille, P.-M. and L. Berliner, *Ultra high field magnetic resonance imaging*. Vol. 26. 2007: Springer Science & Business Media.

47. Schmitter, S., et al., *Cerebral TOF angiography at 7T: Impact of B1 (+) shimming with a 16-channel transceiver array.* Magn Reson Med, 2014. **71**(3): p. 966-77.

48. Metzger, G.J., et al., *Dynamically applied B1+ shimming solutions for non-contrast enhanced renal angiography at 7.0 Tesla.* Magn Reson Med, 2013. **69**(1): p. 114-26.

49. Deniz, C.M., et al., *Maximum efficiency radiofrequency shimming: Theory and initial application for hip imaging at 7 tesla.* Magn Reson Med, 2013. **69**(5): p. 1379-88.

50. Wright, A.C., et al., *Helmholtz-pair transmit coil with integrated receive array for high-resolution MRI of trabecular bone in the distal tibia at 7T.* J Magn Reson, 2011. **210**(1): p. 113-22.

51. Orzada, S., et al., *Open design eight-channel transmit/receive coil for high-resolution and real-time ankle imaging at 7 T.* Med Phys, 2011. **38**(3): p. 1162-7.

52. Trattnig, S., et al., *Advanced MR methods at ultra-high field (7 Tesla) for clinical musculoskeletal applications.* Eur Radiol, 2012. **22**(11): p. 2338-46.

53. Juras, V., et al., *Regional variations of T(2)* in healthy and pathologic achilles tendon in vivo at 7 Tesla: preliminary results.* Magn Reson Med, 2012. **68**(5): p. 1607-13.

54. Domayer, S.E., et al., *Cartilage repair of the ankle: first results of T2 mapping at 7.0 T after microfracture and matrix associated autologous cartilage transplantation.* Osteoarthritis Cartilage, 2012. **20**(8): p. 829-36.

55. Deligianni, X., et al., *High-resolution Fourier-encoded sub-millisecond echo time musculoskeletal imaging at 3 Tesla and 7 Tesla.* Magn Reson Med, 2013. **70**(5): p. 1434-9.

56. Han, M., et al., *Depiction of achilles tendon microstructure in vivo using high-resolution 3-dimensional ultrashort echo-time magnetic resonance imaging at 7 T.* Invest Radiol, 2014. **49**(5): p. 339-45.

57. Theysohn, J.M., et al., *MRI of the ankle joint in healthy non-athletes and in marathon runners: image quality issues at 7.0 T compared to 1.5 T.* Skeletal Radiol, 2013. **42**(2): p. 261-7.

58. Krug, R., et al., *In vivo ultra-high-field magnetic resonance imaging of trabecular bone microarchitecture at 7 T.* J Magn Reson Imaging, 2008. **27**(4): p. 854-9.

59. Banerjee, S., et al., *Rapid in vivo musculoskeletal MR with parallel imaging at 7T.* Magn Reson Med, 2008. **59**(3): p. 655-60.

60. Zhao, Y., et al., *Implanted miniaturized antenna for brain computer interface applications: analysis and design.* PLoS One, 2014. **9**(7): p. e103945.

61. Tang, L., Y.K. Hue, and T.S. Ibrahim, *Studies of RF Shimming Techniques with Minimization of RF Power Deposition and Their Associated Temperature Changes.* Concepts Magn Reson Part B Magn Reson Eng, 2011. **39B**(1): p. 11-25.

62. Krishnamurthy, N., T. Zhao, and T.S. Ibrahim, *Effects of receive-only inserts on specific absorption rate, B1 (+) field, and Tx coil performance.* J Magn Reson Imaging, 2014. **39**(2): p. 475-84.

63. Ibrahim, T.S., Y.K. Hue, and L. Tang, *Understanding and manipulating the RF fields at high field MRI.* Nmr in Biomedicine, 2009. **22**(9): p. 927-936.

64. Wood, S., et al., *Design and fabrication of a realistic anthropomorphic heterogeneous head phantom for MR purposes.* PloS one, 2017. **12**(8).

65. Raval, S.B., et al., *Ultra-high-field RF coil development for evaluating upper extremity imaging applications.* NMR Biomed, 2016. **29**(12): p. 1768-1779.

66. Fiedler, T.M., M.E. Ladd, and A.K. Bitz, *SAR Simulations & Safety.* Neuroimage, 2017.

67. Tropp, J., *Image brightening in samples of high dielectric constant.* J Magn Reson, 2004. **167**(1): p. 12-24.

68. Ibrahim, T.S., et al., *In-depth study of the electromagnetics of ultrahigh-field MRI.* Nmr in Biomedicine, 2007. **20**(1): p. 58-68.

69. Röschmann, P., *Radiofrequency penetration and absorption in the human body: Limitations to high-field whole-body nuclear magnetic resonance imaging.* Medical physics, 1987. **14**(6): p. 922-931.

70. Vaughan, J.T., et al., *Whole-body imaging at 7T: preliminary results.* Magnetic resonance in Medicine, 2009. **61**(1): p. 244-248.

71. Eichfelder, G. and M. Gebhardt, *Local specific absorption rate control for parallel transmission by virtual observation points.* Magn Reson Med, 2011. **66**(5): p. 1468-76.

72. Lattanzi, R. and D.K. Sodickson, *Ideal current patterns yielding optimal signal-to-noise ratio and specific absorption rate in magnetic resonance imaging: Computational methods and physical insights.* Magnetic Resonance in Medicine, 2012. **68**(1): p. 286-304.

73. Ibrahim, T., et al. *20-To-8 Channel Tx Array with 32-Channel Adjustable Receive-Only Insert for 7T Head Imaging.* in *International Society of Magnetic Resonance in Medicine*. 2013. Salt Lake City, Utah.

74. Aussenhofer, S. and A. Webb, *An eight-channel transmit/receive array of TE 01 mode high permittivity ceramic resonators for human imaging at 7T.* Journal of Magnetic Resonance, 2014. **243**: p. 122-129.

75. Avdievich, N.I., et al., *Decoupling of a tight-fit transceiver phased array for human brain imaging at 9.4T: Loop overlapping rediscovered.* Magn Reson Med, 2017.

76. Taracila, V., et al., *Image uniformity improvement for birdcage-like volume coils at 400 MHz using multichannel excitations.* Concepts in Magnetic Resonance Part B: Magnetic Resonance Engineering, 2006. **29**(3): p. 153-160.

77. Orzada, S., et al., *RF Excitation Using Time Interleaved Acquisition of Modes (TIAMO) to Address B(1) Inhomogeneity in High-Field MRI.* Magnetic Resonance in Medicine, 2010. **64**(2): p. 327-333.

78. King, S.B., S.M. Varosi, and G.R. Duensing, *Eigenmode analysis for understanding phased array coils and their limits.* Concepts in Magnetic Resonance Part B-Magnetic Resonance Engineering, 2006. **29B**(1): p. 42-49.

79. King, S.B., S.M. Varosi, and G.R. Duensing, *Optimum SNR Data Compression in Hardware Using an Eigencoil Array.* Magnetic Resonance in Medicine, 2010. **63**(5): p. 1346-1356.

80. Wang, C., P. Qu, and G.X. Shen, *Potential advantage of higher-order modes of birdcage coil for parallel imaging.* J Magn Reson, 2006. **182**(1): p. 160-7.

81. Zhao, Y., et al. *On the E-field construction/deconstruction and B1+ Efficiency/Homogeneity with Transmit Array Eigen Modes*. in *ISMRM*. 2014. Milan, Italy.

82. Santini, T., et al. *A new RF coil for foot and ankle imaging at 7T MRI*. in *In Proc. of the 25th International Society of Magnetic Resonance in Medicine Annual Meeting*. 2017. Honolulu, Hawaii, USA.

83. Zhao, Y., et al., *Dual optimization method of radiofrequency and quasistatic field simulations for reduction of eddy currents generated on 7T radiofrequency coil shielding.* Magn Reson Med, 2014.

84. Ibrahim, T.S., Y.K. Hue, and L. Tang, *Understanding and manipulating the RF fields at high field MRI.* Nmr in Biomedicine, 2009. **22**(9): p. 927-36.

85. Hue, Y.-K., et al., *A Complete Modeling System with Experimental Validation for Calculating the Transmit and Receive Fields, Total Power Deposition, Input Impedance, and Coupling between Coil Elements* in *ISMRM*. 2008. p. 1193.

86. Zhao, Y., et al., *Studies in RF power communication, SAR, and temperature elevation in wireless implantable neural interfaces.* PLoS One, 2013. **8**(11): p. e77759.

87. Raval S, S.T., Wood S, Krishnamurthy N, Ibrahim TS. *In-vivo (8x4) 32-ch Tx-only Body Array for UHF MR*. in *In Proc. of the 25th International Society of Magnetic Resonance in Medicine Annual Meeting*. 2017. Honolulu, Hawaii, USA.

88. Christ, A., et al., *The Virtual Family--development of surface-based anatomical models of two adults and two children for dosimetric simulations.* Phys Med Biol, 2010. **55**(2): p. N23-38.

89. Vester, M., et al. *Using a mode concept to reduce hardware needs for multichannel transmit array*. in *ISMRM*. 2006.

90. Kozlov, M. and R. Turner, *Analysis of RF transmit performance for a 7T dual row multichannel MRI loop array.* Conf Proc IEEE Eng Med Biol Soc, 2011. **2011**: p. 547-53.

91. G. C. Wiggins, O.K., E. Zakszewski,V. Alagappan,C. J. Wiggins and L. L. Wald, *A 7 Tesla Gradient Mode Birdcage Coil for Improved Temporal and Occipital Lobe SNR*, in *ISMRM*. 2006: Seattle, Washington, USA.

92. Orzada, S., et al., *Time-interleaved acquisition of modes: an analysis of SAR and image contrast implications.* Magn Reson Med, 2012. **67**(4): p. 1033-41.

93. Yazdanbakhsh, P., et al., *Variable Power Combiner for a 7T Butler Matrix Coil Array.* ISMRM, 2009: p. 397.

94. Alagappan, V., et al. *A Simplified 16-channel Butler Matrix for Parallel Excitation with the Birdcage Modes at 7T*. in *Proc. Intl. Soc. Mag. Reson. Med. 16*. 2008.

95. Pauly, J., D. Nishimura, and A. Macovski, *A k-space analysis of small-tip-angle excitation.* Journal of magnetic resonance, 2011. **213**(2): p. 544-557.

96. Setsompop, K., et al., *Slice-selective RF pulses for in vivo B1+ inhomogeneity mitigation at 7 tesla using parallel RF excitation with a 16-element coil.* Magn Reson Med, 2008. **60**(6): p. 1422-32.

97. Katscher, U., et al., *Transmit SENSE.* Magn Reson Med, 2003. **49**(1): p. 144-50.

98. Gilbert, K.M., et al., *A radiofrequency coil to facilitate B-1(+) shimming and parallel imaging acceleration in three dimensions at 7 T.* Nmr in Biomedicine, 2011. **24**(7): p. 815-823.

99. Shajan, G., et al., *A 16-channel dual-row transmit array in combination with a 31-element receive array for human brain imaging at 9.4 T.* Magn Reson Med, 2013.

100. Avdievich, N.I., *Transceiver-Phased Arrays for Human Brain Studies at 7 T.* Applied Magnetic Resonance, 2011. **41**(2-4): p. 483-506.

101. Trakic, A., et al., *A Rapidly Rotating RF Coil for MRI.* Concepts in Magnetic Resonance Part B-Magnetic Resonance Engineering, 2009. **35B**(2): p. 59-66.

102. Trakic, A., et al., *Electromechanical Design and Construction of a Rotating Radio-Frequency Coil System for Applications in Magnetic Resonance.* Ieee Transactions on Biomedical Engineering, 2012. **59**(4): p. 1068-1075.

103. Alsop, D.C., T.J. Connick, and G. Mizsei, *Spiral volume coil for improved RF field homogeneity at high static magnetic field strength.* Magnetic Resonance in Medicine, 1998. **40**(1): p. 49-54.

104. M. Kozlov and H.E. Möller. *Safety excitation efficiency of MRI 300MHz dualrow transmit arrays*. in *Antennas and Propagation & USNC/URSI National Radio Science Meeting*. 2015. Vancouver: IEEE.

105. Collins, C.M., S. Li, and M.B. Smith, *SAR and B1 field distributions in a heterogeneous human head model within a birdcage coil.* Magnetic Resonance in Medicine, 1998. **40**(6): p. 847-856.

106. Hoult, D.I., *Sensitivity and Power Deposition in a High-Field Imaging Experiment.* Journal of Magnetic Resonance Imaging, 2000. **12**(1): p. 46-67.

107. Ibrahim, T.S., et al., *Effect of RF coil excitation on field inhomogeneity at ultra high fields: A field optimized TEM resonator.* Magnetic Resonance Imaging, 2001. **19**(10): p. 1339-1347.

108. Tang, L., Y.K. Hue, and T.S. Ibrahim, *Studies of RF Shimming Techniques with Minimization of RF Power Deposition and Their Associated Temperature Changes.* Concepts in Magnetic Resonance Part B-Magnetic Resonance Engineering, 2011. **39B**(1): p. 11-25.

109. van den Bergen, B., et al., *7 T body MRI: B-1 shimming with simultaneous SAR reduction.* Physics in Medicine and Biology, 2007. **52**(17): p. 5429-5441.

110. Van den Berg, C.A.T., et al., *Simultaneous B-1(+) homogenization and specific absorption rate hotspot suppression using a magnetic resonance phased array transmit coil.* Magnetic Resonance in Medicine, 2007. **57**(3): p. 577-586.

111. Ugurbil, K., *The road to functional imaging and ultrahigh fields.* Neuroimage, 2012. **62**(2): p. 726-35.

112. Vaidya, M.V., et al., *Improved detection of fMRI activation in the cerebellum at 7T with dielectric pads extending the imaging region of a commercial head coil.* J Magn Reson Imaging, 2018. **48**(2): p. 431-440.

113. Sohn, S.-M., et al., *RF head coil design with improved RF magnetic near-fields uniformity for magnetic resonance imaging (MRI) systems.* IEEE transactions on microwave theory and techniques, 2014. **62**(8): p. 1784-1789.

114. Fiedler, T.M., M.E. Ladd, and A.K. Bitz, *SAR Simulations & Safety.* Neuroimage, 2018. **168**: p. 33-58.

115. Staewen, R.S., et al., *3-D FLASH imaging using a single surface coil and a new adiabatic pulse, BIR-4.* Investigative radiology, 1990. **25**(5): p. 559-567.

116. Tannús, A. and M. Garwood, *Adiabatic pulses.* NMR in Biomedicine, 1997. **10**(8): p. 423-434.

117. Zhu, Y., *Parallel excitation with an array of transmit coils.* Magn Reson Med, 2004. **51**(4): p. 775-84.

118. Zhang, Z., et al., *Reduction of transmitter B1 inhomogeneity with transmit SENSE slice-select pulses.* Magn Reson Med, 2007. **57**(5): p. 842-7.

119. Wu, X., et al., *Simultaneous multislice multiband parallel radiofrequency excitation with independent slice-specific transmit B1 homogenization.* Magn Reson Med, 2013. **70**(3): p. 630-8.

120. Orzada, S., et al., *RF excitation using time interleaved acquisition of modes (TIAMO) to address B1 inhomogeneity in high-field MRI.* Magn Reson Med, 2010. **64**(2): p. 327-33.

121. Santini, T., et al., *In-vivo and numerical analysis of the eigenmodes produced by a multi-level Tic-Tac-Toe head transmit array for 7 Tesla MRI.* PLoS One, 2018. **13**(11): p. e0206127.

122. Wood S., K.N., Santini, T., Raval, S., and Ibrahim TS. *Evaluation of an Anthropomorphic Phantom with In-Vivo Using Quantitative MRI.* in *In Proc. of the 25th International Society of Magnetic Resonance in Medicine Annual Meeting*. 2017. Honolulu, Hawaii, USA.

123. Raval, S.B., et al., *Ultra-high field upper extremity peripheral nerve and non-contrast enhanced vascular imaging.* PLoS One, 2017. **12**(6): p. e0175629.

124. Raval, S.B., et al., *Ultra-high-field RF coil development for evaluating upper extremity imaging applications.* NMR Biomed, 2016.

125. Ibrahim, T.S. and R. Lee, *Evaluation of MRI RF probes utilizing infrared sensors.* IEEE Trans Biomed Eng, 2006. **53**(5): p. 963-7.

126. Ferrand, G., et al., *Generalized double-acquisition imaging for radiofrequency inhomogeneity mitigation in high-field MRI: experimental proof and performance analysis.* Magn Reson Med, 2012. **67**(1): p. 175-82.

127. Nehrke, K., A.M. Sprinkart, and P. Bornert, *An in vivo comparison of the DREAM sequence with current RF shim technology.* MAGMA, 2015. **28**(2): p. 185-94.

128. Hoyos-Idrobo, A., et al., *On variant strategies to solve the magnitude least squares optimization problem in parallel transmission pulse design and under strict SAR and power constraints.* IEEE Trans Med Imaging, 2014. **33**(3): p. 739-48.

129. Tang, L., Y.K. Hue, and T.S. Ibrahim, *Studies of RF shimming techniques with minimization of RF power deposition and their associated temperature changes.* Concepts in Magnetic Resonance Part B: Magnetic Resonance Engineering, 2011. **39**(1): p. 11-25.

130. Mao, W., et al., *Calculation of SAR for Transmit Coil Arrays.* Concepts Magn Reson Part B Magn Reson Eng, 2007. **31B**(2): p. 127-131.

131. Clement, J.D., R. Gruetter, and O. Ipek, *A human cerebral and cerebellar 8-channel transceive RF dipole coil array at 7T.* Magn Reson Med, 2018.

132. Zwanenburg, J.J., et al., *Fluid attenuated inversion recovery (FLAIR) MRI at 7.0 Tesla: comparison with 1.5 and 3.0 Tesla.* European radiology, 2010. **20**(4): p. 915-922.

133. Massire, A., et al., *Parallel-transmission-enabled three-dimensional T2 -weighted imaging of the human brain at 7 Tesla.* Magn Reson Med, 2015. **73**(6): p. 2195-203.

134. Gizewski, E.R., et al., *High-resolution anatomy of the human brain stem using 7-T MRI: improved detection of inner structures and nerves?* 2014. **56**(3): p. 177-186.

135. Eggenschwiler, F., et al., *3D T2-weighted imaging at 7T using dynamic kT-points on single-transmit MRI systems.* 2016. **29**(3): p. 347-358.

136. Kim, J., et al., *Development of a 7 T RF coil system for breast imaging.* NMR in Biomedicine, 2016.

137. Zhao, Y., et al., *Dual optimization method of radiofrequency and quasistatic field simulations for reduction of eddy currents generated on 7T radiofrequency coil shielding.* Magn Reson Med, 2015. **74**(5): p. 1461-9.

138. Krishnamurthy, N., T. Zhao, and T.S. Ibrahim, *Effects of receive-only inserts on specific absorption rate, B1 (+) field, and Tx coil performance.* Journal of magnetic resonance imaging, 2014. **39**(2): p. 475-84.

139. Ibrahim, T.S. and L. Tang, *Insight into RF power requirements and B1 field homogeneity for human MRI via rigorous FDTD approach.* Journal of Magnetic Resonance Imaging, 2007. **25**(6): p. 1235-1247.

140. Ibrahim, T.S., et al., *In-depth study of the electromagnetics of ultrahigh-field MRI.* NMR in Biomedicine, 2007. **20**(1): p. 58-68.

141. Wood, S., et al., *Design and fabrication of a realistic anthropomorphic heterogeneous head phantom for MR purposes.* PLoS One, 2017. **12**(8): p. e0183168.

142. Theysohn, J., et al., *Subjective acceptance of 7 Tesla MRI for human imaging.* Magnetic Resonance Materials in Physics, Biology and Medicine, 2008. **21**(1-2): p. 63-72.

143. Adriany, G., et al., *Transmit and receive transmission line arrays for 7 Tesla parallel imaging.* Magnetic Resonance in Medicine, 2005. **53**(2): p. 434-445.

144. Keil, B., et al., *Design Optimization of a 32-Channel Head Coil at 7T* ISMRM, 2010: p. 6960.

145. Robitaille, P.-M.L., et al., *Human magnetic resonance imaging at 8 T.* NMR Biomed, 1998. **11**(6): p. 263-265.

146. Lattanzi, R., et al., *Electrodynamic Constraints on Homogeneity and Radiofrequency Power Deposition in Multiple Coil Excitations.* Magnetic Resonance in Medicine, 2009. **61**(2): p. 315-334.

147. Ercan, A.E., et al., *Diffusion-weighted chemical shift imaging of human brain metabolites at 7T.* Magn Reson Med, 2014: p. doi:10.1002/mrm.25346

148. Li, M., et al., *In vivo Sensitivity Estimation and Imaging Acceleration with a Rotating RF Coil Arrays at 7 Tesla.* Journal of Magnetic Resonance, 2014p. doi:10.1016/j.jmr.2014.12.004.

149. Uludag, K., B. Muller-Bierl, and K. Ugurbil, *An integrative model for neuronal activity-induced signal changes for gradient and spin echo functional imaging.* Neuroimage, 2009. **48**(1): p. 150-65.

150. Yacoub, E., et al., *Spin-echo fMRI in humans using high spatial resolutions and high magnetic fields.* Magnetic Resonance in Medicine, 2003. **49**(4): p. 655-664.

151. Yacoub, E., et al., *Imaging brain function in humans at 7 Tesla.* Magnetic Resonance in Medicine, 2001. **45**(4): p. 588-594.

152. Ogawa, S., et al., *Functional brain mapping by blood oxygenation level-dependent contrast magnetic resonance imaging. A comparison of signal characteristics with a biophysical model.* Biophys J, 1993. **64**(3): p. 803-12.

153. Umutlu, L., et al., *7 Tesla MR imaging: opportunities and challenges.* Rofo, 2014. **186**(2): p. 121-9.

154. Wolf, S., et al., *SAR simulations for high-field MRI: how much detail, effort, and accuracy is needed?* Magn Reson Med, 2013. **69**(4): p. 1157-68.

155. van Lier, A.L.H.M.W., et al., *Radiofrequency heating induced by 7T head MRI: Thermal assessment using discrete vasculature or pennes' bioheat equation.* Journal of Magnetic Resonance Imaging, 2012. **35**(4): p. 795-803.

156. Bitz, A., et al. *Comparison of simulation-based and measurement-based RF shimming for whole-body MRI at 7 Tesla*. in *Proceedings of the 18th Annual Meeting of ISMRM, Stockholm, Sweden*. 2010.

157. Homann, H., et al., *Local SAR management by RF shimming: a simulation study with multiple human body models.* Magnetic Resonance Materials in Physics, Biology and Medicine, 2012. **25**(3): p. 193-204.

158. Rietsch, S.H.G., et al., *Parallel transmit capability of various RF transmit elements and arrays at 7T MRI.* Magn Reson Med, 2018. **79**(2): p. 1116-1126.

159. Avdievich, N.I., et al., *Evaluation of transmit efficiency and SAR for a tight fit transceiver human head phased array at 9.4 T.* NMR Biomed, 2017. **30**(2).

160. Lattanzi, R. and D.K. Sodickson, *Ideal current patterns yielding optimal signal-to-noise ratio and specific absorption rate in magnetic resonance imaging: computational methods and physical insights.* Magn Reson Med, 2012. **68**(1): p. 286-304.

161. Sohn, S.M., et al., *RF Head Coil Design with Improved RF Magnetic Near-Fields Uniformity for Magnetic Resonance Imaging (MRI) Systems.* IEEE Trans Microw Theory Tech, 2014. **62**(8): p. 1784-1789.

162. Cho, Z.H. and Y.M. Ro, *Reduction of susceptibility artifact in gradient-echo imaging.* Magnetic Resonance in Medicine, 1992. **23**(1): p. 193-200.

163. Stenger, V.A., F.E. Boada, and D.C. Noll, *Three-dimensional tailored RF pulses for the reduction of susceptibility artifacts in T(*)(2)-weighted functional MRI.* Magn Reson Med, 2000. **44**(4): p. 525-31.

164. Tamer S Ibrahim, T.S., Shailesh Raval, Narayanan Krishnamurthy, Sossena Wood, Jung-Hwan Kim, Yujuan Zhao, Xiaoping S Wu, Essa S Yacoub, Howard S Aizenstein, and Tiejun Zhao, *Towards Homogeneous 7T Neuro Imaging: Findings and Comparisons between 7T TTT and NOVA RF Coil Systems.* ISMRM, 2017.

165. Vaughan, J.T., Garwood, M., Collins, C.M., Liu, W., DelaBarre, L., Adriany, G., Andersen, P., Merkle, H., Goebel, R., Smith, M.B. and Ugurbil, K., *7T vs. 4T: RF power, homogeneity, and signal-to-noise comparison in head images.* Magn Reson Med, 2001. **46**: p. 24–30.

166. T.S. Ibrahim, R.L., B. A. Baertlein, A.M. Abduljalil, H. Zhu, P.L. Robitaille, *Effect of RF coil excitation on field inhomogeneity at ultra high fields: a field optimized TEM resonator.* MRI, 2001. **19**: p. 1339–1347.

167. Yujuan Zhao , T.Z., Shailesh B. Raval , Narayanan Krishnamurthy , Hai Zheng ,Chad T. Harris , William B. Handler , Blaine A. Chronik , and Tamer S. Ibrahim *Dual Optimization Method of RF and Quasi-Static Field Simulations for Reduction of Eddy Currents Generated on 7T RF Coil Shielding.* MRM, 2014: p. DOI: 10.1002/mrm.25424.

168. Santini, T., et al., *A new RF transmit coil for foot and ankle imaging at 7T MRI.* MRI, 2018. **45**(1873-5894 (Electronic)): p. 10.1016/j.mri.2017.09.005.

169. Ibrahim, T.S., et al., *Analysis of B 1 field profiles and SAR values for multi-strut transverse electromagnetic RF coils in high field MRI applications.* Physics in Medicine & Biology, 2001. **46**(10): p. 2545.

170. Christ, A., et al., *The Virtual Family-development of surface-based anatomical models of two adults and two children for dosimetric simulations.* Physics in Medicine and Biology, 2010. **55**(2): p. N23-N38.

171. Luengo, C.L., *DIP Lib,Image : Measuring boundary length* http://www.diplib.org/ http://www.cb.uu.se/~cris/blog/index.php/archives/310. 2003.

172. Proffitt, D. and D. Rosen, *Metrication errors and coding efficiency of chain-encoding schemes for the representation of lines and edges.* Computer Graphics and Image Processing, 1979. **10**(4): p. 318-332.

173. Vossepoel, A.M. and A.W.M. Smeulders, *Vector code probability and metrication error in the representation of straight lines of finite length.* Computer Graphics and Image Processing, 1982. **20**(4): p. 347-364.

174. Tilley, A.R., *The measure of man and woman, human factors in design.* John Wiley & Sons, 2002: p. p27.

175. Ibrahim, T.S., D. Stough, and T. Zhao, *20-Ch Tx Modular Array for 7T PTX Applications.* ISMRM, 2012. **2807**.

176. Hue, Y.-K., et al., *A Complete Modeling System with Experimental Validation for Calculating the Transmit and Receive Fields, Total Power Deposition, Input Impedance, and Coupling between Coil Elements.* ISMRM, 2008: p. 0438.

177. FSL, *Brain Extraction Tool of FMRIB Software Library,* http://fsl.fmrib.ox.ac.uk/fsl/fslwiki/BET.

178. Insight Toolkit, I., *ITK-SNAP* http://www.itksnap.org/pmwiki/pmwiki.php.

179. Ibrahim, T.S., et al., *7T RF Coil System with Non-Subject Specific RF Fields & Extended Coverage into the Cerebellum & Temporal Lobe.* ISMRM Workshop on Ultra High Field

MRI: Technological Advances & Clinical Applications, Heidelberg, Germany, March 2016.

180. Ibrahim, T.S., et al., *Homogenous 7T Neuro Imaging.* The 10th Bi-Annual 2015 Workshop: High Field MR Imaging and Spectroscopy, Minneapolis, MN, October 2015.

181. Smagula, S.F., et al., *Gray matter regions statistically mediating the cross-sectional association of eotaxin and set-shifting among older adults with major depressive disorder.* (1099-1166 (Electronic)).

182. Smagula, S.F., et al., *Association of Hippocampal Substructure Resting-State Functional Connectivity with Memory Performance in Older Adults. LID - S1064-7481(18)30260-4 [pii] LID - 10.1016/j.jagp.2018.03.003 [doi]*. (1545-7214 (Electronic)).

183. de Greef, M., et al., *Specific absorption rate intersubject variability in 7T parallel transmit MRI of the head.* Magnetic Resonance in Medicine, 2012. **69**(5): p. 1476-1485.

184. Kraff, O., et al., *MRI at 7 tesla and above: Demonstrated and potential capabilities.* J Magn Reson Imaging, 2014: p. DOI: 10.1002/jmri.24573.

185. Santini, T., et al. *Noise mitigation from high-resolution 7T MRI images*. in *In Proc. of the 26th International Society of Magnetic Resonance in Medicine Annual Meeting*. 2018. Paris, France.

186. Berron, D., et al., *A protocol for manual segmentation of medial temporal lobe subregions in 7 Tesla MRI.* NeuroImage: Clinical, 2017. **15**: p. 466-482.

187. Tournier, J.D., F. Calamante, and A. Connelly, *MRtrix: Diffusion tractography in crossing fiber regions.* International Journal of Imaging Systems and Technology, 2012. **22**(1): p. 53-66.